11-30-2023

UV Dynamics of Different Ring Molecules Studied by Ultrafast Electron Diffraction

Sajib Kumar Saha
University of Nebraska-Lincoln, ssaha2@huskers.unl.edu

Recommended Citation

Saha, Sajib Kumar, "UV Dynamics of Different Ring Molecules Studied by Ultrafast Electron Diffraction" (2023). *Dissertations and Doctoral Documents from University of Nebraska-Lincoln, 2024–*. 20.
https://digitalcommons.unl.edu/dissunl/20

UV DYNAMICS OF DIFFERENT RING MOLECULES STUDIED BY ULTRAFAST ELECTRON DIFFRACTION

by

Sajib Kumar Saha

A DISSERTATION

Presented to the Faculty of

The Graduate College at the University of Nebraska

In Partial Fulfillment of Requirements

For the Degree of Doctor of Philosophy

Major: Physics and Astronomy

Under the Supervision of Professor Martin Centurion

Lincoln, Nebraska

December, 2023

UV DYNAMICS OF DIFFERENT RING MOLECULES STUDIED BY ULTRAFAST ELECTRON DIFFRACTION

Sajib Kumar Saha, Ph.D.

University of Nebraska, 2023

Advisor: Martin Centurion

Understanding natural light-induced phenomena requires a direct viewing of atomic motion during structural evolution, which, in turn, facilitates controlling and manipulating these light-induced processes. Ultrafast Electron Diffraction (UED) is a structure-sensitive technique that can probe electronic and nuclear dynamics at sub-angstrom spatial and femtosecond time scales. UED has become a vital tool for studying photo-induced molecular dynamics and underlying science.

Organic ring systems are prevalent in biology, materials, and pharmaceuticals. Their synthesis and transformation are fundamental in synthetic chemistry, influencing various fields. We used UV photons to photo-excite different cyclic molecules and investigated their photodynamics using gas phase UED.

The photochemical transformation of quadricyclane involves an ultrafast process in which a highly strained three-membered ring is converted into less strained five and six-membered rings. The isomerization of quadricyclane into norbornadiene has recently garnered considerable attention, particularly within its application as a Molecular Solar Energy Storage (MOST) system. The UV-induced reaction probed by MeV-UED displays simultaneous electronic and nuclear dynamics. Comparison of experimental data with

simulations reveals a substantial structural change as the molecule crosses the conical intersection. The analysis also suggests the involvement of a dissociation channel in addition to QD to NB isomerization in photodynamics.

Cis stilbene has been serving as a model system for exploring photoisomerization and photocyclization. While the dynamics of the first excited state have been extensively investigated, higher excited states remain less explored. We employed MeV-UED to examine the dynamics following ionization due to the absorption of two UV photons. The experimental data precisely captures the oscillations of the cis-stilbene cation and agrees well with theoretical predictions.

Pentamethyl-cyclopentadiene (PMCP) is a small polyene molecule, and investigating its photoreaction can provide valuable insights into reaction mechanisms, which can be applied to studying other complex polyenes. Using our KeV-UED setup, we initiated the photoreaction by pumping with 267nm photon and probed by 90KeV electron beam. The preliminary analysis of this data shows a good pump-probe signal and structural change in the molecule.

Dedication

To my beloved wife **Shampa Saha** and our adorable daughter **Priyonwita Saha.**

I want the whole world to know that you guys never let me down in achieving this milestone.

Acknowledgement

As I write this acknowledgment, it signifies the end of my Ph.D. journey after about seven and a half years. Balancing my mental well-being with academic challenges was a constant struggle, but now, it's finally done. The journey has brought immense honor and satisfaction, making every challenging experience worthwhile. I want to thank everyone who played a crucial role in fulfilling my dream of accomplishing the Ph.D. degree; I am forever indebted to them.

I would like to express my gratitude to my advisor, Professor Martin Centurion. He is the most excellent person I have ever met and the best advisor a student can think of. I extend my sincere appreciation to him for his invaluable guidance, unwavering support, and expert mentorship throughout the entire research process. His insightful feedback and encouragement have played a crucial role in shaping the trajectory of my Ph.D. journey. I consider myself truly fortunate to have him as a mentor, and I deeply appreciate the time and effort he dedicated to helping me achieve my research goals. Beyond the realm of research, Professor Centurion has been the only person in my workplace able to understand my family's needs and has offered valuable suggestions to navigate family issues. I will always remember his contribution to my accomplishments, simultaneously fostering a harmonious work-life balance.

I would also like to thank my honorable committee members, Professor Bradley Shadwick, Professor Kees Uiterwaal, and Professor Yinsheng Guo. I am thankful for the time and effort they dedicated to helping me achieve my academic goals. Their insightful comments on my thesis and comprehensive examination report, and valuable time presiding over my comprehensive exam and thesis defense made me forever grateful. Their guidance has been invaluable, and I am fortunate to have had such a dedicated and knowledgeable committee to oversee my research.

I will always remember the invaluable mentorship of Dr. Pedro Nunes, who actively taught me how to analyze data using MATLAB. I was very scared of using MATLAB because I had no prior experience. Dr. Nunes helped me learn how to use MATLAB to analyze data, how to search various codes online, and how to attain the decisive output from the analysis. He is a superb person. His endless patience and supportive mind facilitate learning not only data analysis but also the sample delivery system and cold trap designing using computer-assisted designing. Dr. Yanwei Xiong is another nice guy I met during my PhD research. I always confronted him with lots of problems pertinent to ultrafast electron diffraction experiments and fundamental physics. I always find him there for me to get all my questions correctly answered. He is a true partner in conducting complex gas-phase electron diffraction experiments. I also express my deep gratitude to Dr. Kyle Wilkin. He wrote a few analysis codes for me, which saved me a lot of time in performing complex analyses. Dr. Wilkin also helped me get acquainted with various equipment in the lab and answered a lot of my queries regarding lab issues.

I sincerely thank my colleagues, Sri Bhavya Muvva, Jackson Lederer, Haoran Zhao, and Cuong Le. I can never forget their contribution to setting up experiments and taking data on the cold and calm winter nights. These guys are amazing and selflessly supported me in accomplishing my research goals. I want to thank Yibo Wang, Mahmudul Hasan, Dr. Xiaojun Wang, Dr. Lauren Heald, and Nikhil Pachisia for their technical suggestions in selecting the right decision about various laboratory issues.

A significant amount of time was spent finishing the coursework required to complete the Ph.D. I will never forget the names of those who helped me solve numerous complex problems in different courses. Gautam Gurung, you are a genius, and your teaching capability is inimitable. I am also grateful to Mahmudul Hasan, Syed Qamar Abbas, Bret Gergely, Esha Mishra to learn physics and solve various physics problems by discussing and consulting with them.

Apart from research and academics, the Ph.D. journey required mental peace to overcome all the stress due to the unexpected consequences pertinent to academics. The person who was leading in balancing the stressful academics and peaceful family life was none other than my beautiful wife Shampa Saha. I know nobody else can recognize your sacrifice, nobody else can realize the pain you bear; I want to say that I can never pay your contributions, nor can I acknowledge them in words. Always keep in mind that I am always here for you, our paths merge until eternity. I love you, and I will always love you until my last breath. Thanks for being with me.

I got my most precious gift, my daughter Priyonwita, during my Ph.D. life. I can still sense her touch with her tiny fingers, which alleviated all my stresses, struggles, and pains. I love you, little angel. You are just a kid, but your footprint in my life was bigger than anyone else's.

Being away from my beloved family and continuing to study here was the most challenging part of the Ph.D. journey. I never imagined staying 8000 miles away from my Mom, Dad, Sister, and Brother. However, I was able to do it because of their continuous courage, support, and blessings from thousands of miles away. Today, whoever I am is the collective contribution of all of them. My sincere respect and love will find their path towards them.

I would also like to acknowledge the selfless contribution of my Mom-in-law, Dad-in-law, Sister-in-law, and Brother-in-law. The blessings and support I got from them are immeasurable.

Finally, I want to express my deep appreciation to all the Bangladeshi students and Bangladeshi committee members in Lincoln and Omaha. Their company, cooperation, and support made a smooth transition to settle from our own country Bangladesh to the USA. I will always thankfully acknowledge their contribution.

Table of Contents

List of Figures

List of Tables

Chapter 1

Introduction to Gas Phase Ultrafast Electron Diffraction

1.1 Introduction

When light passes through two slits and strikes a screen, an interference pattern is observed. This pattern consists of a series of light and dark bands, known as interference fringes, providing valuable information about slit width, spacing, and the incoming light's wavelength. Electrons can exhibit both wave and particle nature. Like light wave, when an electron wave interacts with matter, the interaction can be recorded on a detector. This interaction creates a diffraction pattern on the detector. The diffraction pattern provides us information about the structure of the scatterer. This is the basis of electron diffraction. With the advent of femtosecond lasers and many technological improvements, the temporal resolution of the gas phase ultrafast electron diffraction is routinely found to be as good as 150fs, which is adequate in some cases to image the transient states and evolution of molecular structures during the photochemical reaction route from reactant to product state. Using a DC electron gun and RF photoinjector, electrons are accelerated from tens of KeV to MeV, which makes the de-Broglie wavelength of the electron below picometer regimes and hence improves the spatial resolution to sub-Angstrom range. In this chapter, I will discuss my motivation to conduct UED experiments by UV light-excited organic cyclic molecules with a different number of carbon atoms in their ring and study their dynamics. I will also briefly present the history of UED so that readers can realize how eventually UED arrived at its present state. I will also describe the necessity of gas-phase ultrafast electron diffraction. I reviewed some necessary theories from several references and will present them here to analyze and interpret UED data. The Independent Atom Model (IAM), a widely used method for calculating scattering intensity, has certain limitations when applied to the analysis of electronic dynamics in UED. I will discuss two electronic effects resulting from chemical reactions that the IAM fails to account for. I will also explain the contribution of conical intersection to the photodynamics of organic molecules. I will end this chapter by showing the difference between UED and X-ray diffraction.

1.2 Motivation for this research

Photochemistry is an important event in nature that illustrates how light energy is harvested and stored in molecules. Photochemistry serves as the key to understanding how to control and manipulate light-induced processes in nature. Understanding the light induced-processes found their key role in identifying and predicting UV damage of DNA[1], discovering an effective way of synthesizing vitamin D[2], predicting the ozone layer depletion due to the emission of halogenated refrigerants, propellants, and solvents, and their photoreaction with UV[3][4]. The detailed knowledge of this photoinduced process necessitates how a molecule evolves in terms of its electronic arrangements and nuclear geometry after it absorbs photons. It is necessary to study both the spatial and temporal evolution of molecular geometry for modeling the exact photochemical path from the reactant to the product state. Laser-based spectroscopic methods are capable of measuring the electron dynamics from femtosecond to attosecond time scale, but these methods can study nuclear geometry only indirectly. Diffraction methods like UED are directly sensitive to the molecular structure. Since UED can probe molecular dynamics in a femtosecond time scale and it is structure sensitive, it is a vital tool for understanding structural evolution and underlying science. Using a UV pump, we excited different ring molecules and probed them using UED with a time resolution of hundreds of femtoseconds. Using structure sensitive UED, my goal is to reveal the UV-induced dynamics, investigate associated reaction channels, find structural evolution at various stage of reaction, determine the end products and their relative ratio at the end of photoreaction.

1.3 History of gas phase electron diffraction

The origin of UED lies in the wave nature of electrons. In 1801, Thomas Young confirmed the wave nature of light by doing the double slit experiment and showing the interference of light[5]. In different times of the nineteenth century, the photoelectric effect was observed by different groups of scientists. In 1905, Albert Einstein proposed a theory to explain the photoelectric effect that predicted that light can exhibit wave nature that consists of wavelength and frequency, and particle nature which has discrete energy. In 1922, the Compton effect was observed, and this can only be explained using photoelectric theory proposed by Albert Einstein. The Compton effect supports the dual nature of light. In 1924, de Broglie proposed that all microscopic matters exhibit wave properties and so does the electron[6]. He formulated the wavelength and particle's momentum as $\lambda = \frac{h}{p}$; which is the generalization of Einstein's equation for photon's energy $E = h\nu$, and photon's momentum $E = pc$. The hypothesis given by de Broglie was experimentally verified by two groups by observing the diffraction of electron. G. P. Thomson and A. Reid observed the predicted interference pattern by shooting a ray of electron on celluloid thin film and then on metal films[7][8]. C. J. Davisson and L. H. Germer observed the similar electron diffraction by directing a beam of electron on a nickel crystal surface[9][10]. They concluded that the phenomenon is analogous to the X-ray diffraction and the electron beam with velocity v, is equivalent to the wave of wavelength λ and they are related by $\lambda = \frac{h}{mv}$, which is essentially the de Brogli's equation. Following the experimental proof of the wave-particle duality of electrons, the first gas phase electron diffraction experiment was done in 1930 on CCl_4 by Mark. et. al[11]. They were able to successfully retrieve the molecular structure from this experiment. They used the position of maxima and minima in the interference pattern to measure the interatomic distance. The use of Fourier transformation of the diffraction signal to get the pair distribution function was first used by Pauling et al. in 1935 [12]. The necessity of tracking the molecular evolution after chemical reactions initiated the time resolved gas-phase electron diffraction reaction. In 1982, first time-resolved electron diffraction experiment was done[13]. In this experiment, a synchronized picosecond photoelectron pulse was used to probe the lattice structure of thin film aluminum. Professor Ahmed Zewail, who was awarded the Noble Prize for his pioneering work on femtochemistry, and his group carried out a series of experiments in an attempt to bring the temporal resolution of electron diffraction to picosecond and femtosecond limit to view the chemical reaction in real time[14][15][16][17][18][19][20]. Although the experimental time resolution was limited to the picosecond regime in these experiments, they laid a significant base for instrumentation and improving the temporal resolution of the electron diffraction and started the era of ultrafast electron diffraction (UED). Viewing the molecular structure from reactant to product in real-time and manipulating the chemical process is the foremost goal of UED. The typical time required for a nuclear motion takes about 100fs[21]. This ultrafast event necessitates the instrumental resolution of the UED setup to be 100fs or better. The origin of poor temporal resolution is due to the space charge effect in the electron pulse, velocity mismatch between electron and laser pulse and poor synchronization between the arrival of electron and compressing field. For the KeV-UED, the possible solution to circumvent the electron pulse broadening due to space charge effect is to use either compact electron gun or compressing electron pulse[21]. However, building a compact electron gun for gas phase targets has some engineering difficulties. To produce femtosecond electron pulse, Radio Frequency (RF) pulse compression technique using an RF cavity was conceptualized and developed by Dr. Luiten and Dr. Siwick's group[22][23][24]. They were able to produce electron pulse of duration 70fs and cross-sectional density of electron $2.5 \times 10^8\ cm^{-2}$[21]. The technique was potential enough to achieve a temporal resolution as good as 100fs[21]. In the MeV-UED facility at the SLAC National Accelerator Laboratory, RF photoinjector is used to accelerate the electron beam to a relativistic speed of 0.99C by an accelerating potential of 3.7MeV. The relativistic electron and the collinear geometry of the pump and probe essentially suppress the issue of velocity mismatch. Additionally, the high accelerating field facilitates producing electron pulse with high brightness, suppressing the pulse broadening due to space-charge effect[25][26]. The temporal resolution at this UED facility experimentally measured for gas-phase molecule to a milestone of 150fs[22][23][27][28]. In the tabletop UED setup in our lab, electrons are accelerated by a 90KV DC gun. We adapted the similar RF compression technology proposed by Luiten and Dr. Siwick's group[22] [23][24] to longitudinally compress the electron pulse. The velocity mismatch is removed using a tilted front laser[29][30]. The relative time or arrival of the electron pulse and compressing field in the RF cavity is precisely synchronized by a homemade synchronizing system[31] inspired from the system described in Ref[32]. These advancements collectively contribute to a temporal resolution of 240 fs in our UED system[31][33][34][35].

1.4 Why gas phase UED

There are several benefits in probing the molecule by UED in the gas phase. First of all, the molecular structure is not distorted due to the intermolecular force, so precise structure can be determined[36]. Secondly, coherent chemical dynamics can be found by using the gas phase as the molecule is not affected by solvent effects. Thirdly, in the gas phase precise excitation energy can be used, and finally the experimental data can be compared directly to the theory.

1.5 Quantum theory of scattering

In this section, we will derive the scattering amplitude of electrons due to interaction with an atom. I will also calculate the scattering amplitude for two specific potentials: Yukawa and Coulomb potential. Furthermore, I will derive the scattering amplitude for a charge distribution and an ensemble of molecules.

1.5.1 Scattering amplitude due to potential

In this section, I will derive an expression for the scattering amplitude when an electron is scattered by a potential. This scattering theory is based on the previously provided theory in Ref[37].

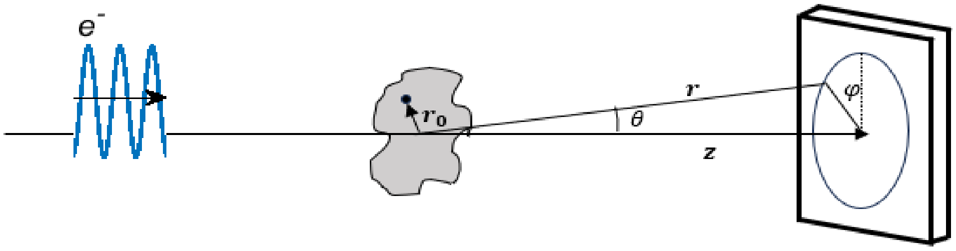

Figure 1.1: Schematic representation of electron scattering by a matter. The interaction of electrons and atoms within matter is recorded on a detector as a diffraction pattern, which gives information about the structure of molecules.

Let's consider, a bunch of electrons is propagating along z-direction in a field free environment. Eventually, the electrons are scattered by a group of atoms. The potential energy of the electron scattering by the atoms is represented by V, which can be taken as a function of distance only. The scattering event is probed by a detector at a distance r from the scattering center and we define the scattering angle to be θ. Let's start with the Schrödinger equation and we can write:

$$i\hbar\frac{\partial\psi}{\partial t}=\left[\frac{-\hbar^2}{2m_e}\nabla^2+eV(\boldsymbol{r})\right]\psi; \tag{1.1}$$

Since, the incident electron is free we can rewrite (1.1) for field free condition and it yields

$$i\hbar\frac{\partial\psi_0}{\partial t}=\frac{-\hbar^2}{2m_e}\nabla^2\psi_0,$$

$$\nabla^2\psi_0+\frac{2m_eE}{\hbar^2}\psi_0=0. \tag{1.2}$$

Where, E is the energy of the incident electron. The solution of equation (1.2) is given by

$$\psi_0(z)=Ae^{ikz}. \tag{1.3}$$

Where $k = \sqrt{2mE}/\hbar$. The solution of equation (1.1) contains both time and position dependence. However, we are only interested in the probability distribution of scattered waves for a steady state. Hence, we will drop the time dependent part[38] from the solution of equation (1.1). At a very large distance from the scattering center where $V(\boldsymbol{r}) \approx 0$, the resulting wave will include both the incident and scattered wave i.e.

$$\psi(r, \theta) = \psi_0 + \psi_{sc}. \tag{1.4}$$

At the large distance, the solution for ψ_{sc} has a form of spherical wave so that it preserves the probability. Also, the scattering wave will be angularly dependent. Hence, equation (1.4) can be written for large *r*.

$$\psi(r, \theta, \varphi) \approx Ae^{ikz} + Af(\theta, \varphi)\frac{e^{ikr}}{r}. \tag{1.5}$$

Here, we are assuming the scattering is elastic. This means the energy, hence the wavenumber before and after the scattering is same. Our goal is to determine the scattering amplitude $f(\theta, \varphi)$. We will employ the Born approximation to find the scattering amplitude.

Rewriting equation (1.1), we get,

$$\left[\frac{-\hbar^2}{2m_e}\nabla^2 + eV(\boldsymbol{r})\right] = E\psi.$$

In the form of Helmholtz equation, we can write

$$[\nabla^2 + k^2]\psi = U\psi. \tag{1.6}$$

Here, $U = \frac{2m_e eV(\boldsymbol{r})}{\hbar^2}$. We can solve equation (1.6) by using Green's function if we assume there is a source that behaves like a delta function. So, we can write from equation (1.6)

$$[\nabla^2 + k^2]G(\boldsymbol{r} - \boldsymbol{r_0}) = \delta(\boldsymbol{r} - \boldsymbol{r_0}) \tag{1.7}$$

The solution of equation (1.6), in terms of Green's function, is therefore[39],

$$\psi(\boldsymbol{r}) = \psi_0(\boldsymbol{r}) + \int G(\boldsymbol{r} - \boldsymbol{r_0})U(\boldsymbol{r_0})\psi(\boldsymbol{r_0})d^3\boldsymbol{r_0}. \tag{1.8}$$

Where, $\psi_0(\boldsymbol{r})$ satisfies the homogeneous Helmholtz equation $[\nabla^2 + k^2]\ \psi(\boldsymbol{r}) = 0$.

The solution of $G(\boldsymbol{r} - \boldsymbol{r_0})$ can be found by solving the equation (1.7) and it can be expressed as follows:

$$G(\boldsymbol{r} - \boldsymbol{r_0}) = -\frac{1}{4\pi}\frac{e^{ikr|r-\boldsymbol{r_0}|}}{|r-\boldsymbol{r_0}|}. \tag{1.9}$$

Putting this equation (1.9) in equation (1.8) we can have:

$$\psi(\boldsymbol{r}) = \psi_0(\boldsymbol{r}) - \frac{1}{4\pi}\int \frac{e^{ikr|r-\boldsymbol{r_0}|}}{|r-\boldsymbol{r_0}|}U(\boldsymbol{r_0})\psi(\boldsymbol{r_0})d^3\boldsymbol{r_0}. \tag{1.10}$$

For a typical scattering problem, $U(\boldsymbol{r_0})$ is localized and outside a certain area the influence of the potential vanishes. At a very large distance, the sample looks like a point particle. We can apply the far-zone approximation as

$$|\boldsymbol{r} - \boldsymbol{r_0}|^2 = r^2 + r_0^2 - 2\boldsymbol{r}.\boldsymbol{r_0} \cong r^2\left(1 - 2\frac{\boldsymbol{r}.\boldsymbol{r_0}}{r^2}\right). \tag{1.11}$$

Which can result as

$$|\boldsymbol{r} - \boldsymbol{r_0}| = r\left(1 - 2\frac{\boldsymbol{r}.\boldsymbol{r_0}}{r^2}\right)^{\boldsymbol{\frac{1}{2}}}. \tag{1.12}$$

Using binomial expansion, we get

$$|\boldsymbol{r}-\boldsymbol{r_0}| = r\left(1-2\frac{\boldsymbol{r}.\boldsymbol{r_0}}{r^2}\right)^{\frac{1}{2}} \cong r-\frac{\boldsymbol{r}}{r}.\boldsymbol{r_0} = r-\hat{\boldsymbol{r}}.\boldsymbol{r_0}. \tag{1.13}$$

Using (1.13), we can write the exponent in equation in (1.10) as

$$e^{ikr|\boldsymbol{r}-\boldsymbol{r_0}|} = e^{ik(r-\hat{r}.\boldsymbol{r_0})} = e^{ikr}e^{-ik\hat{r}.\boldsymbol{r_0}} = e^{ikr}e^{-i\boldsymbol{k}.\boldsymbol{r_0}}. \tag{1.14}$$

Where, $\boldsymbol{k} = k\hat{\boldsymbol{r}}$**,** is the wave-vector along the direction of $\hat{\boldsymbol{r}}$**.** For the denominator in equation (1.10), we will be using $|\boldsymbol{r}-\boldsymbol{r_0}| \cong r$; and hence the equation (1.10) yields:

$$\psi(\boldsymbol{r}) = \psi_0(\boldsymbol{r}) - \frac{1}{4\pi}\int \frac{e^{ikr}e^{-ik.r_0}}{r}U(\boldsymbol{r_0})\psi(\boldsymbol{r_0})d^3\boldsymbol{r_0}, \tag{1.15}$$

$$\psi(\boldsymbol{r}) = \psi_0(\boldsymbol{r}) - \frac{e^{ikr}}{4\pi r}\int e^{-i\boldsymbol{k}.\boldsymbol{r_0}}U(\boldsymbol{r_0})\psi(\boldsymbol{r_0})d^3\boldsymbol{r_0}. \tag{1.16}$$

Comparing equations (1.16) with (1.5) we can extract the scattering amplitude:

$$f(\theta,\varphi) = -\frac{1}{4\pi}\int e^{-i\boldsymbol{k}.\boldsymbol{r_0}}U(\boldsymbol{r_0})\psi(\boldsymbol{r_0})d^3\boldsymbol{r_0}. \tag{1.17}$$

Expressing the $U(\boldsymbol{r_0})$ in term of the potential we can have the equation:

$$f(\theta,\varphi) = -\frac{m_e e}{2\pi\hbar^2}\int e^{-i\boldsymbol{k}.\boldsymbol{r_0}}V(\boldsymbol{r_0})\psi(\boldsymbol{r_0})d^3\boldsymbol{r_0}. \tag{1.18}$$

At this point, we have $\psi(\boldsymbol{r_0})$ which is not a known quantity, hence we will be applying Born approximation which can replace the $\psi(\boldsymbol{r_0})$ with some known quantity. According to Born approximation, the incident wave is significantly more intense than the scattered wave within the scattering system such that the probability of multiple scattering is negligible[38]. In other words, the outgoing wave has an amplitude outside the scattering system that closely resembles the incident wave within the scattering system. Using this approximation, we can write:

$$\psi(\boldsymbol{r_0}) \approx \psi_0(\boldsymbol{r_0}) = Ae^{ikz_0}. \tag{1.19}$$

Plugging this into equation (1.18) we can write

$$f(\theta,\varphi) = -\frac{m_e e}{2\pi\hbar^2 A}\int e^{-i\boldsymbol{k}.\boldsymbol{r_0}}V(\boldsymbol{r_0})Ae^{ikz_0}d^3\boldsymbol{r_0},$$

$$f(\theta,\varphi) = -\frac{m_e e}{2\pi\hbar^2}\int e^{-i\boldsymbol{k}.\boldsymbol{r_0}-kz_0}V(\boldsymbol{r_0})d^3\boldsymbol{r_0}. \tag{1.20}$$

Omitting the subscript from equation (1.20) we can rewrite equation (1.20) as

$$f(\theta,\varphi) = -\frac{m_e e}{2\pi\hbar^2}\int e^{-i\boldsymbol{k}.\boldsymbol{r}-kz}V(\boldsymbol{r})d^3\boldsymbol{r}. \tag{1.21}$$

Now as per the ref[40],

$$\boldsymbol{k}.\boldsymbol{r} - kz = k\hat{\boldsymbol{r}}.\boldsymbol{r} - k\,\boldsymbol{r}.\hat{\boldsymbol{z}} = k(\hat{\boldsymbol{r}} - \hat{\boldsymbol{z}}).\boldsymbol{r} = \boldsymbol{s}.\boldsymbol{r}. \tag{1.22}$$

Where we wrote,

$$\boldsymbol{s} = k(\hat{\boldsymbol{r}} - \hat{\boldsymbol{z}}). \tag{1.23}$$

Here, $\boldsymbol{s}$ is called the momentum transfer vector and expressed by

$$s = \frac{4\pi}{\lambda}\sin\left(\frac{\theta}{2}\right). \tag{1.24}$$

Where λ is the wavelength of the incoming wave. Now returning to the equation (1.21) we can get,

$$f(\theta,\varphi) = -\frac{m_e e}{2\pi\hbar^2}\int e^{-i\boldsymbol{s}.\boldsymbol{r}}V(\boldsymbol{r})d^3\boldsymbol{r}. \tag{1.25}$$

Which tells that the scattering amplitude is the Fourier transform of the scattering potential. For a spherically symmetric potential $V(\boldsymbol{r}) = V(r)$ and using the relation in equation (1.24), and writing $f(\theta,\varphi) = f(\boldsymbol{s})$, we can write:

$$f(\boldsymbol{s}) = -\frac{m_e e}{2\pi\hbar^2}\int e^{-is.r}V(r)d^3\boldsymbol{r}. \tag{1.26}$$

The differential cross-section, hence, the total scattering intensity, for the scattering is related to the scattering amplitude by the following expression:

$$\frac{d\sigma}{d\Omega} = |f(\boldsymbol{s})|^2. \tag{1.27}$$

1.5.2 Scattering amplitude due to a charge distribution

The potential in equation (1.26) depends on the molecular structure. The structure of the molecule depends on the position of the atoms, hence the nuclear position, and the distribution of electron density. For a total number of nuclear charge Z, the total charge distribution of an atom can be written at any point $\boldsymbol{r}'$ as[41]:

$$\rho(\boldsymbol{r}') = Ze\delta(\boldsymbol{r}') - e\rho_e(\boldsymbol{r}'). \tag{1.28}$$

The electrostatic potential can be written based on the total charge distribution as:

$$V(r) = \frac{1}{4\pi\varepsilon_0}\int d^3\boldsymbol{r}'\,\frac{\rho(r')}{|\boldsymbol{r}-\boldsymbol{r}'|} \tag{1.29}$$

$$= \frac{1}{4\pi\varepsilon_0}\int d^3\boldsymbol{r}'\,\frac{Ze\delta(\boldsymbol{r}')-e\rho_e(\boldsymbol{r}')}{|\boldsymbol{r}-\boldsymbol{r}'|} \tag{1.30}$$

$$= \frac{1}{4\pi\varepsilon_0}\int d^3\boldsymbol{r}'\,\frac{Ze\delta(\boldsymbol{r}')}{|\boldsymbol{r}-\boldsymbol{r}'|} - \frac{e}{4\pi\varepsilon_0}\int d^3\boldsymbol{r}'\,\frac{\rho_e(\boldsymbol{r}')}{|\boldsymbol{r}-\boldsymbol{r}'|}$$

$$V(r) = \frac{1}{4\pi\varepsilon_0}\frac{ze}{r} - \frac{e}{4\pi\varepsilon_0}\int d^3\boldsymbol{r}'\,\frac{\rho_e(\boldsymbol{r}')}{|\boldsymbol{r}-\boldsymbol{r}'|}. \tag{1.31}$$

Plugging equation (1.31) in equation (1.26) we can write:

$$f(\boldsymbol{s}) = -\frac{m_e e}{2\pi\hbar^2}\int e^{-is.r}d^3\boldsymbol{r}\left[\frac{1}{4\pi\varepsilon_0}\frac{Ze}{r} - \frac{e}{4\pi\varepsilon_0}\int d^3\boldsymbol{r}'\,\frac{\rho_e(\boldsymbol{r}')}{|\boldsymbol{r}-\boldsymbol{r}'|}\right]$$

$$= -\frac{m_e e}{2\pi\hbar^2}\frac{Ze}{4\pi\varepsilon_0}\int \frac{e^{-i\boldsymbol{s}.\boldsymbol{r}}d^3\boldsymbol{r}}{r} + \frac{m_e e}{2\pi\hbar^2}\frac{1}{4\pi\varepsilon_0}\int e^{-i\boldsymbol{s}.\boldsymbol{r}}d^3\boldsymbol{r}\int d^3\boldsymbol{r}'\,\frac{\rho_e(\boldsymbol{r}')}{|\boldsymbol{r}-\boldsymbol{r}'|}$$

$$f(\boldsymbol{s}) = -\frac{m_e e^2}{2\pi\hbar^2}\frac{Z}{4\pi\varepsilon_0}I_1 + \frac{m_e e}{2\pi\hbar^2}\frac{1}{4\pi\varepsilon_0}I_2. \qquad (1.32)$$

Equation (1.32) involves two integrals where-

$$I_1 = \int \frac{e^{-i\boldsymbol{s}.\boldsymbol{r}}d^3\boldsymbol{r}}{r} \qquad (1.33)$$

and,

$$I_2 = \int e^{-i\boldsymbol{s}.\boldsymbol{r}}d^3\boldsymbol{r}\int d^3\boldsymbol{r}'\,\frac{\rho_e(\boldsymbol{r}')}{|\boldsymbol{r}-\boldsymbol{r}'|}. \qquad (1.34)$$

Following the procedure shown in Ref [40] we can solve this integral. For equation (1.33)

$$I_1 = \int \frac{e^{-i\boldsymbol{s}.\boldsymbol{r}}d^3\boldsymbol{r}}{r} = \int_{r=0}^{\infty}\int_{\emptyset=0}^{2\pi}\int_{\theta=0}^{\pi}\frac{e^{-isrcos\theta}}{r}r^2 sin\theta dr d\theta d\emptyset$$

$$I_1 = 2\pi\int_{r=0}^{\infty} r dr \int_0^{\pi} e^{-isrcos\theta} sin\theta d\theta.$$

Here,

$$\int_0^{\pi} e^{-isrcos\theta} sin\theta d\theta = \frac{2\sin{(sr)}}{sr}.$$

Therefore,

$$I_1 = \frac{4\pi}{s}\int_{r=0}^{\infty}\sin(sr)\,dr \qquad (1.35)$$

Using the trick used in equation (1.39) at Ref([40]) we can write,

$$\int_{r=0}^{\infty}\sin(sr)\,dr = \frac{1}{s}.$$

Hence, from equation (1.35) we obtain,

$$I_1 = \frac{4\pi}{s^2}. \qquad (1.36)$$

Now we will solve $I_2 = \int e^{-i\boldsymbol{s}.\boldsymbol{r}} d^3\boldsymbol{r} \int d^3\boldsymbol{r}' \frac{\rho_e(\boldsymbol{r}')}{|\boldsymbol{r}-\boldsymbol{r}'|}$ following the similar procedure in Ref[40]). Changing the order of integral we find:

$$I_2 = \int d^3\boldsymbol{r}'\, \rho_e(\boldsymbol{r}') \int d^3\boldsymbol{r} \frac{e^{-i\boldsymbol{s}.\boldsymbol{r}}}{|\boldsymbol{r}-\boldsymbol{r}'|}. \tag{1.37}$$

To solve this integral, let's suppose, $\boldsymbol{\alpha} = \boldsymbol{r} - \boldsymbol{r}'$. From this relation we can write,

$$d^3\boldsymbol{\alpha} = d^3\boldsymbol{r}; \text{ and } e^{-i\boldsymbol{s}.\boldsymbol{r}} = e^{-i\boldsymbol{s}.(\boldsymbol{\alpha}+\boldsymbol{r}')} = e^{-i\boldsymbol{s}.\boldsymbol{\alpha}} e^{-i\boldsymbol{s}.\boldsymbol{r}'}.$$

Using these relations in equation (1.37)

$$I_2 = \int d^3\boldsymbol{r}'\, \rho_e(\boldsymbol{r}') \int d^3\boldsymbol{\alpha} \frac{e^{-i\boldsymbol{s}.\boldsymbol{\alpha}} e^{-i\boldsymbol{s}.\boldsymbol{r}'}}{\alpha};$$

$$I_2 = \int d^3\boldsymbol{r}'\, \rho_e(\boldsymbol{r}') e^{-i\boldsymbol{s}.\boldsymbol{r}'} \int d^3\boldsymbol{\alpha} \frac{e^{-i\boldsymbol{s}.\boldsymbol{\alpha}}}{\alpha}. \tag{1.38}$$

The 2nd integral in equation (1.38) is similar to equation (1.33), and its value can be found in equation (1.36). Using equation (1.36) in equation (1.38) we obtain,

$$I_2 = \frac{4\pi}{s^2} \int d^3\boldsymbol{r}'\, \rho_e(\boldsymbol{r}') e^{-i\boldsymbol{s}.\boldsymbol{r}'} \tag{1.39}$$

Plugging equations (1.36) and (1.39) in equation (1.32) we get

$$f(\boldsymbol{s}) = -\frac{m_e e^2}{2\pi\hbar^2} \frac{Z}{4\pi\varepsilon_0} \frac{4\pi}{s^2} + \frac{m_e e}{2\pi\hbar^2} \frac{1}{4\pi\varepsilon_0} \frac{4\pi}{s^2} \int d^3\boldsymbol{r}'\, \rho_e(\boldsymbol{r}') e^{-i\boldsymbol{s}.\boldsymbol{r}'}$$

$$f(\boldsymbol{s}) = -\frac{m_e e^2}{2\pi\varepsilon_0\hbar^2} \frac{1}{s^2} \left[Z - \int d^3\boldsymbol{r}\, \rho_e(\boldsymbol{r}) e^{-i\boldsymbol{s}.\boldsymbol{r}} \right] \tag{1.40}$$

Here in equation (1.40), we dropped all the primes from $\boldsymbol{r}$. Here the integral in equation (1.40),

$$F(s) = \int d^3\boldsymbol{r}\, \rho_e(\boldsymbol{r}) e^{-is.r} \tag{1.41}$$

describes the atomic form factor of X-ray scattering.

1.5.3 Scattering amplitude due an atomic model and ion

In this section, we will find the amplitude of electron scattering due to an atom with two special cases where the nuclear charge is screened by the electron cloud around it: so that the atom can be considered as neutral, and screening effect absent for which we will assume the atom is charged. The potential for the case of neutral atom can be approximated by the Yukawa Potential of the following form[37]:

$$V(r) = \beta \frac{e^{-\mu r}}{r}. \tag{1.42}$$

Where, μ and β are constant. As seen from equation (1.42), the potential decreases exponentially at a rate of μ. The strength of screening is characterized by the factor μ. From equation (1.26) we get

$$f(\boldsymbol{s}) = -\frac{m_e e}{2\pi\hbar^2} \int e^{-is.r} \beta \frac{e^{-\mu r}}{r} d^3\boldsymbol{r}, \tag{1.43}$$

$$f(\boldsymbol{s}) = -\frac{m_e e}{2\pi\hbar^2} \int e^{-is.r} \beta \frac{e^{-\mu r}}{r} r^2 dr \int sin\alpha d\alpha \int d\vartheta. \tag{1.44}$$

Since Yukawa potential is spherically symmetric so $\int d\vartheta = 2\pi$. From equation (1.44) we get,

$$f(s) = -\frac{m_e e\beta}{\hbar^2} \int \frac{e^{-\mu r}}{r} r^2 dr \int e^{-isrcos\alpha} sin\alpha d\alpha, \tag{1.45}$$

$$f(s) = -\frac{m_e e\beta}{\hbar^2} \int \frac{e^{-\mu r}}{r} r^2 dr \times \frac{2}{sr} \sin(sr), \tag{1.46}$$

$$f(s) = -\frac{2m_e e\beta}{\hbar^2 s} \int e^{-\mu r} \sin(sr) dr, \tag{1.47}$$

Using the table of standard integral solutions, we can have-

$$f(s) = -\frac{2m_e e\beta}{\hbar^2 s}\int e^{-\mu r}\sin(sr)\,dr = -\frac{2m_e e\beta}{\hbar^2 s}\frac{s}{\mu^2+s^2},$$

$$f(s) = -\frac{2m_e e\beta}{\hbar^2}\frac{1}{\mu^2+s^2}. \tag{1.48}$$

Equation (1.48) expresses the scattering amplitude for scattering with an atom where the nuclear charge is screened by the electron cloud. Since total scattering intensity,

$$I(s) = |f(s)|^2. \tag{1.49}$$

We can see that total scattering intensity for the neutral atom does not diverge at low s. This is due to the fact that Yukawa potential is a short-range force, so, $I(s)$ does not diverge as $s \to 0$ where impact parameter is high.

If the atom is an ion instead of neutral, we can think of the interaction of two charged particles in the scattering process. In this scattering, the potential can be regarded as a Coulomb potential of the form:

$$V(r) = \frac{1}{4\pi\varepsilon_0}\frac{q_1 q_2}{r} \tag{1.50}$$

Where, $q_1$and q_2 are two-point charges. Using the form of potential (1.50) in equation (1.26) and continuing as above, we can get

$$f(s) = -\frac{2m_e e}{\hbar^2}\frac{1}{4\pi\varepsilon_0}\frac{q_1 q_2}{s^2}. \tag{1.51}$$

Using equation (1.49) and (1.51),

$$I(s) \propto \frac{A}{s^4}. \tag{1.52}$$

Here, A is the constant and can be determined from equation (1.50). Equation (1.52) tells that the total scattering intensity diverges as $s \to 0$. This can be attributed to the long-range nature of the coulomb force. Regardless of the distance between the incident particles and the charge, there is always an influence on the motion of the particles, leading to their scattering.

1.5.4 Elastic scattering from a molecular ensemble

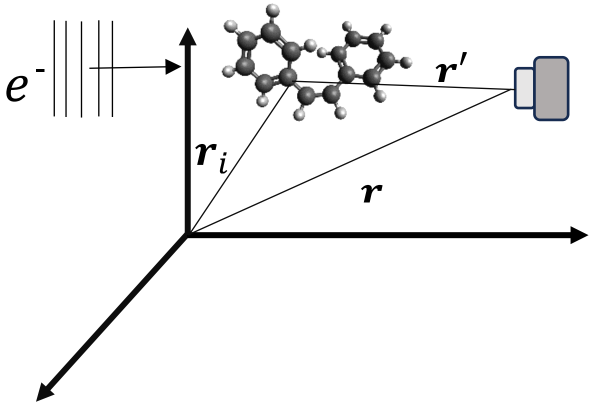

Figure 1.2: Representation of electron scattering by molecule using a coordinate system. A molecule is located at r_i, and a detector is located at a distance r' from the molecule. The diffraction pattern forms at the detector which is located at a distance r from the origin.

Now we will focus on calculating scattering intensity due to a random distribution of molecules. We assume that molecules are at a sufficiently large distance to each other so that they scatter independently. To calculate the total scattering intensity, we first calculate the scattering from a single molecule and then average over all molecules within the ensemble. When calculating the scattering intensity of a single molecule, we will assume that within a molecule, each atom has potential that is not disturbed by other atoms, and they preserve the spherical symmetry of the potential[42]. This assumption lays the base of the independent atom model (IAM). We can extend the elastic electron scattering in each atom within the molecule to calculate the elastic electron scattering of the whole molecule by summing the contribution of elastic scattering over the entire molecule. We will invoke the assumption here that the contribution of scattering from each atom within the molecule adds up coherently; however, the overall intensity of the ensemble is an incoherent sum of scattering from all molecules.

Let's now consider a molecule consisting of N atoms. As shown in Figure 1.2, we will first consider one atom located at a position r_i from the origin. The scattering is detected by a detector at a distance r from the origin. Then, the total elastic scattering form factor can be represented by

$$f_M(\boldsymbol{s}) = \sum_{i=1}^{N} f_i(s) e^{is.\boldsymbol{r}_i} \tag{1.53}$$

Where, $f_i(s)$ are the electron scattering form factor of i^{th} atom as presented by equation (1.40). Because the atom is located at a distance r_i from the origin, a phase term, $e^{is.\boldsymbol{r}_i}$, is included in equation (1.53). Additionally, although according to the first-Born approximation $f_i(s)$ are real, they can be indeed complex[43]. Hence, equation (1.53) takes the form:

$$f_M(\boldsymbol{s}) = \sum_{i=1}^{N} |f_i(s)| e^{i\eta_i} e^{is.\boldsymbol{r}_i}. \tag{1.54}$$

The total scattering intensity of the molecule will be

$$I_M(\boldsymbol{s}) = |f_M(\boldsymbol{s})|^2 = f_M(\boldsymbol{s}) f_M^*(\boldsymbol{s}) = \sum_{i=1}^{N} \sum_{j=1}^{N} |f_i(s)| e^{i\eta_i} e^{is.\boldsymbol{r}_i} \left|f_j(s)\right| e^{i\eta_j} e^{is.\boldsymbol{r}_j},$$

$$I_M(\boldsymbol{s}) = \sum_{i=1}^{N} \sum_{j=1}^{N} |f_i(s)|\left|f_j(s)\right| e^{i(\eta_i-\eta_j)} e^{i\boldsymbol{s}.(\boldsymbol{r}_i-\boldsymbol{r}_j)}. \tag{1.55}$$

In equation (1.55), we can split the summation based on two conditions: $i = j$ and $i \neq j$. For the first case equation (1.55) reduces to

$$I_{M_1}(\boldsymbol{s}) = \sum_{i=j=1}^{N} |f_i(s)|^2. \tag{1.56}$$

For the second case, we can write:

$$I_{M_2}(\boldsymbol{s}) = \sum_{i=1}^{N} \sum_{\substack{j=1 \\ j\neq i}}^{N} |f_i(s)|\left|f_j(s)\right| e^{i(\eta_i-\eta_j)} e^{i\boldsymbol{s}.(\boldsymbol{r}_i-\boldsymbol{r}_j)}. \tag{1.57}$$

Hence as a whole, equation 1.54 can be written as

$$I_M(\boldsymbol{s}) = \sum_{i=j=1}^{N} |f_i(s)|^2 + \sum_{i=1}^{N} \sum_{\substack{j=1 \\ j\neq i}}^{N} |f_i(s)|\left|f_j(s)\right| e^{i(\eta_i-\eta_j)} e^{i\boldsymbol{s}.(\boldsymbol{r}_i-\boldsymbol{r}_j)}. \tag{1.58}$$

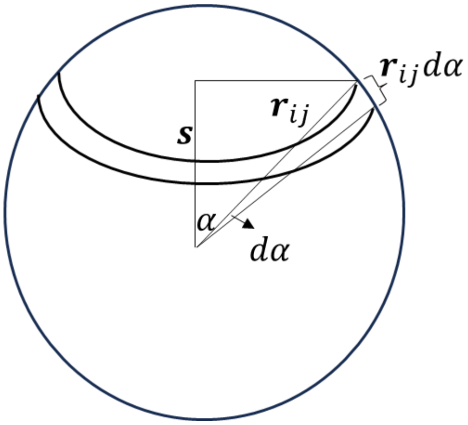

Figure 1.3: Identification of molecular orientation. Figure recreated from Ref [44].

Equation (1.58) gives the total scattering intensity of a rigid molecule at a fixed orientation, where we did not account contribution due to vibration, and we also assumed that molecule has motion that is negligible. In practice, when the scattering intensity is recorded on a detector for an ensemble of molecules, it is the average scattering intensity over all possible orientations, provided that all orientations have equal probability. As in Figure 1.3, the differential probability that the angle between $\boldsymbol{s}$ and $(\boldsymbol{r_i} - \boldsymbol{r_j}) = \boldsymbol{r_{ij}}$ falls between α and $\alpha + d\alpha$ is given by[44]

$$P_\alpha d\alpha = \frac{1}{2} sin\alpha d\alpha. \tag{1.59}$$

Thus, the overall scattering intensity due to the molecular ensemble will be

$$I(s) = \int I_M(\boldsymbol{s}) P_\alpha d\alpha \tag{1.60}$$

$$I(s) =$$

$$\int_{\alpha=0}^{\alpha=\pi} \sum_{i=j=1}^{N} |f_i(s)|^2 \frac{1}{2} sin\alpha d\alpha + \int_{\alpha=0}^{\alpha=\pi} \sum_{i=1}^{N} \sum_{\substack{j=1 \\ j\neq i}}^{N} |f_i(s)| \left|f_j(s)\right| e^{i(\eta_i - \eta_j)} e^{is.(\boldsymbol{r}_i - \boldsymbol{r}_j)} \frac{1}{2} sin\alpha d\alpha,$$

$$I(s) = \sum_{i=j=1}^{N} |f_i(s)|^2 + \frac{1}{2} \sum_{i=1}^{N} \sum_{\substack{j=1 \\ j\neq i}}^{N} |f_i(s)| \left|f_j(s)\right| e^{i(\eta_i - \eta_j)} \int_{\alpha=0}^{\alpha=\pi} e^{isr_{ij}cos\alpha} sin\alpha d\alpha \tag{1.61}$$

Where, we use $r_{ij} = r_i - r_j$. The integral in equation (1.61) is evaluated in the proceeding sections and can be written as

$$\int_{\alpha=0}^{\alpha=\pi} e^{isr_{ij}cos\alpha} sin\alpha d\alpha = \frac{2\sin(sr_{ij})}{sr_{ij}}. \tag{1.62}$$

Using equation (1.62) in equation (1.61) we get

$$I(s) = \sum_{i=j=1}^{N} |f_i(s)|^2 + \sum_{i=1}^{N} \sum_{\substack{j=1 \\ j\neq i}}^{N} |f_i(s)| \left|f_j(s)\right| e^{i(\eta_i - \eta_j)} \frac{\sin(sr_{ij})}{sr_{ij}}, \tag{1.63}$$

$$I(s) = \sum_{i=j=1}^{N} |f_i(s)|^2 + \sum_{i=1}^{N} \sum_{\substack{j=1 \\ j\neq i}}^{N} |f_i(s)| \left|f_j(s)\right| \cos(\eta_i - \eta_j) \frac{\sin(sr_{ij})}{sr_{ij}}. \tag{1.64}$$

$$I(s) = I_{at}(s) + I_{mol}(s) \tag{1.65}$$

Where,

$$I_{at}(s) = \sum_{i=j=1}^{N} |f_i(s)|^2 \tag{1.66}$$

$$I_{mol}(s) = \sum_{i=1}^{N} \sum_{\substack{j=1 \\ j \neq i}}^{N} |f_i(s)| \left|f_j(s)\right| \cos\left(\eta_i - \eta_j\right) \frac{\sin(sr_{ij})}{sr_{ij}} \tag{1.67}$$

Equation (1.66) is called the atomic scattering intensity and does not contain any structural information. The second term in (1.67) is called the molecular scattering intensity and contains the structural information.

The diffraction pattern is simulated using equation (1.64) in the gas phase ultrafast electron diffraction. For a molecule, the Cartesian coordinates are simulated by different optimization and simulation methods. The form and phase factors of atoms for the applied electron energy are generated using ELSEPA[45]. Using the form and phase factors, and the interatomic distances the total scattering intensity is calculated using equation (1.64).

1.6 Scattering beyond Independent Atom Model (IAM)

The Independent Atom Model (IAM), originally proposed by Debye[46] assumes that the total scattering of a molecule is the sum of the scattering from its constituent atoms. However, IAM has limitations; it does not account for important electronic effects, specifically the electron correlation effect and binding effect. Binding effect accounts for the electronic redistribution due to formation of chemical bond[47][48][49]. Binding effect contributes to elastic scattering. On the other hand, correlation effect appears due to Coulomb's repulsion and Pauli's exclusion between two electrons. Correlation effect accounts for the inelastic scattering[50][51]. In UED, the experimental scattering signal can consist of a signal corresponding to both electron and nuclear dynamics. This limitation of IAM becomes apparent when comparing IAM calculations to experimental data, especially when electron dynamics are involved. In such cases, the experimental scattering intensity departs from agreement with the IAM calculation, particularly at lower angles[52] [51][53]. IAM ignores the two above mentioned electronic effects and hence there is a discrepancy between the theoretical and experimental scattering signal at low s[47][51][52]. It was shown, even the IAM consider the electron correlation effect, it cannot agree with the experiment in case there is inelastic signal involved in the total scattering signal [51]**.** The electronic dynamics in UED has been seen in previous two studies[53][52]. Both studies showed that IAM fails to reproduce the signal at low s. To address these limitations, ab-initio calculations have been shown to reproduce the low-s signal accurately, unlike IAM[50][51]. In various theoretical studies, it has become evident that the drawbacks of IAM can be overcome through ab-initio calculations, highlighting the merits of the latter approach[57][55].

1.7 Frank Cordon principle

In the Born-Oppenheimer approximation, the nucleus is a massive object compared to electrons. The nucleus's position can be considered fixed during the fast electronic transition. Since the massive nuclei do not change position during the fast electronic transition, the transition can be represented by a vertical line on the energy vs. internuclear separation plot. The vertical line indicates the electronic transition without accompanying any nuclear geometrical change. Typically, the nuclear mass is about 10^4 times larger than the electronic mass. Because of this mass difference, the time scale of electronic transition to the motion of atom is also different. Atomic motion happens in a timescale of on the order of femtosecond $(10^{-15} fs)$ [58][59]. On the other hand, electronic motion happens $10^2 - 10^3$ times faster than atomic motion[60], in the attosecond domain$(10^{-18} fs)$ [61]. Hence, studying the electronic motion is made possible only width to advent of attosecond technology[62][63].

Due to transition, an electronic charge redistribution induces a change in coulomb force. This results in a change in the vibrational state of the nuclei. The probability of transition depends on the location of the nuclei. At the lower vibrational state, the transition probability is highest near the equilibrium internuclear separation. On the other hand, in an excited vibrational state, the probability of an end-of-transition is higher at classical turning points.

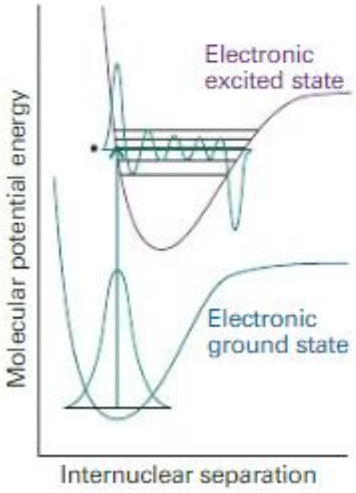

Figure 1.4: Molecular transition from the ground state to a higher vibrational state. The transition occurs in states in which the wavefunction resembles the wavefunction of ground state and has the greatest overlap in the overlap integral. Figure adapted from [64].

The probability of a photon is resonantly absorbed, and there is an electronic transition depends on the transition dipole moment that is expressed as

$$\boldsymbol{\mu}_{fi} = \int \psi_f^* \boldsymbol{\mu} \psi_i d\tau. \qquad (1.68)$$

Where, μ is the electric dipole moment operator, ψ_i and ψ_f are the wavefunction of initial and final states during the photoexcitation process, respectively. When we consider both electronic and vibrational transition, the wavefunction of each state can be considered as the product of electronic and vibrational wavefunction, i.e:

$$\psi_i = \psi_\varepsilon(\boldsymbol{r})\psi_v(\boldsymbol{R}) \text{ and } \psi_f = \psi_{\varepsilon'}(\boldsymbol{r})\psi_{v'}(\boldsymbol{R})$$

Here, ε and v label the electronic and vibrational states, respectively, and $\boldsymbol{r}$ and $\boldsymbol{R}$ are electronic and nuclear coordinates, respectively. From equation (1.68) we can write:

$$\boldsymbol{\mu}_{fi} = -e \int \psi_{\varepsilon'}(\boldsymbol{r})\psi_{v'}(\boldsymbol{R})\boldsymbol{r}\psi_{\varepsilon}(\boldsymbol{r})\psi_{v}(\boldsymbol{R}) d\tau_{elec}\, d\tau_{nuc},$$

$$\boldsymbol{\mu}_{fi} = -e \int \psi_{\varepsilon'}(\boldsymbol{r})\boldsymbol{r}\psi_{\varepsilon}(\boldsymbol{r}) d\tau_{elec} \int \psi_{v'}(\boldsymbol{R})\psi_{v}(\boldsymbol{R}) d\tau_{nuc}. \qquad (1.69)$$

Where, we used $\boldsymbol{\mu} = -e\boldsymbol{r}$**.** In equation (1.69) the nuclear coordinate dependent integral is called the overlap integral between the vibrational wave function of different electronic states

$$f_{vv'} = \int \psi_{v'}(\boldsymbol{R})\psi_v(\boldsymbol{R}) d\tau_{nuc} \qquad (1.70)$$

Equation (1.70) explains how there is an intense transition, and there is a weak or no transition in term transition probability. The better the overlap between the vibrational wavefunctions, the stronger the transition is.

1.8 Contribution of conical intersection

In the context of following and modeling the photochemical pathway from Frank-Condon point to ground state, conical intersection plays a crucial role in determining the photodynamics and end-products[65][66][67][68][69]. Conical intersections are points (or more precisely, hyperlines) where the adiabatic electronic potential-energy surfaces exhibit complete degeneracy in the many dimensional nuclear coordinate space of polyatomic molecules [70] . According to the Born-Oppenheimer approximation, nuclei move slowly because of their larger mass than electrons. When electron moves relative to the nuclei, nuclei can be assumed stationary compared to electron[64]. Hence, their respective wave functions can be treated separately. However, the electronic and nuclear dynamics couple together for polyatomic molecules, especially organic molecules, which have many degrees of freedom and many closely lying electronic states, and Born-Oppenheimer cannot hold anymore[71]. Photo dynamics in which Born-Oppenheimer approximation does not hold are called non-adiabatic dynamics[72]. In non-adiabatic dynamics, in which the nuclear kinetic energy is not excessive, potential energy surface (PES) can be used to describe the dynamics. In the context of photodynamics, after the photoexcitation of molecule, electrons transfer their energy to molecular vibration in an ultrafast process. Subsequently, a geometry is created in which at least two electronic states are isoenergetic and constitute a funnel-like shape in the PESs between two states[73], [74]. The uniqueness of conical interaction is it is a collection of geometries that makes a multidimensional seam on which each point facilitates the transition to the ground state[73]. The transition that happened through CI is a radiation less decay, and the decay occurs from the upper electronic state to the bottom electronic state through the funnel[75]. Previously, it was believed that the PES are avoided in the vicinity of the intersection, but it was shown in the recent work that the surfaces are actually unavoided at the intersection[68][76][77][78].

Conical intersection (CI) plays a crucial role in many photodynamic reactions as it governs the photochemical pathway and the end products.

To elucidate CI more, we can describe it based on the description given in ref [79]. If a molecular system has N number of atoms, then the number of nuclear coordinates is given by, $F = 3N - 6$. When the energy is plotted against these F nuclear coordinates, the two energy states are found to intersect along an $(F - 2)$ dimensional hyperline. Each point on this hyperline has the same energy. However, for the other two remaining coordinates, degeneracy canceled out. In the Figure 1.5, these two coordinates can be viewed as $\boldsymbol{x_1}$and $\boldsymbol{x_2}$. As we can see in Figure 1.5, the shape of the energy surface looks like a double cone.

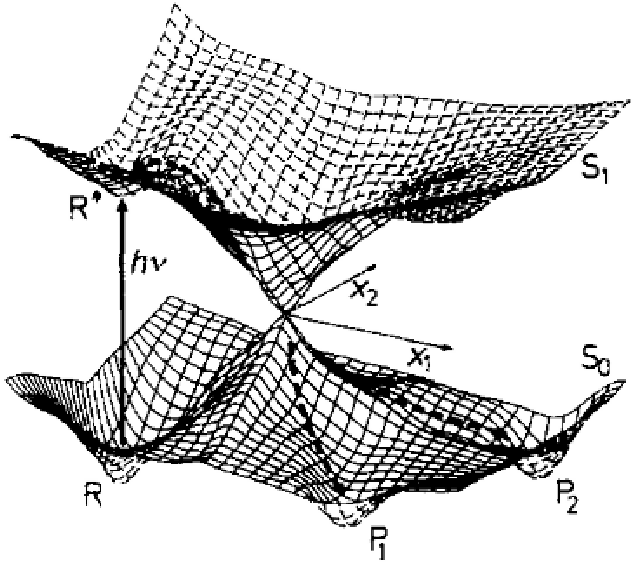

Figure 1.5: Identification of conical intersection. The potential energy surfaces of two states, S_0 and S_1 are schematically represented. After excitation the reactant, R produces R* in the excited state. R* follows the route on the excited state indicated by dashed line and produces P_1 and P_2. The plot reused from Ref[79] with permission.

$\boldsymbol{x_1}$ and $\boldsymbol{x_2}$ are used to characterize the CI. $\boldsymbol{x_1}$ is called the gradient difference vector, which is defined as $\boldsymbol{x_1} = \partial(E_0 - E_1)/\partial\boldsymbol{q}$, whereas $\boldsymbol{x_2}$ is called the nonadiabatic coupling vector and formulated as $\boldsymbol{x_2} = \langle\boldsymbol{\psi}_0|\partial\boldsymbol{\psi}_1/\partial\boldsymbol{q}\rangle$, where $\boldsymbol{q}$ is nuclear coordinate [79]. The difference between the upper and lower surface slope is maximum along $\boldsymbol{x_1}$. On the other hand, $\boldsymbol{x_2}$ represents the nuclear displacement direction that optimally mixes the two adiabatic wave functions' states at the cone point.

According to Figure 1.5, in a photoreaction, after absorption of a photon, the molecule is excited to the Frank-Cordon point. From there, the molecule moves on the surface towards the minimum following classical trajectory. During the passage, the molecule cannot jump on the lower surface as the energy difference is high. Eventually, the molecule arrives at the CI, where the energy difference is very small, and the probability of transition is maximum. Trajectories passing precisely through the cone tip proceed smoothly, converting electronic energy into nuclear motion along the steep slope of the cone wall. Trajectories missing the cone tip have a probability of either staying on the upper surface or jumping to the lower surface.

The type of photo product and their quantum yield depends on the CI. There are several factors that control the dynamics in the CI of a molecule. These include the accessibility of the CI, substituent on the molecules, density of states, and the floppiness of the molecules[80]. These factors affect the motion along $\boldsymbol{x_1}$ and $\boldsymbol{x_2}$, and hence the overall photochemistry.

1.9 Electron diffraction vs X-ray diffraction

The quantum particle cannot be viewed directly by using optical devices[39]. The only way to visualize them is to use techniques like scattering. Currently, two methods are intensively used: electron diffraction and X-ray diffraction. The main difference between these two diffraction methods and their experimental improvement is given in Ref[81][82]. To summarize a few key difference we can first talk about that electron diffraction has a million times greater cross-section in elastic scattering[83]. Currently, in the UED, the typical energy used for electron's acceleration is of the order of a few tens of KeV or higher, which corresponds to a de Broglie wavelength of pm or lower, whereas in the X-ray diffraction, typically the wavelength used in the order of an Å or less. In this case, UED can have a better spatial resolution than X-ray diffraction. Compared to X-ray diffraction, electron diffraction is more sensitive to the hydrogen atoms dynamics [82]. Electrons are negatively charged; hence, the space charge effect in the electron pulse hinders attaining a higher bunch charge and shorter pulse duration. The probability of radiation damage in UED is much lower than in X-ray diffraction [84]. In the modern world, the development of X-ray free electron lasers has enabled the generation of high-intensity X-ray pulses with shorter durations. This advancement has made it possible to study the diffraction of solids and gas-phase materials with greater efficiency[85]. Likewise, the space charge issue and velocity mismatch problem are overcome using a highly energetic RF photoinjector that made electron diffraction another potential candidate for structural analysis. Technological improvement has been made to improve spatial and temporal resolution in both UED and X-ray diffraction. The gas phase MeV UED has temporal resolution of 150fs and spatial resolution of 0.60Å[74][28][26][27]. The lower cross section in X-ray diffraction is compensated by a very highly bright X-ray pulse. In SLAC at LCLS facility, the X-ray photon has energy ranging from 1-25KeV which facilitates the analysis of experimental data in real space and brings up a sub-Å spatial resolution[86]. X-ray scattering possesses a superior temporal resolution since the temporal resolution is only dependent on the pulse duration of the pump and probe pulses and their synchronization. With appreciable synchronization, temporal resolution of 10-100fs is routinely achieved[87][88][86].

Chapter 2

UV-Induced Ring Conversion Reaction of Quadricyclane Studied by Ultrafast Electron Diffraction

2.1 Preface

In this chapter, I will talk about the photoreaction of quadricyclane (QD) by pumping QD with 200nm photons. The reaction involves the ring conversion dynamics of QD, which converts the highly strained three-membered ring (QD) to less strained norbornadiene (NB). This experiment was done at the SLAC National Accelerator Laboratory in 2020 during MeV-UED Run 2. I wasn't directly involved in conducting the experiment or physically present during data acquisition. Nevertheless, I contributed remotely to real-time data analysis during the beamtime. The initial analysis was conducted by Dr. Pedro Nunes, a former postdoctoral research associate in our group. All the analyses presented in this chapter were performed by me. The project is still running. I will discuss the commercial and scientific interest of this research. Since no diffraction-based structure-sensitive probe has been reported, I will describe our research goal and motivation by comparing other research done on QD. I will present the data analyzed so far, offer initial interpretations of our analysis, and outline our plan for further investigation.

2.2 Introduction

In the next twenty-five years, global energy demand is expected to double; by the end of this century, this demand will triple[89]. The excess demand for energy by 2050 is attempting to be met using carbon-neutral energy sources like biomass and nuclear energy plants; however, these sources suffer from low efficiency[90] and need acceptance by a significant portion of the public[89]. The necessity of keeping the CO_2 as low as possible to control the emission of greenhouse gases and, hence, reducing the risk of perturbing the large ecosystem, pushing us toward a greater reliance on renewable energy sources[91]. Among various renewable energy sources, sunlight stands out as a critical resource, harnessed through methods like solar panels or using it directly for heating. Solar energy has the capability to meet the ongoing global energy demand[92]–[94], however, solar energy presents a unique challenge because it varies with the time of a day and weather. To address this, we need 'load leveling' techniques to ensure a steady supply[95].

While we can store electricity using batteries, this approach has cost related issues and is not feasible for large-scale deployment. An exciting alternative is to directly convert solar energy into chemical energy. This conversion could involve making hydrogen from water or turning carbon dioxide into methanol[96], although these processes include gases.

Another promising avenue is using what we call 'molecular solar thermal' (MOST) systems. These systems use special molecules that can change their structure when exposed to sunlight, storing energy in the process. Later, by heating them or triggering a chemical reaction, we can release this stored energy. Scientists have explored various molecules for this purpose, such as azobenzenes [97]–[99], stilbenes [100], [101], and norbornadiene-quadricyclane (NB-QD) systems[102][103][104].

To be practical for MOST applications, these molecules must meet certain criteria[104][103][105]. First, they should absorb sunlight efficiently, matching the solar spectrum. Second, there is a need to balance the stored energy and the molecular size to result in a higher stored energy density. (iii). Third, they need a way to release the stored energy, which can be achieved through a catalytic reaction. Additionally, they should convert sunlight to energy with high efficiency, remain cost-effective, and have a high yield. The quadricyclane (QD): Norbornadiene (NB) interconversion has garnered a lot of recent interest as a molecular solar energy storage medium [1,2]. The molecule releases a considerable amount of energy as it converts from the QD structure to the NB structure. The stored energy can be released into heat using light or a catalyst.

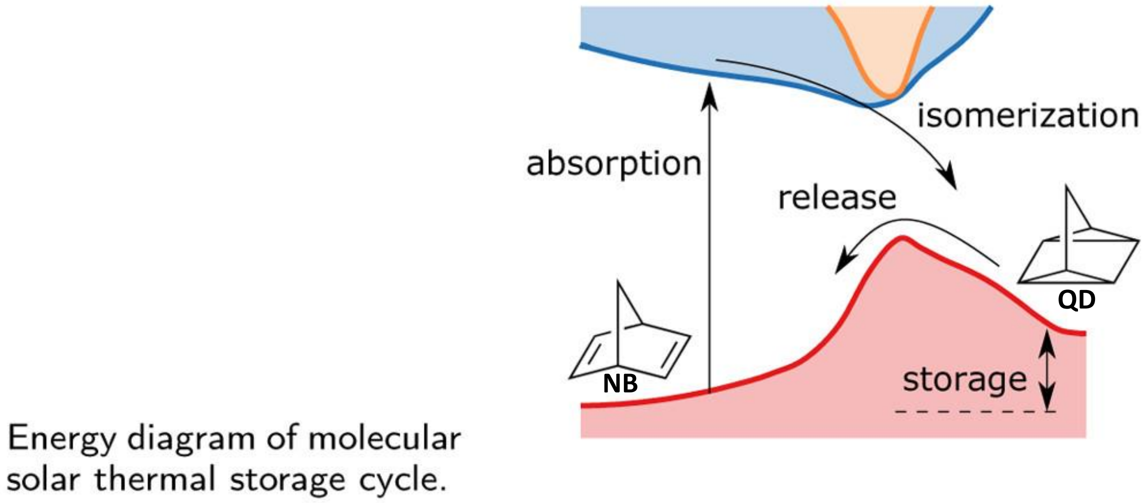

Figure 2.1: Energy diagram of QD-NB interconversion reaction. Isomerization of NB to QD facilitates storage of energy in QD, which then can be released by light-induced reaction from QD to NB. This figure is reused[1] with permission from ref [106].

QD:NB system is an ideal candidate for the application of MOST system as it meets most of the requirements outlined here [107]. It has a low molecular weight of 92.14 g/mol.

---

[1] The reference used from https://pubs.acs.org/doi/10.1021/acs.jpcc.5b11489. Further permission related to the material excerpted should be directed to the ACS.

When NB absorbs light, it can isomerize to QD and store appreciable energy of 146kJ/mol[107]. As seen in Figure 2.1, there is a clear energy difference between NB and QD isomers, and a considerable energy barrier separates the isomers. The energy barrier between two isomers is 96kJ/mol, which inhibits the thermal back reaction[107] spontaneously. A close-bomb calorimeter was used to determine the enthalpy for QD→NB isomerization in the solution phase, and the value was determined -89.03 ± 1.18 kJ/mol[108]. Additionally, the half-life of QD is of the order of a hundred years. By using UV light or catalyst, the back reaction from QD to NB can initiate, which releases the stored energy in it, which makes it an ideal candidate for the MOST application.

The objective of this study is to employ UED to capture both electronic and nuclear dynamics in real time. By obtaining high-resolution structural information, it will be possible to validate Woodward-Hoffman rules to understand and predict the outcomes of a wide range of photochemical reactions, especially those involving ring conversion. The Woodward-Hoffmann rules were formulated by American chemists Robert Woodward and Roald Hoffmann in the 1960s. These are a set of empirical principles that describe the permissibility and stereochemistry of pericyclic reactions. The rules are developed based on orbital symmetry and are particularly relevant in the context of organic chemistry. They also define which reactions are allowed and which are forbidden. This research seeks to significantly enhance the understanding of these reactions, which are crucial in organic synthesis, natural product formation, pharmaceutical synthesis, and other commercial applications like MOST application as outlined above.

2.3 Literature review

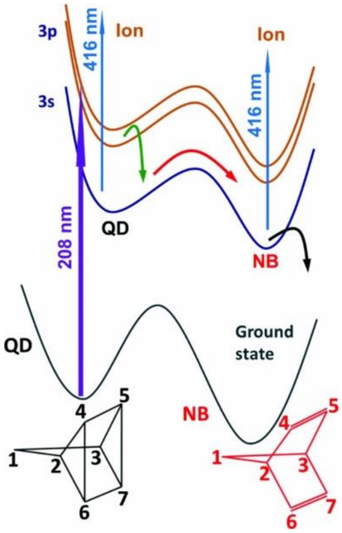

Figure 2.2: Photoreaction scheme for the pump-probe reaction and relaxation of QD. The photoexcitation was initiated by a 208nm photon, and molecular dynamics was probed by another 416nm photon. Figure reused from ref [109] with permission from AIP publishing.

The electronic excitation of QD, a highly strained three-membered ring, causes the excitation energy to distribute among its various degrees of freedom[109], which then leads to the formation of NB with less strained five and six-membered rings. The reaction follows an ultrafast mechanism, occurring within a few hundred femtoseconds, as evidenced in a prior photoelectron spectroscopy experiment conducted by Rudakov et al.[109]. The reaction scheme can be seen in Figure 2.2. In this experiment, ground state QD was excited by a 208nm pulse which populates 3s, $3p_x$, $3p_y$, and $3p_z$ Rydberg states. A time delayed probe pulse of 416nm was used to photo ionize the excited-state QD from the Reydberg states to ionic states. The ejected electrons during ionization are collected in a detector and used to analyze the data. Various time constants were determined by fitting the experimental time-dependent photoelectron spectra along different features using mathematical models. An internal conversion of the excited QD brings the molecule to 3s state in a time constant of 320fs. Energy analysis showed that QD does not possess enough energy in the 3p state to cross the energy barrier to isomerize to NB. However, the available vibrational energy in 3s state suffices the crossing of the energy barrier; hence, isomerization only happens in 3s state. By fitting the experimental features found in the TRPES spectra, the time constant calculated for isomerization is 136fs. From this excited state, NB relaxes to a lower-lying state at 394fs. The ground state dynamics could not be observed because the energy of the probe pulse (416nm=2.99eV) was much lower than the ionization potential (7.65eV) for ground state to ion-state transition. This study provided a time frame for the different steps of photoreaction. Our objective is to employ UED to obtain the time-dependent structure at various stages of the photoreaction.

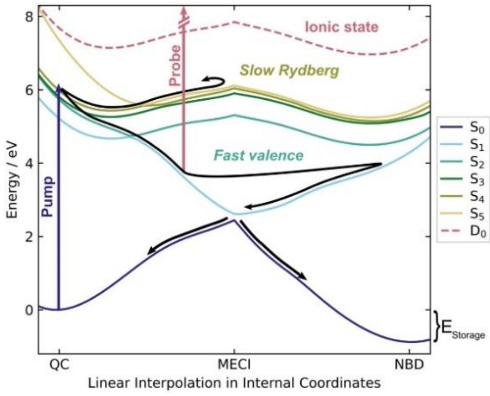

Figure 2.3: Potential energy curves for different electronic excited states and ground states. The figure adapted from ref [110] with permission.

Very recently, another study on photodynamics of quadricyclane was carried out by Borne and Cooper et al.[110]. They pumped the gas-phase QD by 200nm photon and probed it by time-resolved XUV photoelectron spectroscopy (TRPES). The dynamics was simulated using Root Mean Square Complete Active Space Second Order Perturbation Theory (RMS-

CASPT2) based on State-Averaged Complete Active Space Self-Consistent Field (SA (9)-CASSCF (2,6)) with the 6-31G(d) basis Two competitive pathways were observed for relaxation to the ground state. The faster pathway follows the initial excitation to an electronic state that has a mix of valence and $3p_x$ Rydberg state character. In Figure 2.3, this state is labeled as S_2 and relaxes to ground state via S_1 state in <100fs. The slower pathways are associated with the initial excitation to the $3p_y$ and $3p_z$ Rydberg states. They are labeled as S_3 and S_4 in Figure 2.3. The relaxation from these states also occur through the S_1 state but at a time scale of several hundreds of femtoseconds. Both relaxation pathways facilitate an interconversion with a branching ration of QD: NB of approximately 2:3. However, TRPES is not sensitive to different isomers in photoreaction. So, the prediction done by the MD simulation could not verified experimentally. Since UED is structure sensitive and reveals the structure of the isomers after a photoreaction[52], it is an obligatory tool for validating the end product ratio. Additionally, we aim to reveal the dynamics of QD experimentally using UED's spatiotemporal sensitivity.

2.4 Research goal

We have several goals for this research. Firstly, we aim to investigate the evolution of molecular structure on the excited potential surface at different stages of the dynamics. Additionally, we will explore whether structural evolution plays a role in determining the timescale of the dynamics. Furthermore, our goal is to understand the process of isomerization, identify the structure of the resulting hot NB product, determine the final ratio of QD to NB formed during the photo reaction, and investigate the presence of other potential reaction pathways, such as dissociation.

2.5 Methodologies

In this section, I will give an overview of the SLAC MeV-UED beamline and describe how the experimental data is processed for further analysis. The relativistic electron paved an way to determine the molecular structure and reveal the dynamics with a temporal resolution of 150fs, spatial resolution of 0.63Å, momentum space resolution 0.22Å^{-1}[26].

2.5.1 Instrumentation

Figure 2.4 shows the beamline used for gas phase MeV-UED experiments at SLAC. Details about the apparatus and procedures are described in the earlier reports[25], [26].

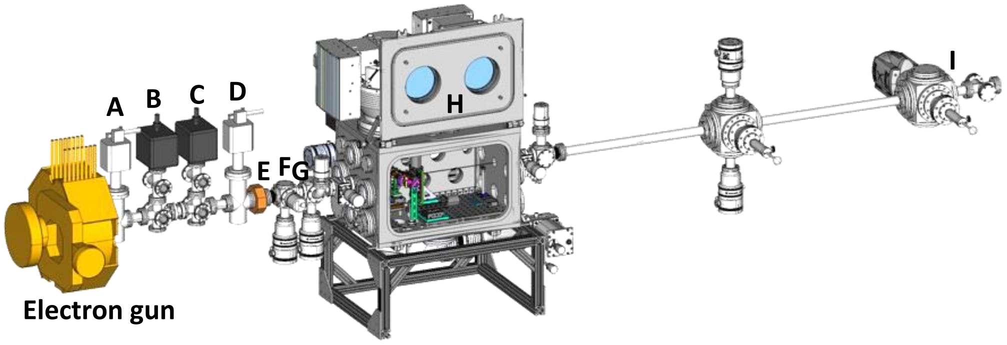

Figure 2.4: Experimental MeV-UED beamline at SLAC national accelerator laboratory. Here, A: Gun gate valve, B: e-beam diagnostic assembly, C: differential pumping assembly, D: sample gate valve, E: micro-focusing coil, F: differential pumping, G: incoupling optics, H: Sample chamber, I: Detection chamber. Figure courtesy: Pedro Nunes, Diamond Light Source, Didcot, United Kingdom.

As seen in Figure 2.4, the key component in the beamline is a radio frequency (RF) photocathode powered by a 1.6-cell S-band klystron. Electrons are generated by the photoemission process by directing 3% of the total output from a Ti: Sapphire laser system and after generating 267nm light. The laser system generates 800 nm pulses with a pulse duration of 70fs and a repetition rate of 180 Hz and 360Hz. The photoemitted electrons are accelerated to 3.7 MeV energy and focused into the interaction zone in the sample chamber. After the RF photoinjector a gate valve is located to protect the electron gun. An electron beam profile monitor is located in a diagnostic cube. A Faraday cup is also housed in this cube to measure the charge in an electron pulse. Fixed-size apertures are mounted on a motorized collimator to manipulate the electron beam size and current. The cross after the diagnostic cube contains two differential pumping sections, which gives an appreciable vacuum isolation between the upstream and downstream of the beamline. Next in the beamline, there is a sample gate valve. The gun gate valve and sample gate valve are coupled with a safety interlock, which closes the valves in case there is a pressure rise in the sample chamber and protects the electron gun from contamination. In the beamline, a microfocussing solenoid is used to further manipulate the electron beam. Moving further downstream, another cube is located which contains another differential pumping to further isolate the vacuum sections. The incoupling optics is housed in a cube to direct the pump laser beam toward the sample chamber. The incoupling optics contains a 45° holey mirror so that an electron beam can pass through this toward the sample chamber. The electron beam is introduced in the interaction point by using a movable capillary, which also offers differential pumping so as not to contaminate the coupling optics. A computer-controlled three-dimensional stage is used to position the gas nozzle, and, in some cases, a solid-state sample such as Bi_2Te_3 is placed just beneath the gas nozzle. The solid-state sample located under the gas nozzle is used to find the time zero conveniently before taking data with the experimental gas-phase sample. For gas phase UED, depending on the nature of the gas and signal-to-noise ratio, different types of continuous flow or pulsed flow nozzles are used. For catching the exhausted sample after interaction with the pump laser and probe electron beam, a cold trap is located under the nozzle. The cold trap is cryocooled to a temperature of 77K.

At 3.2m from the interaction point, another cube contains a phosphor screen to capture the diffraction image. The phosphor screen contains a hole in the middle so that un-diffracted electron beam can pass through and does not damage the phosphor screen by oversaturation. A high reflective mirror is located behind the phosphor screen to reflect the photons generated in the phosphor screen towards the Andor iXon 888 electron-multiplying charge-coupled device (EMCCD) camera. Another EMCCD camera which is coupled with another phosphor screen is located for capturing the un-diffracted electron beam. These un-diffracted electrons are used for diagnosing any steering of the electron beam due to surrounding condition or plasma effect that appears due to the interaction with laser and gas.

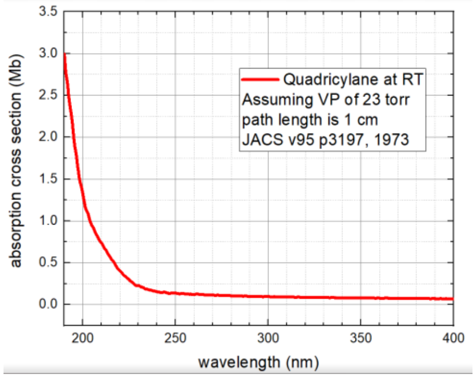

Figure 2.5: Absorption cross section of Quadricyclane measured at room temperature. The measurement was done by Dr. Ming-Fu Lin, during the UU031 beamtime. The figure is adapted from the SLACK channel used for communication during the beamtime.

Figure 2.5 shows the absorption cross section of QD for different wavelengths. Consistent to the previous studies, we wish to pump the QD using 200nm photon. The major portion of the output of the laser system produces a 200nm pump by using a frequency mixing process. The pump beam is directed towards the interaction region by the incoupling optics and traverses the sample with the electron beam almost collinearly. This colinear traversal of electron and pump beam suppresses the velocity mismatch and hence reduces the temporal blurring.

2.5.2 **Diffraction image processing**

The image obtained directly from the EMCCD camera usually contains noise of different types. By properly processing them, we can improve the signal-noise ratio, hence sharpening the signal. In this section, I will describe the processing of the raw diffraction images before using them for further analysis.

1. For a particular run, first, the total count of each image is determined and plotted against the lab time. Any image that has a significantly smaller number of counts than the average count is discarded.
2. Diffraction images are recorded for a number of delay points. Each delay point has multiple images. All the images are sorted out based on the delay point.
3. A threshold is set to remove hot pixels or saturated pixels. These hot pixels result from X-ray hits or permanently damaged pixels. Anything above the threshold is set as ‘not a number (NAN)’.
4. The average intensity and standard deviation for each pixel across all the images at a specific time delay point are computed. Pixels with intensities exceeding three

times the standard deviation from the average value are identified. These pixels are considered as "bad pixels" and are set to NAN.

5. The diffraction can also contain a dark current. All the dark current, leakage current, and central hole on the phosphor screen is masked to set NAN.
6. Since the phosphor screen is circular and the detector is rectangular, we took the mean of the counts found outside of the circular phosphor screen on the detector to get the base count. This base count is subtracted from the diffraction image.
7. At this point, all the images of each delay point are averaged, and the diffraction center is calculated for the averaged image.
8. Using this center, azimuthal average and standard deviation are calculated for each diffraction image. Any pixel that has a count of more or less than three standard deviations is ignored.
9. For each diffraction image, all the NAN are filled by the azimuthal average at that pixel point, and a median filter of 5x5 window size is applied. This filters out the ‘salt and pepper’ type noise.
10. All the NANs are put back in the pixels, where filling was done in the previous step, and the diffraction center is recalculated on the average image of each time point.
11. The diffraction centers of all the delay stages are averaged and used while doing the azimuthal average to get the 1-dimensional total scattering intensity from processed diffraction image.
12. The uncertainty is calculated by standard bootstrapping procedure. We will discuss the details about the bootstrapping in section 3.2.6.

2.6 Relevant theory for data analysis

In section 1.5.4, we derived the total scattering intensity for a randomly oriented molecular ensemble. In this section we will formulate only the relevant formulas which we will be using for analyzing our data. The static signal is analyzed by using modified scattering intensity and it is expressed by,

$$sM(s) = s\frac{I_{mol}(s)}{I_{at}(s)}. \tag{2.4}$$

Where $I_{mol}(s)$ and $I_{at}(s)$ are given by equations (1.67) and (1.66), respectively. The Fourier sine transform of equation (2.4) gives the pair distribution function in real space.

$$PDF(r) = \int_0^{s_{Max}} sM(s)\sin(sr)\,e^{-ds^2}\,ds \tag{2.5}$$

Here, d is a damping factor that removes the edge effect by damping the sM at higher s. The PDF shows peaks corresponding to the interatomic distance of different atom pairs. For time-dependent analysis, we use change in diffraction signal relative to the diffraction signal of the ground state structure. We calculate the percentage difference signal which is expressed as

$$\frac{dI}{I}(s,t) = \frac{I(s,t>0)-I(s,t<0)}{I(s,t<0)}. \tag{2.6}$$

Where, $I(s,t>0)$ is the total scattering intensity after the excitation by pump beam and $I(s,t<0)$ is the total scattering before pump beam hit the sample. One convenience in using the percentage difference signal is it is self-normalized and unitless. Another method used in time dependent signal analysis is using difference-modified scattering intensity as expressed by

$$\Delta sM(s,t) = \frac{I_{mol}(s,t>0) - I_{mol}(s,t<0)}{I_{at}(s)} s = \frac{I(s,t>0) - I(s,t<0)}{I_{at}(s)} s. \tag{2.7}$$

Where, I_{at} is a function of s only and does not depend on time since it does not carry any structural information. Hence, it does not contribute to structural evolution. In real space, time dependent analysis is done by using the difference in pair distribution function which is expressed as

$$\Delta PDF(r,t) = \int_0^{S_{Max}} \Delta sM(s,t) \sin(sr)\, e^{-ds^2} ds. \tag{2.8}$$

A bleach in ΔPDF in a particular r means a change of internuclear distance from that r. Conversely, the gain in ΔPDF at another r indicates that two atoms have new internuclear distance equals the value of that r.

2.7 Results and discussions

This section discusses the diffraction data analysis and our interpretation of the analysis. We will start by discussing the static diffraction data. This data will give us confirmation about using the right molecule in the experiment and identifying different internuclear distances in QD. After static data analysis, we will proceed with the time-dependent data analysis of our UV-induced UED data. We will discuss and interpret the temporal evolution of scattering signal with the aid of available simulation.

2.7.1 Static data analysis

We analyze Static data based on modified scattering intensity (sM) and pair distribution function (PDF). For static, diffraction data are recorded for the delay points where electrons are scattered by the molecule before pump pulse excite them. So, the ground state structural information can be extracted by static data analysis.

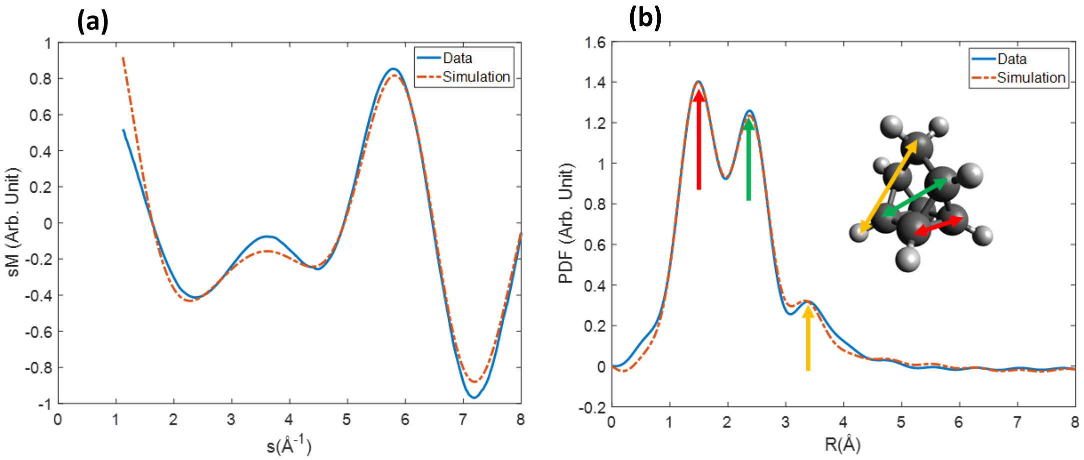

Figure 2.6: Static diffraction signal analysis of QD. (a) Experimental and simulated modified scattering intensity as sM. (b) Pair distribution function (PDF) obtained by the Fourier sine transform of sM. In both figures, the experimental signal agrees well with the theoretical calculation.

Figure 2.6a shows the modified scattering intensity, sM of both experimental and theoretical data. In the sM, each pair of atoms gives a waveform whose amplitude is proportional to the product of their atomic form factors and inversely proportional to their internuclear distance[111]. Theoretically, the total scattering intensity is calculated from an optimized ground state structure of QD. The optimization was done using B3LYP def2-SV(P) basis function. Experimentally, the total scattering intensity is extracted from the diffraction image by azimuthally averaging the image. Then the sM is calculated by the method, called 'zero fitting method', described in Ref[111]. In this method, experimental total scattering intensity is plotted against the s-values, where theoretical sM is zero. This intensity vs s curve is fitted by an exponential decay function which gives the background that contains atomic scattering intensity and other backgrounds. This fitted background (I_b) is then subtracted from the total experimental scattering intensity. Using equation (2.4), experimental sM is determined. Mathematically,

$$sM_{expt}(s) = \frac{I_{total}(s) - I_b(s)}{I_{at}(s)} s \tag{2.9}$$

Here, $I_{tot}(s)$ is the total experimental scattering intensity, $I_b(s)$ is the background scattering that includes atomic scattering, detector and other experimental background. I will discuss more about the zero-fitting method in section 3.2.3.

In Figure 2.6a, the experimental and theoretical sM shows a good agreement. The Fourier sine transform of sM using equation (2.5) gives the $PDF(r)$. In Figure 2.6b, the blue solid line gives the $PDF(r)$ for experimental data and red dotted line represents the theoretical $PDF(r)$. The experimental and theoretical $PDF(r)$ are also in good agreement. Two major peaks are seen at 1.49Å and 2.40Å. These peaks represent the interatomic distances in the QD as indicated by the colored arrows on the structure in the inset. Additionally, another peak is being seen at 3.4Å, which we believe is due to the C-H distance as shown by the yellow arrow.

Since the experimental sM(s) and $PDF(r)$ have good agreement with the theoretical counterpart, we can say that we did use QD in the experiment. Moreover, we calculated the detector pixel-to-s calibration value of 0.0248Å^{-1} by obtaining best fitting between the theoretical sM and experimental sM for different pixel-s-calibration value. One another important parameter we can extract from the static analysis is the spatial resolution. The experimental $sM(s)$ and theoretical $sM(s)$ agrees well upto $s_{Max} = 8\text{Å}^{-1}$, hence the spatial resolution for this experiment can be calculated as[26]:

$$\delta = \frac{2\pi}{s_{Max}} = 0.79\text{Å}.$$

2.7.2 Time-resolved data analysis

The structural evolution and excited state dynamics can be elucidated through the analysis of time-dependent signals. In this section, our emphasis lies in the investigation of time-resolved data to discern the intricate dynamics at play. The temporal characteristics are assessed utilizing the percentage difference signal of scattering intensity, as defined in equation (2.6). Comparative analysis of experimental data with theoretical simulations enables an in-depth exploration of electronic and nuclear dynamics. Analyzing the simulation facilitates the determination of the temporal correlation between nuclear dynamics and arrival to the conical intersections by the photoexcited molecule. Comparing the time resolved characteristics with the simulation counterpart ultimately permitting the extraction and quantification of end-products and their respective ratios.

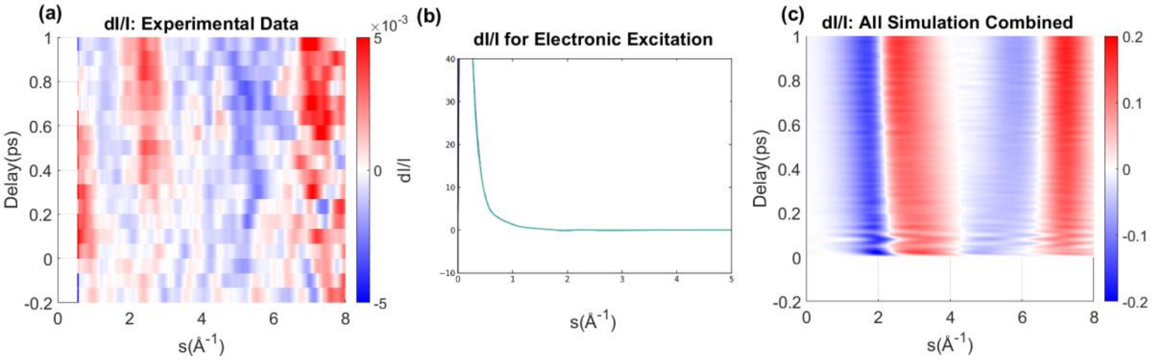

Figure 2.7: Time-dependent diffraction signal in term of difference-diffraction (dI/I) signal.Experimental 2D $\frac{\mathrm{dI}}{\mathrm{I}}$. Here, the data is convolved with a 100fs Gaussian in time. (b) $\frac{\mathrm{dI}}{\mathrm{I}}$ calculated for a single geometry with and without electronic excitation and by performing ab-initio scattering calculation. The sharp rise at low s validates that the signal at low s in experiment is due to electronic dynamics. (c) 2D $\frac{\mathrm{dI}}{\mathrm{I}}$ calculated from simulated trajectories using IAM. Because IAM is insensitive to the electronic contribution, the signal at low s is missing in this plot.

Figure 2.7a shows the two dimensional $\frac{dI}{I}$ for the experimental data to show the time dependent scattering signal. Here the horizontal axis shows the magnitude of the momentum transfer vector s, and the vertical axis shows the pump-probe delay. In this plot, a sharp signal arises at the low s, decaying after a few hundred femtoseconds. A similar signal was seen in a previous gas phase UED experiment[53], which was attributed due to inelastic electronic scattering.

To validate if the low s signal is due to electronic dynamics, we optimized a QD structure, calculated the total scattering signal with and without electronic excitation using ab-initio scattering calculations. We collaborated with Professor Adam Kirrander's group at the University of Oxford, who aided us with necessary simulation to interpret our experimental data. Joe Cooper in Professor Kirrander's group calculated the scattering signal using ab-initio scattering calculation. The $\frac{dI}{I}$ is then calculated and shown in Figure 2.7b. A clear sharp rise at low s is seen due to electronic excitation which validates our interpretation of seeing signal due to electronic dynamics in our experimental data. Moreover, in Figure 2.7a, clear pump-probe signal is seen at higher s, which is due to nuclear dynamics. In Figure 2.7c, we can see the simulated 2D $\frac{dI}{I}$. Joe Cooper also simulated 235 trajectories using RMS-CASPT2 based on SA(9)-CASSCF (2,6) with the 6-31G(d) basis. Each trajectory contains 2000 time-dependent structures from 0 to 1000fs at an interval of 0.5fs. We calculated the scattering signal from the structures in the trajectories using IAM. We calculated $\frac{dI}{I}(s,t)$ for all the trajectories using equation (2.6) and averaged them. As discussed in section 1.6, IAM assumes the total scattering of a molecule is the sum of scattering of all constituent atoms. The drawback of IAM is it cannot take into account the electronic correlation effect or rearrangement[53]. Because of this limitation we cannot see the electronic contribution on dI/I in Figure 2.7c. However, if we look at the features at larger s that correspond to nuclear dynamics, we can see a good qualitative agreement between experiment and simulation in Figures 2.7a and 2.7c, respectively.

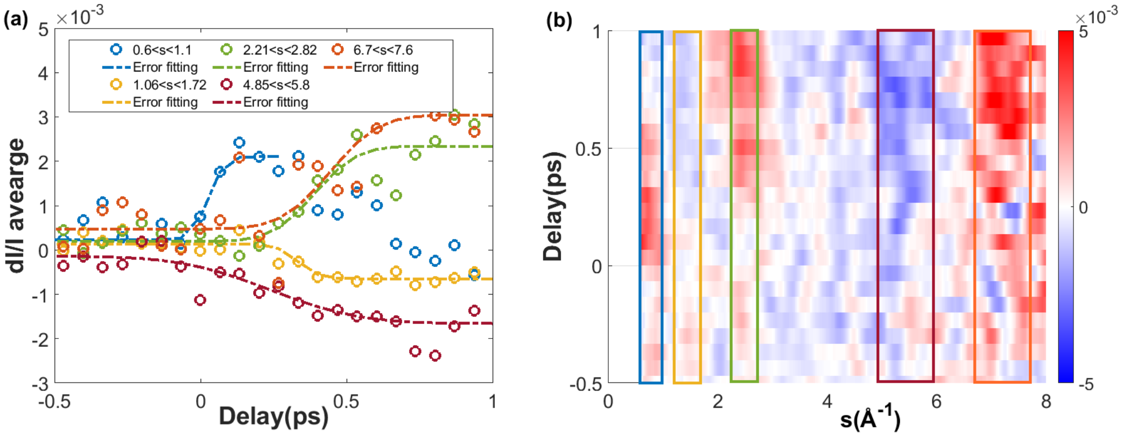

Figure 2.8: Time dependent lineout of experimental $\frac{\mathrm{dI}}{\mathrm{I}}$. (a) $\frac{\mathrm{dI}}{\mathrm{I}}$ is averaged over a certain window shown in (b). The averaged $\frac{\mathrm{dI}}{\mathrm{I}}$ is then plotted as a function of pump-probe delay. Each lineout is fitted by an error function which is represented by dash line. The low s signal has onset well before the onset of higher s signal. (b) 2D $\frac{\mathrm{dI}}{\mathrm{I}}$ of experimental data, shown to visualize the area of interest for lineouts.

To track the structural dynamics, we analyzed the time dependent features of 2D dI/I plots. Figure 2.8a shows the time-dependent lineout of $\frac{dI}{I}$ along different features of $\frac{dI}{I}$ in Figure 2.8b. The lineouts are calculated by integrating over a certain s range, which is shown by the colored rectangles in Figure 2.8b, and plotted against the pump-probe delay in Figure 2.8a. It is seen that the feature at low s, which can be attributed to the electronic dynamics has an onset well before the onset of the features corresponding to the nuclear dynamics. This tells us that, immediately after photoexcitation, electron transitions to excited states.

However, structural evolution does not start with electronic transition. It takes some time to respond to the laser excitation. Also, the low s signal starts to decrease as the higher s signal increases, which tells us that the electronic deexcitation begins from the excited state with the onset of structural change. Each of the features is fitted by an error function of the following model:

$$f(t) = a \times \operatorname{erf}\left(- \frac{\frac{(t-b)}{c}}{\sqrt{2log2}} \times \sqrt{2} \right) \tag{2.10}$$

In equation (2.10), a defines the amplitude of f, b is the center, c defines the width of the error function. We fit the experimental lineout using equation (2.10) and obtain the parameters b and c. We indicate the center of the fitted error curve, b, as T0. We define T0 as the time of onset for structural change. The parameter c gives the rise time of the signal along different feature. Table 2.1 shows the rise time and T0 of different features obtained from the fitting.

Table 2-1: Rise time and time of onset of different features at experimental dI/I.

Feature	Rise Time	T0
0.6<s<1.1	105fs	0fs
1.06<s<1.72	140fs	300fs
2.21<s<2.82	270fs	360fs
4.85<s<5.8	570fs	210fs
6.7<s<7.6	310fs	420fs

Evidently, the features at higher s have $T0$ a few hundred femtoseconds later, and their rise time is also longer than the low s feature. We interpret that immediately after excitation, the wavepacket spends a few hundreds of femtoseconds in the excited state. At this excited state, the wavepacket does not undergo large structural change. When electrons decay to lower lying excited state, energy in the excited QD is dissipated along various degrees of freedom which causes large structural change. This interpretation is consistent with the slower pathway as reported by Borne and Cooper et al. [110] and shown in Figure 2.3. The slower pathway corresponds to the dynamics started from the state which has $3p_y$ (singlet 3) and $3p_z$ (singlet 4) Rydberg character, and dynamics persist in these states for longer time.

2.7.3 Time-resolved data analysis using simulation

In the experiment, we found a delayed onset in the nuclear dynamics. For getting a sense about temporal behavior in simulation, we analyzed all the simulated trajectories. It became evident that the majority of these trajectories exhibited a rapid onset of nuclear dynamics immediately following the laser excitation (at time zero). However, a subset of trajectories exhibited a substantial delay in the onset of a large change in nuclear dynamics. We aim to compare our experimental data with those trajectories and explain the dynamics based on the simulation. But before that, we will analyze the simulation based on their time-resolved signal.

All the simulated trajectories are classified by the end-product: QD and NB. Each group of trajectories is further subdivided into three groups based on their initial excitation to singlet 2, singlet 3, and singlet 4 states. From these six groups (3 subdivisions for each QD and NB products) we first selected trajectories that have delayed nuclear dynamics.

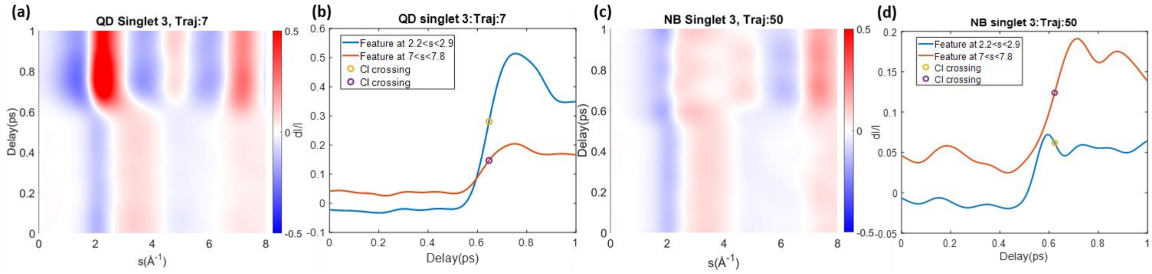

Figure 2.9: Illustration of trajectories that have delayed onset of nuclear dynamics. (a) 2D $\frac{\mathrm{dI}}{\mathrm{I}}$ of a trajectory that ends up to QD at the end of photodynamics and has initial excitation to a state that has singlet 3 character. (b) The lineout of $\frac{\mathrm{dI}}{\mathrm{I}}$ averaged at $2.2 < \mathrm{s} < 2.9\text{Å}^{-1}$ and $7 < \mathrm{s} < 7.8\text{Å}^{-1}$ is shown. Two circles on the lineouts represent the time for crossing the CI to relax to ground state. (c), (d) similar things done using a different trajectory as (a) and (b), respectively.

Figure 2.9a and 2.9c show the 2D dI/I plot for two such trajectories that have end-product QD and NB, respectively. Both trajectories have singlet 3 nature. We are seeing these two trajectories as the representative of all the trajectories that have delayed onset of nuclear dynamics. These two trajectories are chosen for a better illustration of delayed nuclear dynamics and its time-dependent behavior. The plots are convolved by a Gaussian with 100fs FWHM in time. In both plots, signals get stronger after a certain delay, as seen by the Increase in the amplitude of $\frac{dI}{I}$. The delay is evident in the lineouts shown in Figure 2.9b and Figure 2.9d. In the plots, the blue curve represents the time-dependent lineout of $\frac{dI}{I}$, obtained by integrating $\frac{dI}{I}$ at $s > 2.2\text{Å}^{-1}$ and $s < 2.9\text{Å}^{-1}$, and the red curve is taken by taking an average of $\frac{dI}{I}$ at $s > 7\text{Å}^{-1}$ and $s < 7.8\text{Å}^{-1}$. Both lineouts show that the signal has onset after about 500fs. After photo excitation, the nuclear wave packet moves along the PES. It takes a certain amount of time to reach the conical intersection (CI) and relax to the lower state through the CI. The circles on the lineouts in Figure 2.9b and 2.9d represent the time at which the excited QD crosses the conical intersection (CI). From these two plots, it seems that the large structural change is correlated to the time when the nuclear wave packet transfers the CI.

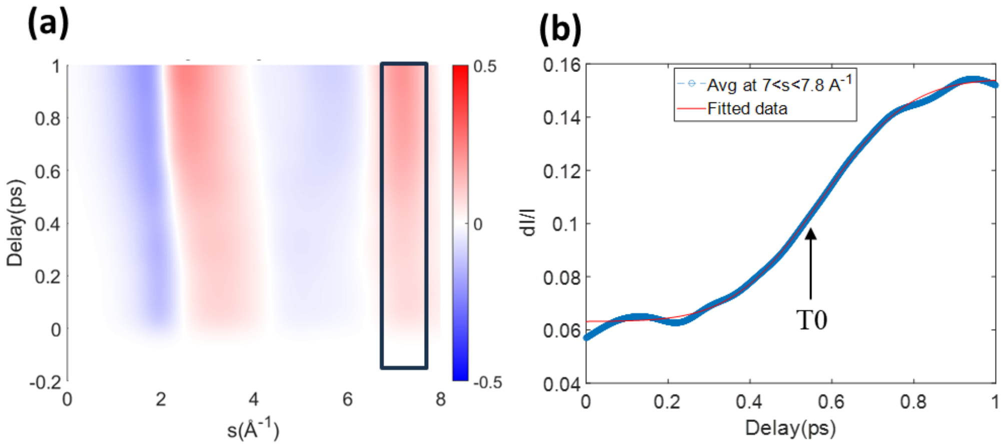

Figure 2.10: Simulated $\frac{dI}{I}$ and its time-dependent lineout. (a) 2D $\frac{dI}{I}$ averaged over all trajectories that result NB after photoreaction and have delayed nuclear dynamics. The rectangle shows area of interest for integration. (b) Time-dependent lineout is shown by the blue curve, and it's fitting by the error function is shown by red curve. In equation (2.10), the coefficient c evaluates the time of onset, which is labelled by T0.

We will now see if the time at which the excited wavepacket crosses the CI is associated with the time when large structural change happens. We investigated the correlation of CI transfer time with T0 (Time of onset of the structural change), for all selected trajectories, irrespective of their time of onset of nuclear dynamics. We are seeing Figure 2.10 to illustrate how we selected the trajectories to see the correlation of T0 and CI transfer time. Figure 2.10a shows 2D $\frac{dI}{I}$ calculated from the averaged trajectories that yields NB and exhibits a delayed onset in nuclear dynamics. Figure 2.10b shows the lineout taken by averaging $\frac{dI}{I}$ at the highlighted area in Figure 2.10a, and it's fitting by equation (2.10).

Here, I will describe how we selected trajectories. For all the available trajectories, we first calculate the lineout of $\frac{dI}{I}$ averaged at $s > 7\text{Å}^{-1}$ to $s < 7.8\text{Å}^{-1}$, as seen by the rectangle in Figure 2.10a. Then we fit the $\frac{dI}{I}$ lineout using equation (2.10), as shown in Figure 2.10b. The blue line is the time-dependent lineout of $\frac{dI}{I}$ and the red-curve is the fitting by equation (2.10). We only kept those trajectories that correspond to a good fit of $\frac{dI}{I}$ lineout by equation (2.10). We rationalized the goodness of fitting by seeing the parameter c and regression constant. c gives some unphysical value for the case of inappropriate fitting. The fitting parameter, b gives the time of onset of nuclear dynamics, T0.

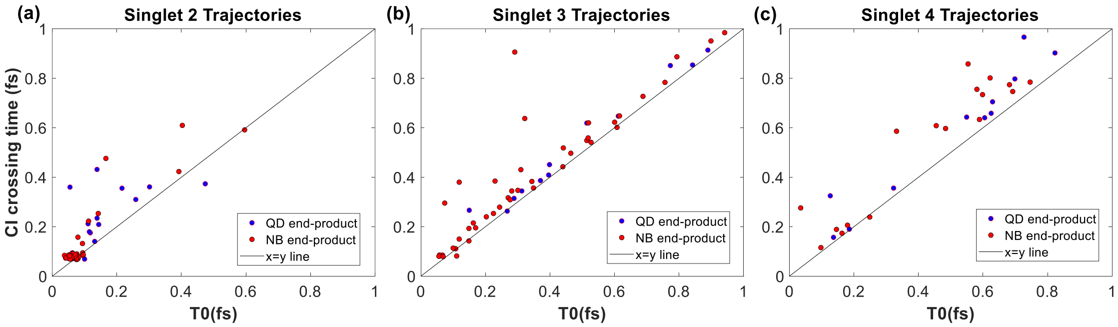

Figure 2.11: Relations of CI transfer time as a function of time of structural change. Each plot shows the time of onset of structural change in the horizontal axis, and the time at which the trajectory crosses the CI in the vertical axis. Blue dots represent the times for trajectories that result in hot QD and red dots represent the times for the trajectories that result in hot NB. The diagonal line is drawn to show the reference to demonstrate the linearity in their relation. Different singlet states are shown in plot (a), (b) and (c).

Figure 2.11 shows the CI crossing time as a function of the time of onset of nuclear dynamics (T0) of different trajectories. In each plot the blue dots represent the trajectories that ended up producing QD, and the red dots represent the trajectories that that ended up producing NB at the end of photo dynamics. The black line in each plot shows the $y = x$

line as a reference. Figure 2.11a shows this dependence for the Singlet 2 trajectories. From this plot we can see that trajectories which have faster onset are clustered about the $y = x$ line. For the other trajectories with delayed onset have CI crossing time increases with an increase with T0. This behavior is more evident in Figure 2.11b and Figure 2.11c, which represent the trajectories of singlet 3 and singlet 4 states, respectively. Here, the dots are aligned mostly about the $y = x$ reference line and show a linear increase in CI crossing time with respect to structural change. This behavior establishes that excited state QD undergoes some structural change while it crosses the CI to relax to the ground state.

From Figure 2.11, we can assert that the excited state QD relaxes to ground state with a large structural change. As described by the simulation[110], Figure 2.11a accounts for the faster channel of relaxation, that's why it is obvious that most of the trajectories have a rapid onset of nuclear dynamics. However, for the slower channels (singlet 3 and singlet 4), there is a significant number of delayed trajectories, and all of these trajectories have a good correlation between CI transfer time and T0. In analogy to these trajectories, we infer that in experiment, after photoexcitation of the ground state QD, the excited QD moves along PES of higher excited state. Large structural change is not possible in this higher excited state because of the presence of a barrier[109]. When it falls to the lower excited state by internal conversion, the excess energy is dissipated along different degrees of freedom in QD molecule. This energy distribution triggers a large structural change which brings the excited state QD to the CI and subsequently QD relaxes to ground state. The onset of nuclear dynamics in experiments indicates the instance when the excited state QD reaches the CI point. Moreover, the delayed nuclear dynamics in experiment is indeed resembling the slower relaxation pathway to ground state as seen in the simulation[110].

2.7.4 End-products determination

In this section, we will outline our efforts to determine the relative product ratio at the end of the photodynamics process. While most of the previous studies done on the photochemistry of QD could not structurally resolve the relative yield of end-products, the structure sensitivity of UED has the capacity to find the structure of the end products and their relative yield[52]. The work of Borne and Cooper et al. predicted that the photoreaction of QD by 200 nm photon yields QD and NB at a ratio of 2 to 3. However, they could not validate the prediction using XUV photoelectron spectroscopy because of its structural insensitivity[110].

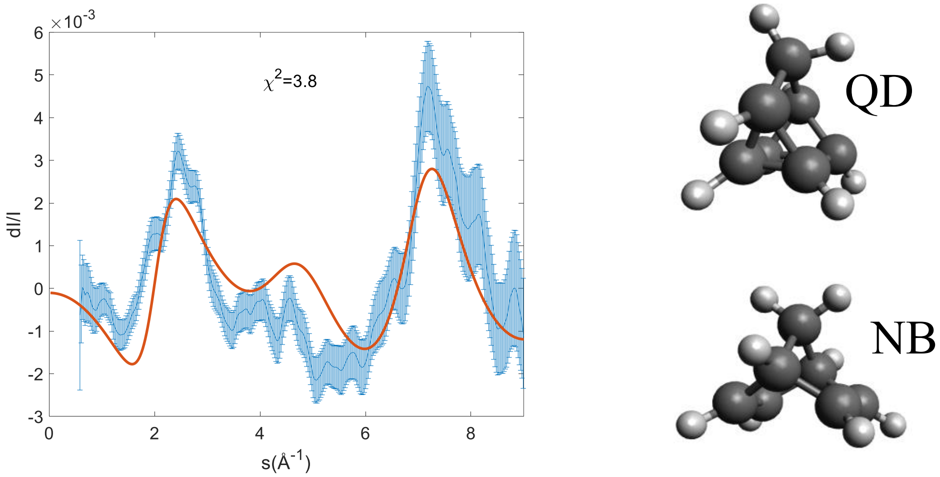

Figure 2.12: Fitting the experimental data using hot QD and hot NB end products. Experimental and simulated $\frac{\mathrm{dI}}{\mathrm{I}}$ are averaged at 700fs-1000fs. The fitting yields 96% hot QD and 4% NB. The structure of QD and NB is also shown.

In Figure 2.12, we fit the experimental data by a linear combination of simulated trajectories that yield QD, and NB. Blue curve represents the experimental $\frac{dI}{I}$ averaged at 700fs-1000fs and it is denoted by $\frac{dI^{expt}}{I}$. In simulation, we use only those trajectories that have delayed onset of nuclear dynamics. Trajectoies that yield QD at the end of photoreaction are combined. From this combined trajectories, we calculated the dI/I and averaged them at 700fs-1000fs which gives $\frac{dI^{QD}}{I}$. Similar process is followed for the trajectories that yield NB as end-product, have delayed onset of nucelar dyanamics, and we obtain $\frac{dI^{NB}}{I}$. $\frac{dI^{QD}}{I}$ and $\frac{dI^{NB}}{I}$ form the two bases to fit $\frac{dI^{expt}}{I}$. The fitting follows the equation:

$$\frac{dI^{simu}}{I}(s) = \left[a \times \sum_{t=700fs}^{t=1000ds} \frac{dI^{QD}}{I}(s,t) + (1-a) \times \sum_{t=700fs}^{t=1000ds} \frac{dI^{NB}}{I}(s,t)\right] \tag{2.11}$$

Here, the parameter a determines the relative percentage of QD and NB in the end product. We used reduced χ^2 to find the best fit between the experiment and the simulalted lineouts.

$$\chi^2 = \frac{1}{N-k} \sum_{s=1.6}^{9} \left(\frac{c \times \frac{dI^{simu}}{I}(s) - \frac{dI^{expt}}{I}(s)}{\sigma(s)} \right)^2; \tag{2.12}$$

In equation (2.12), c determines the relative scaling between experiment and simulation expressed by equation (2.11), and this is called the excitation factor. N is the total number of elements in $\frac{dI^{simu}}{I}$ or $\frac{dI^{expt}}{I}$, and k represents the number of fitting parameters. We used the particle swarm optimization algorithm to get the minimum of χ^2 [112], [113]. The value of the minimum reduced χ^2 for this fitting was 3.8. The relative product ratio for QD and NB is 96%: 4%. Although the major peaks in the fitted simulation at $s = \sim 2.1\text{Å}^{-1}$ and at $s = \sim 7.2\text{Å}^{-1}$ appears at the same s position of the experimental lineout, there is a signaficant mismatch between the two lineouts. Notably, the simulation misses the experimental lineout at $s = \sim 1.6\text{Å}^{-1}$ and in the range $s = 4 - 5.8\text{Å}^{-1}$. This drives us to think if any other channel is involved in the photodynamics other than only the isomerization from QD→ NB.

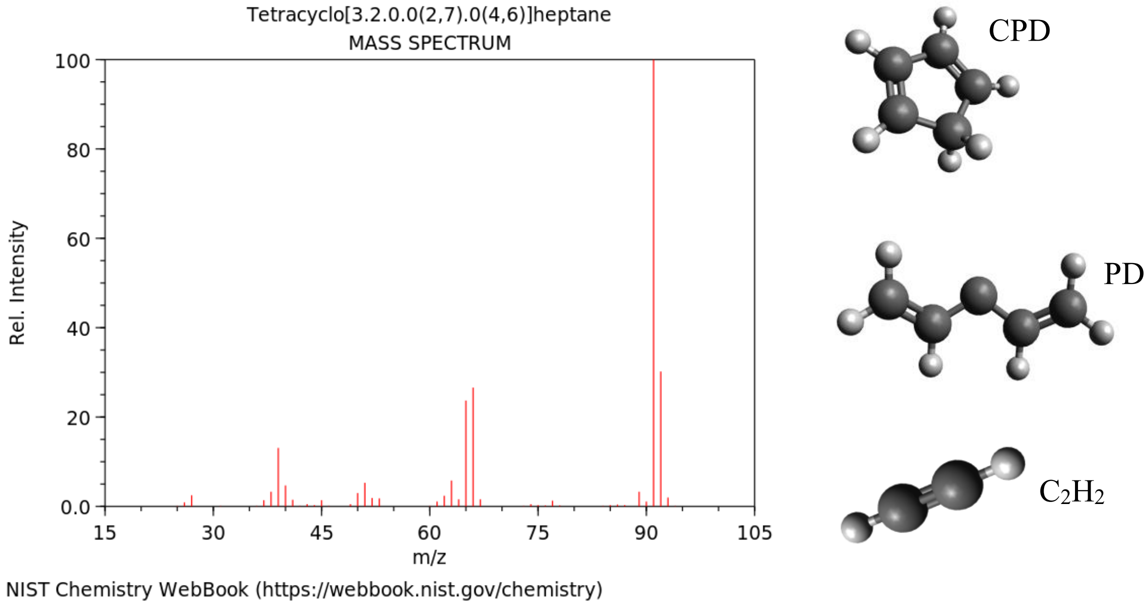

NIST Chemistry WebBook (https://webbook.nist.gov/chemistry)

Figure 2.13: Mass spectrum of Quadricyclane adapted from NIST website. We looked for possible fragments due to dissociation of QD in the photoreaction, and optimized cyclopentadiene (CPD), pentadiene (PD), and acetylene (C_2H_2).

Since the fitting in Figure 2.12 is not praiseworthy, we consider if other channel like dissociaton is involved in the dynamics. For checking this possibility we will now fit the experimental data, $\frac{dI^{expt}}{I}$, by $\frac{dI^{QD}}{I}$,$\frac{dI^{NB}}{I}$ and $\frac{dI}{I}$ calculated for fragments. Figure 2.13 shows the mass spectrum data of quadricyclane generated by electron ionization. We use the mass spectrum to get idea about possible fragments of QD. QD (C_7H_8) has a molecular mass of 92 gram per mole. In the mass spectrum, the most prominent peaks can be seen at the mass-to-charge ratio (m/z) of 91-92, which is the parent QD (m/z=92) or a hydrogen atom dissociated QD (m/z=91). The second prominent peak is at m/z=66, that corresponds to C_5H_6. The fragmentation of C_7H_8 to C_5H_6 aslo produce C_2H_2 (acetylene). We optimized two possible structures of C_5H_6, cyclopentadiene (CPD) and pentadiene (PD), and acetylene. The optimization is done using B3LYP def2-SV(P) basis function. We then calculated the diffraction signals, I^{CPD}, I^{PD} and $I^{C_2H_2}$, for the optimized fragment structures. Subsequently, we calculated the difference diffraction signal using equation (2.6) as follows:

$$\frac{dI^{CPD+C_2H_2}}{I} = \frac{I^{CPD}+I^{C_2H_2}-I^{QD}}{I^{QD}}, \tag{2.13}$$

$$\frac{dI^{PD+C_2H_2}}{I} = \frac{I^{PD}+I^{C_2H_2}-I^{QD}}{I^{QD}}. \tag{2.14}$$

Where, I^{QD} is the scattering intensity of the ground state QD. We modified equation (2.11) for fitting the experimental data, $\frac{dI^{expt}}{I}$, by four bases, namely, $\frac{dI^{QD}}{I}, \frac{dI^{NB}}{I}, \frac{dI^{CPD+C_2H_2}}{I}$ and $\frac{dI^{PD+C_2H_2}}{I}$. For this case, we can write equation (2.11) as follows:

$$\frac{dI^{simu}}{I}(s) = \frac{1}{c_1+c_2+c_3+c_4}\left[c_1 \times \sum_{t=700fs}^{t=1000ds} \frac{dI^{QD}}{I}(s,t) + c_2 \times \sum_{t=700fs}^{t=1000ds} \frac{dI^{NB}}{I}(s,t) + c_3 \times \frac{dI^{(CPD+\mathrm{C}_2H_2)}}{I} + c_4 \times \frac{dI^{(PD+\mathrm{C}_2H_2)}}{I}\right] \tag{2.15}$$

Using equation (2.12) and (2.15), we obtained the minimum χ^2 for the best fitting using the same optimization algorithm.

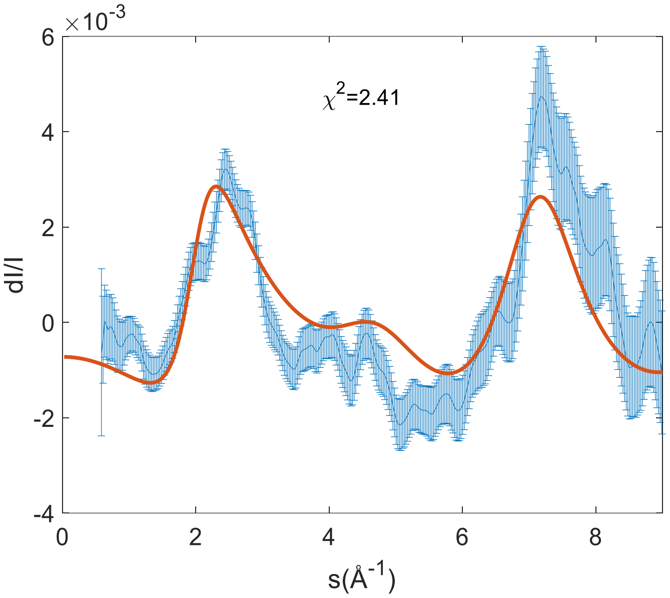

Figure 2.14: Fitting the experimental data by adding dissociation products. In addition to the hot QD and hot NB, $\mathrm{dI/I}$ for CPD and PD is calculated, and all four channels are used to fit the experimental data. The reduced χ^2 improved for this fitting compared to the fitting in Figure (2.12).

Figure 2.14 shows the fitting of the experimental data for four different end-products outlined above. The reduced χ^2 improved to 2.41 compared to the case of two products. We got a product ratio for QD, NB, (CPD+C_2H_2), and (PD+ C_2H_2) is 56%:31%:13%:0. Qualitatively, the fitting improves at $s = \sim 1.6\text{Å}^{-1}$. We got an excitation percentage of 1.2% from this fitting.

Apart from the fragmentation, the fitting yields QD and NB at a ratio of 65:35, which is opposite of the theoretical prediction, where majority of the end product was NB. Looking at the χ^2 and qualitative fitting in Figure 2.13, we assert that the fitting is not praiseworthy in an extent to make a solid conclusion in determining the end-product and their ratio. Also, for fragments, we only used single optimized structure. The structure does not convey any information about the dynamics after they are formed. Simulation of dissociation channel might lead us towards greater agreement of the data with simulations.

2.8 Summary

We observed scattering signals corresponding to electronic and nuclear dynamics in the time-dependent study of the experimental data. We validated the electronic signal in the experiment by performing the ab-initio scattering calculation for the electronic excitation of a single structure of QD. Performing the ab-initio scattering calculation on the simulated trajectories could give us a comprehensive view of electronic dynamics.

We followed a delayed onset of the nuclear dynamics in the experimental data. However, simulation has a rapid onset of nuclear dynamics after laser excitation which inhibits the agreement between experiment and simulation. We were able to make a subset of trajectories which shows similar delayed onset of nuclear dynamics as of the experiment. By analyzing the simulated trajectories, we found that the time at which the nuclear wavepackets cross the CI is directly correlated to the time of large structural change. We interpret that the reason for delayed onset is due to spending QD at higher PES for a period of time after laser excitation. When the QD falls in the lower lying excited state, the excess energy dissipates along various degrees of freedom which causes a large structural change of the molecule. This structural change brings the molecule to the CI through which it relaxes to the ground state. Since the onset of structural change brings the molecule to the conical intersection, and structural change continues after crossing the CI, we think the end product forms after crossing the conical intersection and in the ground state.

We tried to fit the experimental data by simulations of different end products. The improvement of the fitting by involving the dissociation product indicates that in addition to the isomerization, dissociation is involved in the dynamics. However, the dissociation channel only includes optimized single structures. Simulation of dynamics structure after dissociation might improve the fitting. The analysis is still ongoing.

Chapter 3

UV dynamics of cis stilbene Studied by Ultrafast Electron Diffraction

3.1 Introduction

Stilbene is a prototypical molecule used for studying photoisomerization and photocyclization. In the ground state, stilbene can exist in two conformers: cis-stilbene (CS) and trans-stilbene (TS). Extensive studies have been done on TS as the lifetime of the first excited state of TS in the gas phase is on the order of 10-100ps[114]. The barrier height to move to the conical intersection (CI) from the Frank-Condon point in excited TS was reported to be 1200cm^{-1} or 0.15 eV[115][116][117][118]. On the other hand, when excited from the CS, there is almost no barrier experienced, which results in an excited state lifetime of <500fs [119][120][121]. From the study of CS in the solution phase, the barrier height measured around 400cm^{-1} or 0.05eV[122][123]. With the advent of femtosecond probing tools, interest grew in CS as it undergoes both isomerization and cyclization reactions due to 1-photon excitation. The photoisomerization process yields CS and TS due to the continued rotation of phenyl ring around the central C-C bond. Photocyclization yields mostly CS and the ring-closed product of 4,4-dihydrophenanthrene (DHP) due to electronic rearrangement[124][125].

Numerous studies being done on CS as well, both experimentally and theoretically[126][127][128][125][129][130][131][132][133][134][135][136][137][138][139][140][141] to elucidate the S_1 dynamics. However, only a few studies were done to explore the higher excited state of both cis-stilbene and trans stilbene. Bao et el. employed time resolved photoelectron spectroscopy (TRPES) and mass spectroscopy(MS) to study the highly excited state of CS[128]. They pumped the ground state CS by 6eV photon and probed it by time-delayed 3eV photon. They observed that after absorbing the pump photon, CS is excited to 7^1B state. From this state, CS stilbene undergoes a decay process to reach the 3^1B state within 167 femtoseconds. The ring closing reaction of CS to DHP occurs in this state. The decay of 3^1B state to 1^1B (S_1) occurs in 395fs. From 1^1B state CS undergoes to ground state via a conical intersection by forming only CS and DHP. They did not see isomerization of CS to TS in this study. They also shed light on the ionization dynamics of CS. From 7^1B state, excited CS can absorb one probe photon to ionize to form CS^+. They postulated that CS^+ can undergo to form ring closed DHP^+. However, they could not experimentally verify the reaction from CS^+ to DHP^+ because neither TRPES nor MS can distinguish the isomers. If CS^+ absorbs another 3eV photon, it can form ring closed hydrophenanthrene cation (HPT^+) via a dissociation of its hydrogen and ring closing reaction. On the other hand, If DHP^+ is formed due to isomerization of CS^+, it can form HPT^+ and phenanthrene cation (PT^+) by absorbing another 3eV probe photon.

In a different study, Bao et al. used trans-stilbene (TS) to excite them at S_5 state using a 6eV pump photon and they probed the dynamics using 3eV probe photon[142]. On the S_5 state, they observed an antisymmetric torsional oscillation. This oscillation happens in the phenyl rings about the C-C single bond in trans stilbene. The frequency of oscillation was determined to be 0.2THz. They concluded that excitation to higher excited state exhibits different dynamics than excited to lower states.

Given the comprehensive understanding of the dynamics in S_1 states and the distinct dynamics in higher excited states, this study aims to explore the ionization dynamics of

CS. Previous research on CS and TS in higher excited states has been limited, and no structure-sensitive probe has been used to investigate CS in its ionized state. To address this gap, the study utilizes the spatiotemporal resolution of MeV-UED to capture the previously unexplored ionic dynamics of CS. Although UED is commonly used for structure-sensitive one-photon dynamics studies[143][53][144][145][74], it has not yet been employed to investigate ionization dynamics. Xiong et al. implemented UED to determine the end product due to isomerization and fragmentation of Toluene as a result of laser induced ionization. However, they did not probe any dynamics on ion-state. The potential of UED in probing molecular dynamics on a femtosecond timescale, with its structure sensitivity, makes it a crucial tool for unraveling structural evolution and underlying scientific phenomena.

In this study, the research delves into the dynamics of stilbene after 2-photon excitation. By comparing experimental results at two different laser pulse intensities, the study distinguishes between the contributions of the 1-photon channel (previously investigated) and the 2-photon channel leading to ionization. Using a 267nm UV pulse with a 70-fs pulse duration for excitation and UED for structural dynamics probing, the research identifies structural changes in the stilbene cation and pinpoints the primary vibrational mode, with excellent agreement between experimental findings and theoretical predictions.

3.2 Methodologies

In this section, I will explore a range of methodologies that we use during the data acquisition and data analysis steps. Specifically, I will provide a brief overview of the experimental procedures for conducting the experiment, outlining various experimental parameters and essential steps in data processing and analysis. These steps includes image cleaning, describing zero-fitting method for static data analysis, detector pixel to s calibration, characterizing instrumental response time, uncertainty determination, a brief introduction to the simulation used analyzing the experimental data, determining the percentage of dynamics by fitting the experimental data, identifying ionization, transforming the simulated ΔsM to ΔPDF, and Fourier transform of the time-dependent data from both experiment and simulation.

3.2.1 Experimental methodology

The experiment was carried out at the MeV-UED facility at the SLAC National Accelerator Lab [26] in March 2020. I was present during the experiment and actively operated the experimental setup to take data. The description of the setup is presented in section 2.5.1. In brief, a Ti: Sapphire laser system generates 800 nm pulses with a pulse duration of 70 fs and a repetition rate of 180 Hz. About 3% of the total output is frequency tripled to 267 nm and directed to the 1.6-cell s-band photocathode RF gun, where electrons are produced in the photoemission process. Electrons are then accelerated to 3.7 MeV and directed into the interaction zone within a sample chamber designed for gas-phase diffraction experiments via a holey mirror.

Figure 3.1 shows the normalized optical absorption plot of cis stilbene. The maximum absorption happens at 276nm. From the plot it is found that at 267nm pump wavelength about 95% absorption happens. To pump the cis stilbene at 267nm, another part of the laser beam is also frequency tripled, directed, and focused to the interaction point with a spot size of 200 μm full-width half-maximum (FWHM). We carried out experiments pulse energies of 80 μJ and 130μJ, resulting in fluences fluence in the interaction point of 170mJ/cm^2 and 280mJ/cm^2, respectively.

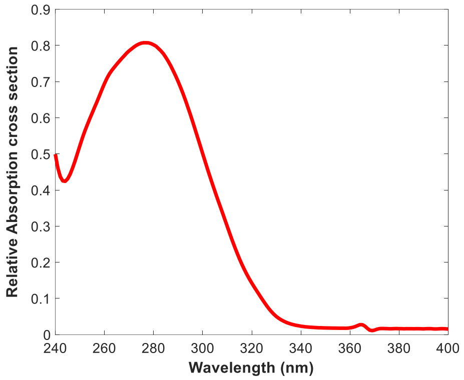

Figure 3.1: Absorption cross section of cis stilbene. The plot is created from the online tool found here[2] and the references[146], [147]. The spectrum is originally published in Ref[116].

The probe electron beam and pump laser beam traverse the sample almost collinearly to minimize temporal blurring due to velocity mismatch. An in-vacuum bubbler containing 20 g cis-stilbene was heated to a temperature of 168°C. The whole gas delivery line was also heated at the same temperature to rule out any possibility of clogging the gas line by condensation of the CS vapor when it came in touch with the colder surface of the gas line.

A stable gas delivery condition was attained by backing the stilbene vapor with 1000 torr of He. The diffracted electrons were captured in a detection system consisting of a combination of a phosphor screen and an electron-multiplying charge-coupled device. We fitted the fastest feature in the signal with an error function and found a 145fs instrument response function (IRF) time in our setup. The instrument response time includes the pulse duration of the laser and electrons and their relative arrival time jitter.

---

[2] https://omlc.org/spectra/PhotochemCAD/html/163.html

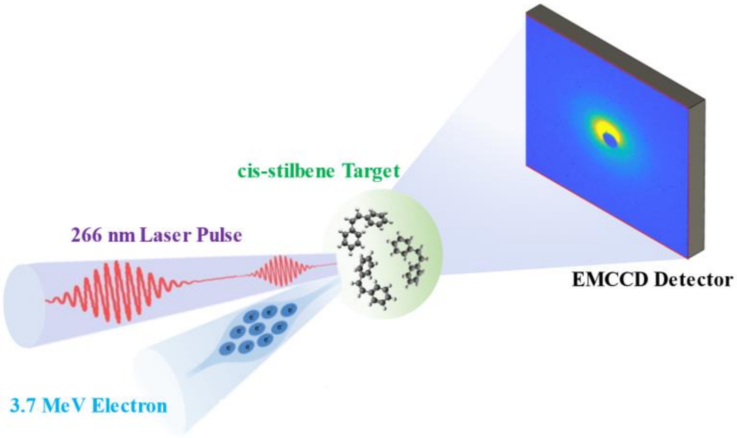

Figure 3.2: Schematic presentation of laser-electron interaction with CS target. A 267nm UV pulse excites the CS molecules. The excited state dynamics are then probed by using a 3.7 MeV pulsed electron beam at variable delay time, which is scattered by the target molecule. The scattered electrons are recorded on a phosphor screen coupled with an electron multiplying charged coupled device detector. These images are cleaned and analyzed to reveal the molecular dynamics.

Figure 3.2 shows the schematic of pump-probe interaction with the gas sample. The interaction is recorded by a phosphor screen which is coupled to an EMCCD camera. For 170 mJ/cm^2 pump fluence, we took 33 images at each delay point, with 20s exposure time of each image. We took a total of 6 hours data for fluence of 170 mJ/cm^2. On the other hand, for 280 mJ/cm^2 fluence, we took total of 4 hours data with 22 images at each delay point, each with 20s exposure time. For data set with each pump fluence, we took data at 28 delay points. The time delays lie from -1ps to 10ps about the time zero, with 66fs intervals for early time (-0.5ps to 1ps) delays and 1 ps-3 ps intervals for longer time delays. The 2D raw diffraction images are processed to remove any unwanted noise or artifact using the procedure discussed in section 3.2.2. The clean diffraction images are azimuthally averaged to get the total scattering intensity in one dimension.

3.2.2 Image cleaning

In this section, I will provide a detailed explanation of our procedure for cleaning and processing experimental diffraction images. Our goal is to eliminate any unwanted artifacts and noise that may be present in these images, ensuring that the data we analyze and interpret is as accurate and reliable as possible.

- **Removing the Background:** We start the image cleaning by removing the background. 45 background images were taken by turning off the electron beam with 20s exposure time of each image. We combine all the background images and apply a threshold to remove all hot-pixel and saturated pixels. We also apply a median filter to remove further noise from the background image. The processed background image is subtracted from each of the diffraction images.
- **Ellipticity Correction:** We observed that the diffraction image on the detector was not perfectly circular. This likely occurred because the image from the phosphor screen onto the Andor camera was distorted, resulting in a slightly elliptical diffraction pattern. Before collecting data with gas-phase stilbene, we acquired a few diffraction images using a solid-phase sample, bismuth, in order to establish the experimental time zero. The scattering of electrons by bismuth generated diffraction rings on the detector. We utilize these diffraction rings to correct the elliptical distortion by ensuring that the distances across various points on the ring were of equal size, using an ellipticity correction algorithm. Subsequently, we use the output from the algorithm to mitigate the effect of ellipticity in the gas phase diffraction images.

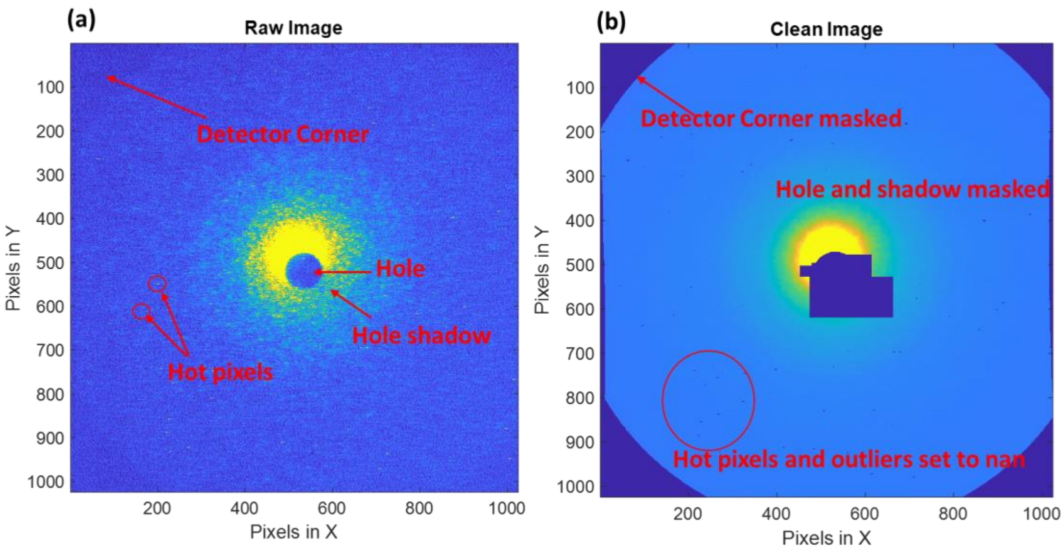

Figure 3.3: Diffraction image before and after cleaning. The image in (a) shows a few possible artifacts. (b) Diffraction image after cleaning.

- **Removing hot pixels:** The diffraction pattern obtained from the experiment typically contains "hot pixels," which may arise from X-ray hits, saturated pixels, or permanently damaged areas. To address this issue, we calculate the mean value and standard deviation for each pixel by averaging all images taken at a specific delay point. Subsequently, we establish a threshold that is three standard deviation higher than the mean value for each pixel. Any pixel exceeding this threshold is then marked as "not a number (NAN).
- **Masking the artifacts:** We mask the central hole on the phosphor screen, the shadow due to the hole (as seen in Figure 3.3a) and any remaining artifacts that the methods mentioned earlier couldn't eliminate. We also mask any electron beam leakage by setting their values as NAN. This way, we ensure that there are no alternation in the azimuthal average.

- **Removing CCD induced artifacts:** The Andor camera chip has 1024×1024 pixels array and possessing a square shape. The phosphor screen has a circular geometry. Because of the circular geometry of the phosphor screen, the corner of the camera chip does not contain any scattering signal, seen in Figure 3.3a. We take the mean at the corners of the rectangular shape detector, where phosphor screen is not imaged, and subtract the value from the whole diffraction image to account for the detector baseline. Due to the prolonged usage, camera chip gets warmed, a certain elevation in the count can result. This count can be removed by following this step. After getting the average from the corner, we masked the corner by putting the values as NAN.
- **Removing radial outlier:** We average all the images of each delay point and determine the diffraction center at each delay point using a suitable diffraction center finding algorithm. Subsequently, we take an average of the diffraction centers of all the delay points. For each diffraction image, we determine the azimuthal mean and standard deviation about that center. We remove any pixel, located on a specific radial distance from the center, that has value above or below the three standard deviations from the mean on that radial distance. In this way, we get circularly symmetric intensity with respect to the diffraction center.
- **Applying Median Filter:** To address any residual "salt and pepper" noise, we employ a median filter with a 7x7 window size. It's important to note that when a pixel within this window contains a NAN value, the median filter operation turns all the pixels within the window into NAN, which could result in the loss of useful data. To avoid this, prior to applying the median filter, we replace any NAN values

within a pixel with the azimuthal average around the diffraction center in that specific pixel location. After the median filter is applied, we restore the NAN values to their original locations, ensuring that essential data is preserved while effectively reducing "salt and pepper" noise in our processed images.

- **Calculating fine diffraction center:** We take the average of all the images at each delay point. We determine the diffraction center from average diffraction image at each delay stage. We take the mean of the centers of all delay stages and use this mean diffraction center for further analysis, such as taking the azimuthal average to convert the 2D diffraction image to the 1D azimuthal average.
- **Correcting offset and tilt:** We calculate the azimuthal average of the diffraction pattern and hence convert the 2D diffraction matrix into a 1D vector. When calculating dI/I or dsM in s-space for each time-delay, we find the $\frac{dI}{I}$ or dsM has some tilt about the baseline in s space. We correct any tilt by fitting a power function of the form $y = as^b + c$. After fitting, we recheck the fitted $\frac{dI}{I}$ or dsM if the tilting and offset are removed.
- **Smoothing the data:** We remove high frequency noise of the data by using a moving mean of a window size of 0.25Å^{-1} along s. To smooth the data along the time axis, we applied convolution by a Gaussian of 100fs FWHM.

3.2.3 Zero-fitting method

The modified scattering intensity (sM) from the static data is calculated using Zero-fitting method. In this method, sM is calculated using theoretical input, and therefore, it is not used for time dependent analysis to avoid any bias form the theory. The zero-fitting method works in the following way. First, we calculate the theoretical sM (TsM) using the equation (2.4). I_{mol} and I_{at} are calculated using the independent atom model discussed in section (1.5.4). We use an optimized ground state structure for calculating I_{mol} and I_{at}. The positions of s where TsM has zero value are found. Let's call these s positions as s_0. At $s_0, I_{mol} = 0,$ since $s\frac{I_{mol}}{I_{at}} = 0.$ At these s_0 positions, the experimental total scattering (I_{expt}), which is calculated by azimuthally averaging the diffraction image, are extracted. At s_0 positions of I_{expt}, $I_{mol}^{expt\ at\ s_0}$ is considered zero, consistently with theory. Hence, I_{expt} consists only the sum of atomic and background scattering, I_{BC}, at the s_0 postioms. Then I_{BC} vs s_0 is plotted and the curve is fitted by a piecewise exponential function of the form, $B(s) = e^{a+bs^c}$. $B(s)$ is then subtracted from I_{expt}, that gives the experimental scattering signal free of atomic and background scattering, which is the molecular scattering intensity (I_{mol}^{expt}) found from the experimental data. Using I_{mol}^{expt}, and theoretically calculated atomic scattering, experimental sM is calculated using the equation (2.4).

3.2.4 Pixel-to-s calibration

The detector has 1024×1024 pixel array. For transferring the pixel value to the momentum transfer vector, s, we fit the experimental sM curve to the theoretical sM (TsM) curve for different pixel-to-s calibration value and look for the best fit. The TsM is found by calculating the total scattering signal from the structures of cis stilbene sampled by harmonic Wigner distribution at 0°C. These cis-stilbene structures were generated by Dr. Hayley Weir, a former graduate student at Standford University. The calibration value during the data acquisition with 80μJ pump energy is 0.0250; however, the calibration value during the data acquisition with 130μJ pump is 0.0243.

3.2.5 Instrument response time

This section describes how we experimentally calculate the instrumental response function (IRF) time of the UED set up during the experiment and experimentally determine the time zero. We calculate the rise time of different features by fitting the integrated signal at a certain s range using the following equation $y = a \times \mathrm{erf}\left(-\frac{(x-b)}{\frac{c}{\sqrt{2log2}}} \times \sqrt{2}\right) + d$, where, a is the amplitude, b is the center, c is the width of and d accounts any offset of the fitted curve. We found the experimental feature at $0.55 < s < 1.1\text{Å}^{-1}$gives the fastest rise time of 145fs. The 145fs represents the convolution of the temporal resolution of the experimental system with the response time of the stilbene to the laser excitation[148]. This 145fs thus can be said to be the upper limit of the IRF. We also put the experimental time zero based on this feature. The parameter b in the fitting equation gives us the time of onset of the feature. We put the time zero for each data set following the parameter b.

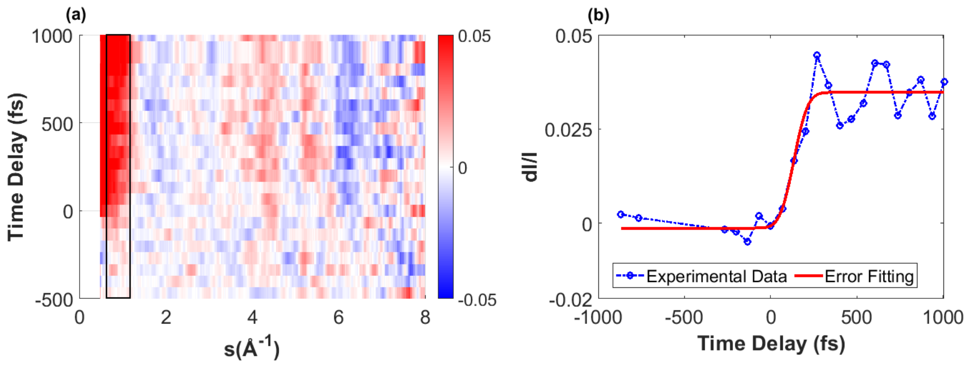

Figure 3.4: Measurement of temporal resolution. The integrated dI/I at $0.55 < s < 1.1\text{Å}^{-1}$ in (a) is fitted by an error function. (b) The fitting of the integrated dI/I by the error function. The FWHM of the associated Gaussian obtained 145fs. For temporal resolution measurements, we did not apply Gaussian convolution along the time axis.

3.2.6 Uncertainty determination

We used the standard bootstrap process to find the uncertainty in our data. To illustrate the process of bootstrapping, let's say we have 1 dataset consisting of n number of images at each delay point. We also consider we have m delay points. So, our initial data set has $n \times m$ array size. We randomly resample n images with replacement for 100 times, and for all m delay points. This gives us 100 datasets of each delay point, where each data set contains n number of images. The bootstrap data set has now dimension $100 \times n \times m$. We applied the data cleanup process to each of the 100 dataset and analyzed them individually. We calculate the $\frac{dI}{I}$ for each dataset. The mean and error bar are determined by calculating the average and standard deviation over the 100 bootstrap datasets.

3.2.7 One-photon excitation and two-photon excitation simulations

Both one-photon and two-photon excitation simulations are done by Dr. Hayley Weir, former graduate student in Professor Todd Martinez's group at the Stanford University. The Nonadiabatic dynamics simulations for one-photon excitation dynamics were performed with Ab-initio Multiple Spawning (AIMS) on a CASSCF / 6-31G* potential energy surface. Details about the simulation can be found in Ref[134]. Briefly, 100 trajectories were initiated from 100 initial geometries of cis stilbene sampled using 0K harmonic Wigner distributions. The trajectories are promoted to the S_1 state due to the absorption of a 267nm photon and then propagated for 2 ps. The simulation's final outcome reveals a ratio of 44:52:4 for CS: TS: DHP in the end product. For the case of two-photon excitation, Dr. Weir used molecular dynamics (MD) simulation utilizing unrestricted B3LYP / 631G* basis function. For this case, the simulation started from 20 initial geometries sampled using 0K harmonic Wigner distributions. The trajectories propagate for a time of about

12ps in the ionized ground state. We are given the time dependent structures of each trajectory. Each structure is separated from another by 0.5fs. I calculated the total scatterings intensity from these trajectories using IAM.

3.2.8 Determination of the percentage of dynamics and excitation factor

We compare our experimental data with the simulation to find the ratio of dynamic happening along one photon channel and two-photon channels. The excitation factor greatly depends on whether one photon channel or two-photon channel dominates. We use a three-parameter fitting routine to fit the simulation to our experimental data by minimizing the reduced χ^2 value. For this case, we use:

$$\frac{dI^{simu}}{I}(s) = \frac{c_1}{c_1+c_2} \times \frac{dI^{AIMS}}{I}(s) + \frac{c_2}{c_1+c_2} \times \frac{dI^{MD}}{I}(s); \tag{3.1}$$

Here, $\frac{dI^{AIMS}}{I}$ is the time-averaged AIMS simulation for one photon dynamics, and $\frac{dI^{MD}}{I}$ is the time-averaged MD simulation for ionization. We then calculate the reduced χ^2 following the equation:

$$\chi^2 = \frac{1}{N-k}\sum_{s=2}^{7}\left(\frac{c_3 \times \frac{dI^{simu}}{I}(s) - \frac{dI^{expt}}{I}(s)}{\sigma(s)}\right)^2; \tag{3.2}$$

Here, $\sigma(s)$ is the standard deviation calculated from the bootstrap data. We use particle-swarm optimization routine[112], [113], [149], which optimized the parameters $c_1, c_2,$ and c_3 to minimize the χ^2. The percentage of the dynamics is calculated using parameters c_1 and c_2, where,

$$\text{\% of 1-photon excitation} = \frac{c_1}{c_1+c_2} \times 100\%,$$

and $\quad$ % of 2-photon excitation=$\frac{c_2}{c_1+c_2} \times 100\%$.

c_3 from the fitting gives us the excitation percentage of the molecule due to laser interaction.

3.2.9 Identifying Ionization

In this section, I will discuss how I identified ionization in our scattering signal qualitatively. It has been discussed in section (1.6) that the electronic dynamics exclusively contributes to low s features which is experimentally observed in Ref[52], [53]. In Figure 3.4a, we see a sharp feature at $0.55 < s < 1.1\text{Å}^{-1}$, which persists for the entire observational time window. We rule out the possibility of inelastic scattering since the signal does not decay in 500fs, which is the excited state lifetime of cis-stilbene [119]–[121]. The ionization potential of cis stilbene is 7.38eV, so, two-photon excitation using 267nm photon can lead to ionization. Sri Bhavya Muvva in our group calculated atomic form factor (AFF) of carbon cation (f_{C^+}) using first born approximation. We account the C$^+$ in the scattering calculation in the following way:

$$I_{at}^{+} = I_{at} + (-|f_C|^2 + |f_{C^+}|); \tag{3.1}$$

And,

$$I_{mol}^{+} = \sum_{i=1}^{n} \sum_{j\neq i}^{n} |f_i||f_j| \frac{\sin(sr_{ij})}{sr_{ij}}; \begin{cases} when\ f_i = f_{10},\ f_i = f_{C^+} \\ when\ f_j = f_{10},\ f_j = f_{C^+} \end{cases}. \tag{3.2}$$

Where, I_{at} is the atomic scattering intensity of neutral cis stilbene, f_C is the AFF for electron scattering of neutral carbon, r_{ij} is the internuclear distance between i^{th} and j^{th} atom. In equation (3.2), f_i and f_j accounts for the AFF of carbon atom for $i, j = 1\ to\ 12$.

In calculation of I^+_{mol}, we replace the 10^{th} neutral C atom by the C^+, so when $i = 10$, or $j = 10$, we replace f_c by f_{C^+}. We found that the I^+_{mol} does not change by changing the position of C^+ in the stilbene molecule. The sum of equation (3.1) and (3.2) gives:

$$I^+_{tot}=I^+_{at} + I^+_{mol}. \tag{3.3}$$

We calculated difference diffraction by using the following formula for the case using:

$$\frac{dI^+}{I}(s) = \frac{I^+_{tot}-I_{tot}}{I_{tot}}. \tag{3.4}$$

Where, I_{tot} is the total scattering intensity of neutral cis stilbene. In calculating I_{tot} and I^+_{tot}, we choose one single structure so that we can see only the effect of ionization.

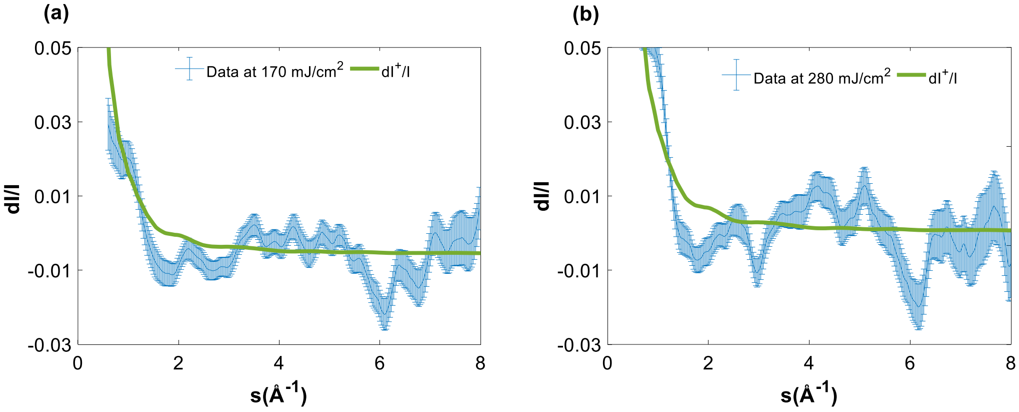

Figure 3.5: Qualitative identification of ionization. The blue lines with error bars are showing the time-averaged $\frac{dI}{I}$ signal in 835-962 fs for fluences (a) 170 mJ/cm^2 and (b) 280 mJ/cm^2. The green line represents $\frac{dI^+}{I}$, calculated using equation (3.3).

Figure 3.5 shows the qualitative comparison between the experimental $\frac{dI}{I}$ and $\frac{dI^+}{I}$, which we calculated using equation (3.3). $\frac{dI}{I}$ is calculated by averaging the $\frac{dI}{I}$ of experimental data averaging in 835-962 fs. For overlaying the curve onto one another, we scaled the

$\frac{dI^{+}}{I}$ by a factor of 10. It is evident from Figure (3.4), the effect of cation shows a rise at the low s, which resembles the feature we found in our experimental data. This resemblance can be attributed to the ionization present in our experimental signal.

3.2.10 Transforming simulated ΔsM to ΔPDF

We calculated the ΔsM and then ΔPDF using equations (2.7) and (2.8) for the scattering simulation done for 2-photon excitation channel. For the case of experiment, a hole is drilled at the center of phosphor screen to allow the un-diffracted beam to pass through the hole. Experimental data is not possible to capture at $s < 0.5\text{Å}^{-1}$ because of the hole. When it needs to transform the experimental ΔsM, this can be done in a number of ways. Firstly, the s-range can be ignored. However, this introduces some artifacts in the ΔPDF. The second method of filling the low-s range is to use properly scaled simulation. Although this is mostly used method, it puts more weight on simulation and the data can be highly biased by this simulation. Another method is to smoothly interpolate the data to zero. The experimental data has a sharp peak due to ionization at low s. For interpolating the data to zero, we need to separate the signal due of ionization and subtract it. Since we lack ab initio scattering calculations to compare the trajectories with our experimental data, we could not separate the electronic contribution from our experimental data. Consequently, we could not transform experimental ΔsM to ΔPDF.

3.2.11 Fourier transform the time-dependent data

To capture the frequency of oscillation of different vibrational mode after ionization, we Fourier transform the time dependent $\frac{dI}{I}$ of both experimental data and two-photon excitation simulation. For experiment we use data for 280 mJ/cm^2 fluence, since the data correspond to this fluence predominantly shows ionization. Unlike the $\frac{dI}{I}$ in momentum space, time dependent $\frac{dI}{I}$ has not the problem of filling missing range during Fourier transformation, since we have $\frac{dI}{I}$ at $t = 0$. We average the $\frac{dI}{I}$, over various s range: $1.48 < s < 2.35Å^{-1}, 4.12 < s < 4.67Å^{-1}, 5.9 < s < 6.6Å^{-1}$. We use a time-range $0 - 1ps$ to Fourier transform the time-dependent $\frac{dI}{I}$. We use MATLAB's standard code for fast Fourier transformation to do the transformation. Additionally, we use the Tukey window to dampen the sharp edges on the time-dependent lineout to merge into the baseline. We also Fourier transform the 2-dimensional ΔPDF calculated from the 2-photon excitation simulation to capture the inter-nuclear distances that contribute to the vibration using the same procedure outlined in this section.

3.3 Results and discussions

In this section, we present the key findings from our research on photodynamics of CS. The purpose of this section is to analyze and interpret these results in depth. We will begin by discussing static data analysis, followed by an exploration of time-dependent analysis. These insights contribute to our understanding of the dynamics for 2-photon excitation channels.

3.3.1 Static data analysis of stilbene

In this section we delve into the analysis of ground state data of CS. By analyzing the static data and comparing it with theoretical counterpart, we will validate that CS preserve its structural property before being photoexcited during experiment. For static analysis, we will look into modified scattering intensity (sM) and pair distribution function (PDF).

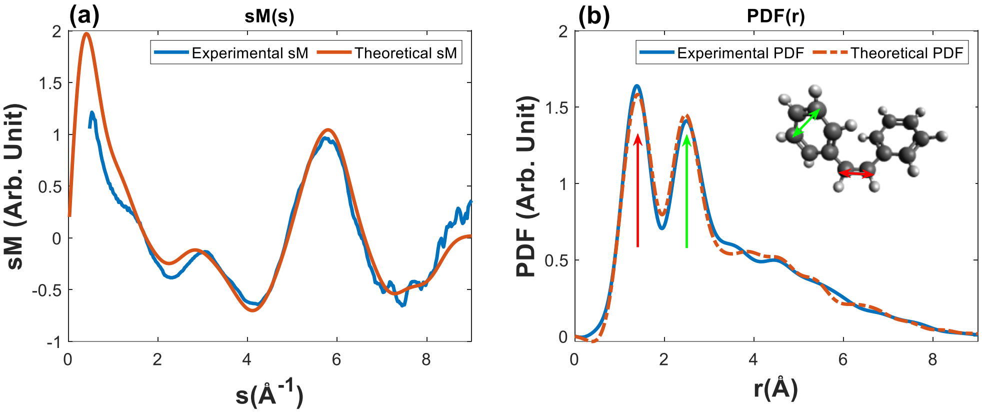

Figure 3.6: (a) Modified scattering intensity, sM for ground state CS. The blue curve is the experimental sM, and the red curve is the theoretical sM calculated from the structure simulated by using Wigner distribution at 0°C. (b) The pair-distribution function (PDF) is shown for experiment and theory. The major peaks correspond to the nearest C-C distance at 1.35Å and 2nd nearest C-C distance at 2.34Å, as indicated by the red and green arrows on the structure in the inset. Some other peaks appeared but were not pronounced as the first two peaks.

Figure 3.6 shows the sM and PDF as functions of s and r, respectively. For the theoretical $sM(s)$ (TsM), the total scattering intensity was calculated from ground state structures generated using the harmonic Wigner distribution at 0K. Figure 3.6a shows a good agreement between TsM and experimental sM. The $PDF(r)$ is shown in Figure 3.6b. The sharp peak that appears at 1.35Å, denoted by the red arrow, indicates the interatomic distance of the closest C-C distance, as shown on the molecular structure in the inset. The peak at 2.34 Å, indicated by the green arrow, denotes the 2nd nearest C-C distance. Some other peaks also appeared at higher r; however, those are not as intense as the first two peaks, and those peaks are responsible for different C-C distances.

3.3.2 Time-dependent Analysis

In this section, we will discuss the time-dependent analysis of the experimental data by comparing them with 1-photon excitation and 2-photon excitation simulations. Time-dependent data exhibit the evolution of scattering signals, revealing the dynamics induced by photoexcitation. We will first qualitatively compare the two-dimensional difference-diffraction ($\frac{dI}{I}$) signal of experimental data obtained using $170mJ/cm^2$ and $280mJ/cm^2$ pump fluences with 1-photon excitation and 2-photon excitation simulations. Then, we will delve into the quantitative analysis of the time-averaged $\frac{dI}{I}$ signal to determine the contribution of 1-photon and 2-photon excitation in our experimental data. Subsequently, we will analyze various time-dependent features in the $280mJ/cm^2$ pump fluence data, which predominantly exhibits ionization, and compare these features with the 2-photon excitation simulation. We will Fourier transform the features and extract the frequency of vibration. We will also show which mode is responsible for the most pronounced vibration.

Figure 3.7a and 3.7b show the 2D plot for the dI/I for CS for pump excitation fluences of 170mJ/cm^2 and 280mJ/cm^2, respectively. The experimental data was convolved with a 100 fs FWHM Gaussian along the time axis to reduce noise. In these figures, it is clearly seen that a pump-probe signal appears after time zero, where time delay is denoted along the horizontal axis, and the momentum transfer vector, s, is represented along the vertical axis.

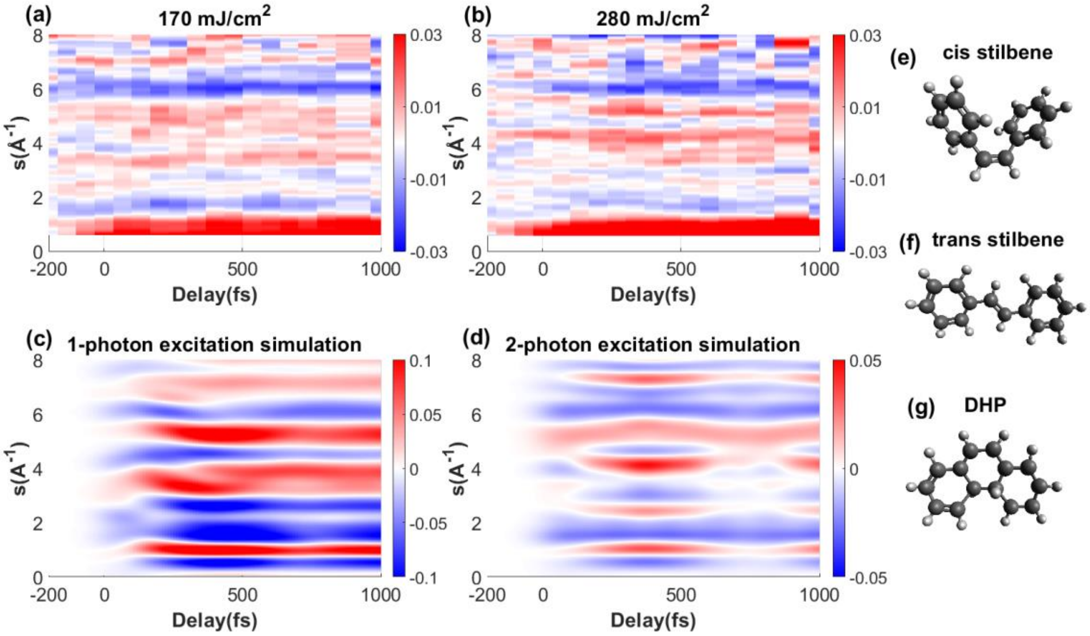

Figure 3.7: Time-dependent pump-probe signal expressed by the relative difference of total scattering intensity, dI/I, and structures of different products. (a), (b) Experimental 2D dI/I signal for $170mJ/cm^2$ and $280mJ/cm^2$ fluence, respectively. Here, the vertical axis is the momentum transfer vector, s, and the horizontal axis is the pump-probe delay. (c), (d) The 2D dI/I calculated using AIMS simulation and MD simulations, respectively, at the time range of 1ps (e) (f) (g) Structures of different end products at the end of one-photon dynamics.

Figure 3.7c shows the corresponding dI/I based on the nonadiabatic dynamics simulations for the 1-photon channel, performed with Ab-initio Multiple Spawning (AIMS) on a CASSCF / 6-31G* potential energy surface[134]. The simulation was done by Dr. Hayley Weir. The diffraction signal is calculated using the IAM and averaging the signal over all the trajectories. We applied a convolution with Gaussian of 150 fs FWHM on 1-photon excitation simulation along the temporal dimension to match the IRF of the experiment. The 1-photon excitation simulation predicts an end-product ratio of 44:52:4 for CS:TS:DHP, and the structures are shown in Figure 3.7(e, f, g). Comparing the dI/I for both experimental data and 1-photon excitation simulation, we observed some significant differences. In particular, at low s ($s < 1$ Å^{-1}), the experiment shows a strong positive feature while the theory shows negative signal in this region. We attribute this strong positive signal to additional scattering due to the charge in the molecule. This signal is not captured by the IAM which assumes neutral molecules [52], [53]. As expected, this signal persists for time since the molecule remains charged after ionization. The ionization potential of CS is 7.38eV[128]; thus, by absorption of two photons with energy of 4.6 eV the molecule is ionized.

The time-dependent CS$^+$ structures were also generated by Dr. Hayley Weir. She did the simulation using molecular dynamics (MD) simulation using unrestricted B3LYP / 631G* basis function. I calculated the diffraction signal from the time-dependent structures using the IAM and averaging the diffraction signal over all trajectories. Figure 3.7d shows the calculated dI/I for the stilbene cation (CS$^+$) after convolution with a Gaussian of 150 fs FWHM to match the IRF of the experiment. In Figure 3.7b and Figure 3.7d, we see a good qualitative agreement along different features at different s between the experiment and 2-photon excitation simulation. Again, the positive feature at low s does not appear in the theory since the IAM does not capture it; however, the features at higher s show a good match in position and time evolution.

In the work of Xiong et al., it was shown that the effect of ionization can be accounted for accurately using ab-initio scattering calculations instead of the IAM and that the main differences between the two models appear at $s < 2$ Å^{-1}[52], while the signals are very similar at higher s. Thus, we use our IAM model to compare the experiment and theory in the range of $s > 2$ Å^{-1}.

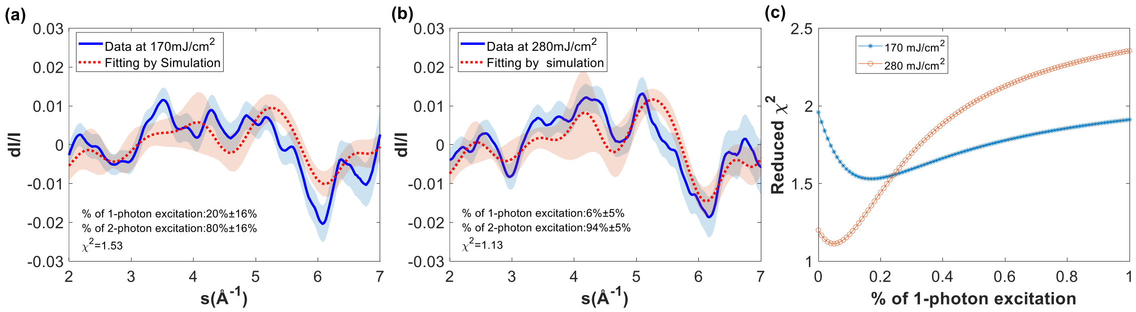

Figure 3.8: **Fitting the experimental data using a combination of 1-photon and 2-photon excitation simulation.** (a) Experimental data for 170mJ/cm^2 fluence, and (b) 280mJ/cm^2 fluence. Each of the plots has a lineout of experimental data averaged at 770-960fs indicated by the blue curves. 1-photon and 2-photon excitation simulations are averaged at 800-1000fs and fit to the experimental data. The fittings are indicated by red curves. The shade on each curves represents uncertainty. The χ^2 for the fitting with 170 mJ/cm^2 is 1.53, whereas χ^2 for the fitting with 280 mJ/cm^2 data yields χ^2= 1.13. (c) Dependence of reduced χ^2 as a function of the percentage of 1-photon excitation in the dynamics.

We compare experiments and theories at higher scattering angles to capture the structural changes and avoid the low angle signal from ionization. We fit the experimental data, averaged at 770-960fs time window, by a linear combination of the calculated signal averaged at 800-1000fs time. Figure 3.8a and 3.8b show the experiment and fitted curve for the low and high fluence cases, respectively. The shaded region in the experimental data represents the 68% confidence level calculated using bootstrapping. In the simulations, the shaded region represents one standard deviation calculated from 100 trajectories for the 1-photon excitation simulation, and from 20 trajectories for the 2-photon excitation simulation. For the low fluence the best fit (reduced χ^2 = 1.53) is for a relative yield of 80%±16% for ionization and 20%±16% for the valence excitation. The total excitation percentage including both channels was found to be 34±11 % based on the result of the fitting. Similar fitting was done for the experimental data at high fluence, with a reduced χ^2 = 1.12 and relative yield of 94%±5% for the 2-photon channel, with a total excitation percentage of 58%±12. In this case, the ionization channel is dominant. The increased yield in ionization is consistent with a two-photon process where the ionization probability is proportional to the square of the laser intensity. Figure 3.8c shows the variation of reduced χ^2 for different percentages of 1-phton excitation. Clearly, the best fitting occurs at ~20% 1-photon excitation for lower fluences, whereas for higher fluence, the contribution from 1-photon excitation is negligible, close to 6%.

We also fitted the experimental data using the combination of simulation at various time intervals. We observed that the best fitting happens at a later time, specifically in 770-960fs window, for both fluences. We attribute this to the ionization process of the CS, wherein it transitions to higher ionized states, namely, D_1-D_2[150]. From these upper ionized states, it takes some time to relax to the ionic ground state, D_0 and settles there.

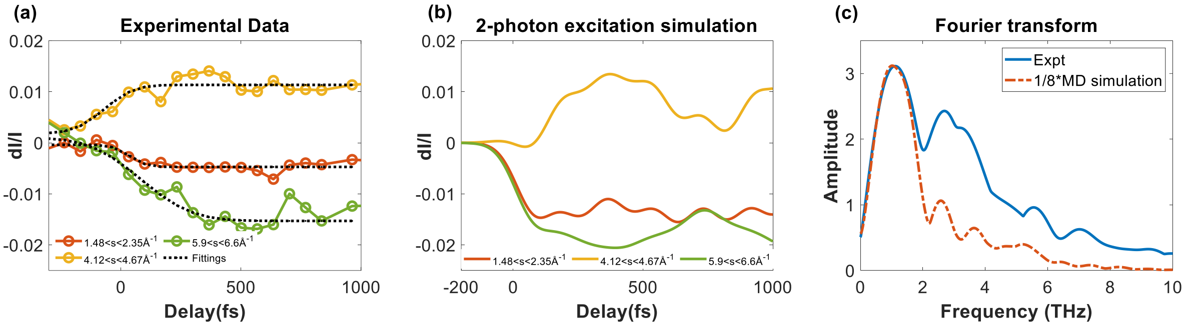

Figure 3.9: Time-dependent lineouts and their Fourier transform for the data of $280 mJ/cm^2$, which mostly shows ionization. (a),(b) lineouts along the features averaged in the s-range as indicated by the legends. 2-photon excitation simulation is convolved by 150fs Gaussian along the time axis. Both experimental data and simulation have similar trends. These features are Fourier transformed and shown in Figure (c). Both the experimental data and simulation have sharp peaks in the vicinity of 1.05THz. This frequency corresponds to the phenyl ring motion about the central C-C bond.

We examine the high fluence case to investigate the dynamics of CS^+. Figure 3.9a and 3.9b show lineouts extracted from the main features in Figure 3.7b and Figure 3.7d, respectively. The lineouts were calculated by averaging the signal over the s-range indicated in the figure legend. Each of these lineouts was fitted by the error function shown by the black dotted lines. The error function fits show the general trend, while the data also contains amplitude oscillations about this trendline. The general trend and some of the oscillations are reproduced in by the theory lineouts in Figure 3.9b. The simulations assume the wavefunction starts in the D_0 ionic state, while experimentally, the ionization might lead to higher states. Based on the agreement between experiment and theory, it is reasonable to conclude that the higher states relax to D_0 within 200 fs to 300 fs. The oscillations in the amplitude of the lineouts can be attributed to motion in the D_0 potential well.

We compare the vibrational frequencies in the experiment and theory with a Fourier transformation (FT) of the time-dependent features individually. The trendline from the error fitting curve was subtracted from the lineouts prior to performing the FT to focus on the vibrations, and a similar procedure was used for the theory lineouts. The resulting spectra after FT of each lineout were added to create the spectra in Figure 3.9c. The dominant frequency and even the higher order frequencies are in close agreement between experiment and theory. The dominant frequency peaks at 1.1 THz in the experiment and 1.03THz in the simulations.

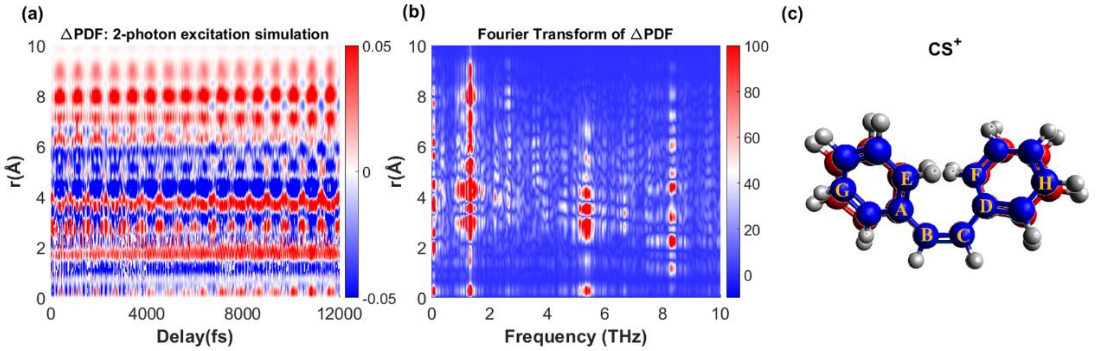

Figure 3.10: 2D ΔPDF and its Fourier transformation. (a) The 2D plot shows the ΔPDF of cis stilbene cation over full simulation time. Here, no convolution applied. (b) Fourier transform of the time-dependent ΔPDF at plot (a). The most prominent peak is found at ~1.3THz, which matches the frequency found in the experimental data. This frequency corresponds to the vibration of the phenyl ring about the central C-C bond. Plot (c) shows the structure of molecules at two extremes in a vibration. Here, different colors are used to indicate two different states.

We can further investigate the vibrational modes of the molecule in the ionic ground state by extending the simulation time up to 12 ps. Figure 3.10a shows the $\Delta PDF(t)$ generated from the simulation. It is clear that the periodic motion persists over multiple periods and includes vibration in short and long distances. Here, we did not use a convolution in time (as in Figure 3.9) to also capture the higher frequency vibrations. A FT of the ΔPDF reveals which distances are active at each vibrational frequency (Figure 3.10b). The dominant peak appears at 1.3 THz, corresponding to the dominant peak observed in Figure 3.9c. Here, we can see that this motion involves both short and long distances in the molecule, from 2.5 Å to 9.3Å. The main contributions for the higher vibrational frequencies are from the shorter distances. The broad band observed Figure 3.9c in the range between 2-4 THz can now be resolved into individual peaks due to the extended time range in the simulation. Additional peaks also appear at 5.3THz and 8.1THz, which were not captured in the experiment due to the limited temporal resolution of 150 fs. We calculated the vibrational frequency modes for the optimized CS^+ structure using density functional theory at the def2-SVP basis function of the orca ab initio software[151]. The resulting frequencies were then visualized and compared with experimental data using Avogadro[152]. We identified the frequency of 1.3THz as the vibration of the phenyl ring about the central C-C distance. Figure 3.10c shows the structure of the cation. In the ionic ground state, the phenyl rings are not completely planar and are slightly facing out of plane. Due to this motion, both rings approach one another and then move away. The CS^+ structure at two endpoints of the vibration is shown in the figure using different colors. The distance between atom G and atom H varies between 7.828Å and 8.150Å. Similarly, the distance between E and F atoms also varies between 3.132-3.150Å. The motion can be viewed by the change of angle BCD as well. It changes between 129.9° and 133.3°. A similar change happens for the angle ABC. However, there is no change observed for the ABCD dihedral angle. Because of this motion, an overall stretching is observed in the ΔPDF of CS^+.

3.4 Summary

Using MeV-UED as a probe, we simultaneously observed one-photon dynamics and ionization in a single experiment. The sharp, low-angle scattering signal is attributed to ionization, which the IAM diffraction calculations do not capture. Using two different pump laser intensities, we were able to identify the relative contributions of the 1-photon and 2-photon channels, corresponding to valence excitation and ionization. We explored the dynamics triggered by ionization, which had not been investigated in detail before. The MeV-UED study on the ionization dynamics of cis-stilbene gives us the experimental evidence about the topology of the ionic state. After exciting to higher lying ionized state, cis stilbene cation decay to ionic ground state in about 300fs. in the ionic ground state, cis stilbene cation traps in potential well, where is vibrates through periodic structuration change. The periodic nature of potential in the well is revealed by the vibrational mode.

Chapter 4

Experimental Techniques and Data Acquisitions of Low Vapor-Pressure Molecules

4.1 Introduction

In this chapter, I will describe the detailed procedure for conducting UED experiment using low vapor pressure sample. By low-vapor pressure, we mean a sample's molecular density is very low which cannot make any detectable diffraction signal due to interaction with electron, when the number of electrons per pulse is optimized to get the best temporal resolution. In section 4.2, I will describe why we need to heat low vapor sample to get higher vapor pressure and get good diffraction signal. Ultrafast electron diffraction (UED) employs a pump-probe technique to investigate photo-induced molecular dynamics. The heart of our KeV-UED lab is a femtosecond laser system that generates the pump laser pulse and probe electron beam. The details of the pump-probe arrangement are discussed in the earlier reports[31], [40], [153]–[155]. Nevertheless, in section 4.2, I will briefly talk about the laser system and electron optics used in our lab. Besides the pump-probe setup, the sample delivery system and its management are another crucial component in the experiment. I will give a comprehensive description of the sample delivery system and procedure of running gas phase UED experiment using low vapor pressure sample in section 4.3-4.6.

4.2 Necessity of heating

In this section, I will illustrate why we need to heat the sample to get a good scattering intensity. In a typical gas phase UED experiment, the extent of scattering of electron by target molecules depends on scattering cross section of the target molecule, diameter of the gas jet, and the number density of gas molecule in the interaction zone [40]. Heating the sample results in increase the vapor pressure, so that the number density of gas molecule can be higher in the interaction region. The gas density, n , at a distance x from the nozzle exit can be expressed using the following relation:

$$\frac{n}{n_0} = \frac{M}{f^{\frac{1}{2}}}\left(\frac{d}{x}\right)^{2+\frac{2}{f}} \tag{4.1}$$

Where, we used equations (2), (7), and (10) from reference [156]. In equation (4.1), n_0 is the gas density at the nozzle stagnation region, f is the number of active degrees of freedom of molecule, d is the diameter of the orifice of the nozzle, and M is the Mach number. For supersonic jet, Mach number lies between 1.3-5.

We did gas phase UED experiment using the vapor of toluene[52] and got a good scattering signal. We can first look at the number density of gas molecules for that experiment and estimate how much heat we would need to apply to get the same number density as PMCP at the interaction region. Toluene is a liquid at room temperature, and it has vapor pressure 28.4 Torr. We can calculate the gas density using the ideal gas law:

$$PV = Nk_BT; \frac{N}{V} = \frac{P}{k_BT}; n = \frac{P}{k_BT}; \tag{4.2}$$

Where, n is the gas number density, P is the vapor pressure, k_B is the Boltzman constant, T is the temperature of the gas. At, $T = 298K,$ the number density of toluene corresponding to 28.4 Torr vapor pressure is estimated using equation (4.2) is $9.21 \times 10^{17}/\ \mathrm{cm}^3$. We can use C_p to calculate f using the following relation:

$$C_p = \left(\frac{f}{2} + 1\right)R; f = 2\left(\frac{C_p}{R} - 1\right) \tag{4.3}$$

Where, R is the ideal gas constant. At room temperature, $C_p = 103\, Jmol^{-1}K^{-1}$ for toluene gas[3] which gives $f \approx 23$. If the interaction happens at a distance $150\mu m$ from the nozzle exit, and the nozzle has an orifice diameter 50 $\mu m,$ then using equation (4.1) we get,

$$\left(\frac{n}{n_0}\right)_{Toluene} = 0.03.$$

Where, we used $M = 1.3$, considering the jet is supersonic. Hence, the gas density in the interaction region is therefore, $n_{Toluene} = 2.7 \times 10^{16}/cm^3$. Which is about 30 times lower. For molecules like PMCP, the vapor pressure at room temperature is even lower compared to toluene. PMCP has vapor pressure about 2 Torr at room temperature[4]. The gas molecule density at this pressure is thus 6×10^{16} /cm^3, as estimated from equation (4.2). For PMCP, $C_p = 225\, Jmol^{-1}K^{-1}$ at room temperature. In this reference[5], C_p is given for different temperatures, and they showed the C_p varies with temperature as a fourth order polynomial of temperature. I fitted the given C_p vs T plot and extracted C_p at room temperature. Using (4.3) we get, $f \sim 50$. Using the same values of $M, x = 100\mu m$, and $d = 150\mu m$, we get $\left(\frac{n}{n_0}\right)_{PMCP} = 0.08$, and $n_{PMCP} = 4.8 \times 10^{15}\ /cm^3$. Evidently, n_{PMCP} is about 6 times lower than $n_{Toluene}$ in the interaction region, even with twice the orifice size. To get $n_{PMCP} = 2.7 \times 10^{16}/cm^3$, same density as Toluene, in the interaction region, we

---

[3] Toluene - Thermophysical properties. (n.d.). https://www.engineeringtoolbox.com/toluene-methylbenzene-properties-d_2095.html

[4] https://www.chemsrc.com/en/cas/4045-44-7_1032551.html.

[5] 1,3-Cyclopentadiene, 1,2,3,4,5-pentamethyl- (CAS 4045-44-7). (n.d.). Cheméo. https://www.chemeo.com/cid/46-212-5/1-3-Cyclopentadiene-1-2-3-4-5-pentamethyl

need $\sim 3.4 \times 10^{17}\ /cm^3$ in the backing section. This would be possible if we can raise the vapor pressure of PMCP to $\sim 10\ Torr$ that corresponds to gas density $\sim 3.4 \times 10^{17}\ /cm^3$, found using equation (4.2). By applying heat, we can raise the vapor pressure of the sample since the vapor pressure is directly proportional to the temperature. The vapor pressure and temperature relation can be found using Clausius–Clapeyron equation which is given by:

$$\ln\left(\frac{P_1}{P_2}\right) = \frac{-\Delta H_{vap}}{R}\left(\frac{1}{T_1} - \frac{1}{T_2}\right). \tag{4.4}$$

Where, P_1 and P_2 are vapor pressure at temperature T_1 and T_2, respectively, ΔH_{vap} is the enthalpy of vaporization. For PMCP, $\Delta H_{vap} = 39KJ/mol.$ Since at room temperature, $T_1 = 25°C$ and $P_1 = 2\ Torr$, using equation (4.4), we can get $P_2 = 10\ Torr$ at $60°C.$ In this experiment, we gradually heat the sample and observed a good scattering signal at $70°C$, which provided a vapor pressure of 13 Torr, calculated using equation (4.4).

Now, I will show a quantitative comparison on scattering intensity in the interaction zone. The different nozzle size and different vapor pressure contributed to the difference in the gas density in the interaction region. Apart from the gas density in the interaction region, scattering intensity depends on the scattering cross section. The cross section measures the probability of scattering happening depending on the number of incident particles. In the UED experiment of toluene, we used electron bunch with 8750 electrons/pulse, an electromagnetic gain of 300 and 60s exposure for each image. We calculated the total scattering count within 100–200-pixel range about the diffraction center. This gives us total scattering intensity ~11500 counts, where we normalized the intensity by the gain and exposure time. In the UED experiment using PMCP, we used electron bunch with 25000 electrons/pule, an electromagnetic gain 300 and 30s exposure for each image. Using the similar calculation and normalization we get an intensity with ∼9500 counts.

Even though the incoming electron beam has higher electron per pulse for the case of PMCP, the scattering intensity is lower than the case of toluene. This can be justified by another factor, the diameter of the gas jet. We don't have this data for PMCP experiment which prevents us from further comparing the scattering intensity between the UED experiment using toluene and PMCP. Moreover, the geometry of the nozzle was different for the two experiments. In our calculations, we used same Mach number ($M = 1.3$) for experiment for simplicity. However, in the actual experiment this number might be different which can be regarded as another potential source of discrepancy in the scattering intensity.

4.3 Femtosecond laser pump and KeV electron probe setup

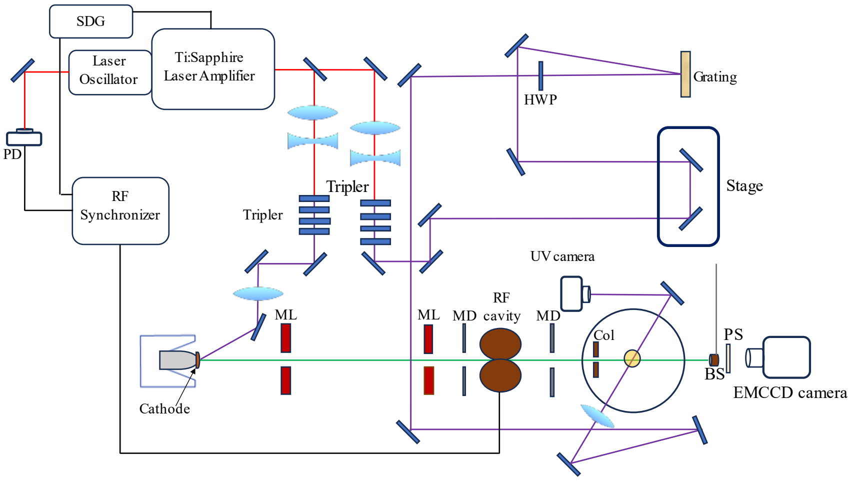

Figure 4.1: Schematic diagram of the optical and electron-optics setup. The schematic shows different components used in the pump laser path and probe electron path. Here, SDG: synchronization and delay generator, PD: photodiode, HWP: half-wave plate, ML: magnetic lens, MD: magnetic deflector, col: collimator, BS: beam stop, PS: phosphor screen.

Figure 4.1 shows the optical setup for the ultrafast electron diffraction experiment using a KeV electron beam. A Ti: sapphire laser system generates a laser pulse centered at 800nm with a bandwidth of 30 nm. The system consists of a mode-locked oscillator (Coherent Vitara) and a chirped pulse amplifier (CPA) (Coherent Astrella). From the oscillator, a laser pulse with a central wavelength of 800nm is seeded to the CPA at a rate of 75MHz. One of the cavity end mirrors is mounted on a stage to change the cavity length as required to stabilize the oscillator frequency. From CPA, the pulse output has an energy of 7.35mJ (7.35W total power) with a repetition rate of 1KHz and a pulse duration of 30fs. About 10% of the IR output (0.70W) is then sent to a frequency tripler where UV of 267nm wavelength is generated. This UV beam is then directed to a photocathode, where the photoemission process generates electrons. A neutral density filter wheel is mounted to control the energy of the UV beam hitting the cathode allowing the electron current to be controlled. After adjusting the filter wheel, the UV pulse energy was measured 0.25μJ. This wheel is motorized and computer-controlled by a data acquisition program, which will be described in section 4.6.8. The photoemitted electrons are accelerated by using a 90KV DC electric field. Electrons are guided to the target chamber and transversely focused by magnetic deflectors and lenses, respectively. The electron beam is longitudinally compressed by a RF cavity using the same techniques described in Ref[22], [23] . The principle employed in longitudinal compression is that a time-varying RF field decelerates the leading part of the electron pulse while the tail of the pulse is accelerated. The whole system is synchronized with respect to the laser oscillator[32]. Part of the laser oscillator output is sent to a homemade synchronizer[31] using a photodiode, which convert the oscillator output into electrical signal. This synchronizer generates 3GHz signal, amplifies and feeds it into the RF cavity. The synchronizer also ensures a precise timing between the arrival of the electron beam at the center of the cavity and the phase of the RF electric field for maximum compression[31]. A platinum aperture of 300μm collimates the electron beam to deliver about 25000 electron per pulse at the target position. The aperture is mounted on a 2D movable collimator, which is used to optimize the maximum electron current through the aperture. The purpose of the aperture is to reduce the electron size and discard the diffused electrons. A laser-activated streak camera measures the electron pulse duration at the target[157]. The electron beam current is measured by a Faraday cup, which is also used as a beam stop to prevent the main electron beam from passing to the phosphor screen. For gas-phase UED experiment of PMCP, the electron beam had a current of about -4pA, which corresponds to 25000 electrons per pulse.

The majority, about 90% (6.4W), of the laser amplifier output is sent to another tripler to generate another 267nm laser pulse, which is used as the pump for the experiment. This UV pump has an estimated pulse duration of 135fs using a home-built autocorrelator. The velocity mismatch between the pump and electron pulse while traversing the sample is removed using a tilted font laser pulse[158], [159]. The front tilting is produced using a Al-coated diffraction grating with a grating constant 400mm^{-1}. This tilted front UV beam is then directed to the target chamber at an angle of about 60° with respect to the propagation direction of the electron beam, where the velocity component of light along the direction of electron beam matches the electron's velocity. After passing the target chamber, the UV beam is imaged on a UV camera (Thorlabs 340UV-GE). Using a thin lens, first the sample delivery nozzle is imaged on the UV camera. Then using another thin lens, the grating is imaged on the sample position, which is viewed by the UV camera. A precise imaging can give us a minimum pulse duration at sample position[155]. The detection system consists of a 39mm diameter phosphor screen (Beam Imaging Solutions: P43 Type Phosphor). The phosphor screen is imaged onto an Andor ixon-888 electron multiplying charged coupled device (EMCCD) camera, by an aberration-free optical lens (Nikon, NIKKOR 50mm f1/2. The detector has a 1024×1024 pixel array and each pixel size is $13\mu m.$ For spatial overlap between the gas nozzle and electron, we usually move the nozzle position perpendicular to the laser beam path to maximize the scattering. To do the spatial overlap between the UV laser and gas nozzle, first the UV beam is focused on the gas jet exerted from the nozzle. The focused laser beam causes the gas to fluoresce. We use CF_3I as a reference gas for spatial overlap, since CF_3I gives a higher fluorescence intensity. CF_3I is found to fluoresce even with the tilted UV pulse[155]. The fluorescence intensity is made maximum by moving the pump laser using a mirror just before the target chamber. The fluorescence is viewed by a CMOS camera (Thorlabs DCC1545M) which is mounted with the target chamber through a view port. The camera is located at about 150° with respect to the incoming electron beam direction. Once the spatial overlap is done, the temporal overlap is done using the plasma-lensing method[18], [160]. The plasma lensing is also used to vertically overlap the electron and pump laser pulse[155]. We found CF_3I is an ideal gas to check both the spatial and temporal resolution in terms of the fluorescence and plasma-lensing effect, respectively.

4.3.1 Third harmonic generation

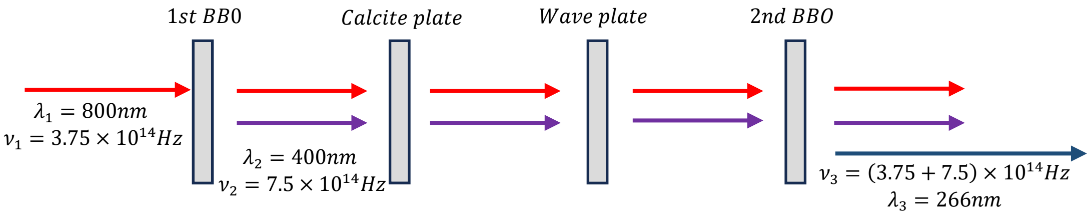

Figure 4.2: Schematic of third harmonic generation from 800nm laser pulse. The setup consists of a BBO crystal followed by a calcite plate. After the calcite plate there is a waveplate and then another BBO crystal to generate the third harmonic laser pulse. The corresponding wavelength and frequency after conversion from the BBO crystal are also shown.

In our setup, we need to generate a third harmonic of 800nm laser pulse to a) generate an electron beam via photoemission, and b) generate the pump beam to excite the molecules. The tripler optics consist of a Beta Barium Borate (BBO) crystal, which can effectively generate 2nd harmonic light of 400nm from 800nm. However, for generating a 267nm pulse, we use a couple of BBO crystals so that the third harmonic light can be produced by sum frequency generation. After the 800nm IR beam passes through the 1st BBO, it produces 800nm and 400nm pulses. These pulses have different group velocity because of their difference in refractive index. To match the group velocity between these two beams, a properly cut birefringent calcite crystal is used after the 1st BBO. After the calcite plate, a waveplate that works as a half waveplate for the 800nm is inserted. The waveplate acts as a full waveplate for 400nm, hence does not alter the polarization of 400nm pulse. After exiting the 1st BBO, the generated 400nm has opposite polarization than that of the 800nm pulse. The waveplate rotates the polarization of the 800nm pulse to match with the polarization of 400nm. Third harmonic light of 267nm is produced along with 800nm and 400nm after the 2nd BBO. Light with 267nm is extracted using a harmonic separator, which transmits the 267nm light and reflects the 800nm and 400nm lights.

4.4 Overview of sample delivery system

In this section, I will give an overview of the sample delivery system by showing a schematic diagram. I will describe the main parts, their purpose and how they are connected.

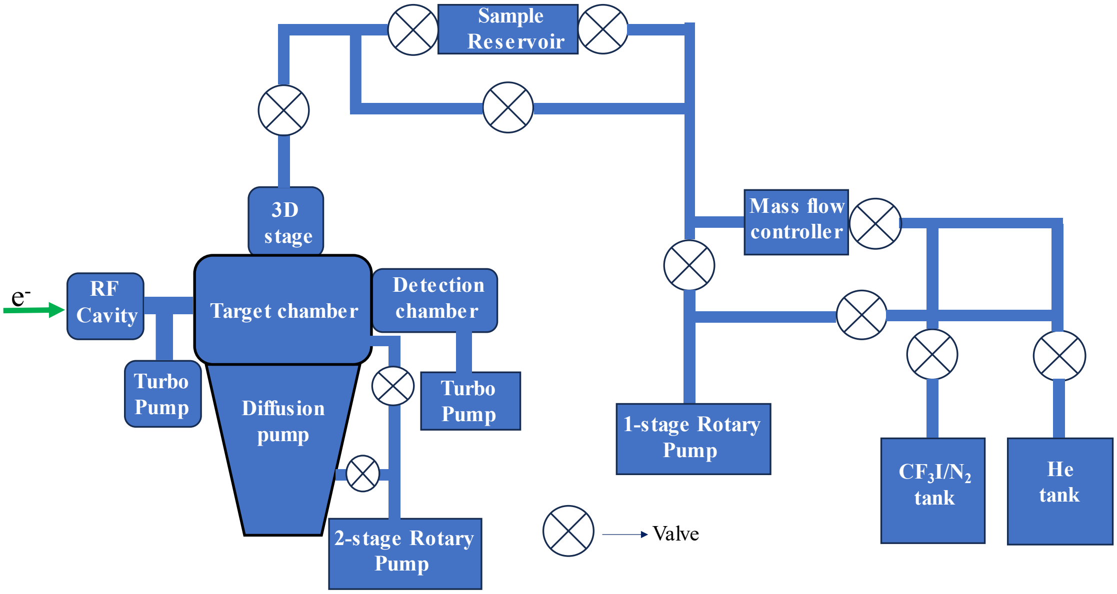

Figure 4.3: Schematic diagram of the sample delivery system. Various main parts and their interconnections are shown.

In Figure 4.3, we present a schematic layout of the sample delivery system (SDS), illustrating its various components and their connections. This particular SDS was designed and implemented for gas-phase electron diffraction experiments using the vapor of liquid and solid samples. The sample includes PMCP, thymine, iodobenzene [155], and Toluene [52].

The central component of the SDS is the target chamber. It's a custom-built cylindrical enclosure made of stainless steel with an inner diameter of 7.8 inches and height about 11 inches. High vacuum within the target chamber is maintained by a diffusion pump (Edwards CR250/2000, with a pumping speed of 1700 l/s for N2), which is backed by a two-stage rotary vane pump (Edwards E2M40). The two-stage rotary pump can also rapidly reduce the pressure in the target chamber from 10 Torr to 2.5×10^{-2} Torr, when necessary.

Connected to the target chamber is a 4.5-inch cube which houses a 39mm phosphor screen, forming the detection chamber. The detection chamber is connected to a turbo-molecular pump (Pfeiffer Hipace80) with a pumping speed of 67 l/s. Another similar turbo pump (Leybold Turbovac 70) is connected with a cross to ensure high vacuum within the RF cavity. Both turbo pumps are backed by a single stage rotary-vane pump (Edwards RV3). Pressure in the target chamber and RF chamber is measured using hot filament ion gauge (Kurt J. Lesker, 354 Series) when the pressure is below 1×10^{-4} Torr. For pressures above this range, the pressure in the target chamber is measured using a micro-Pirani transducer (MKS Gransville-Phillips, PN: 925-11014). Another Pirani Gauge is used to measure the critical backing pressure of the diffusion pump (MKS Granville Phillips 275 series).

A 3D stage (MDC precision) is located on top of the target chamber. The stage facilitates the three-dimensional movement of the tube-nozzle assembly to ensure spatial overlap with the incoming electron and pump laser beam.

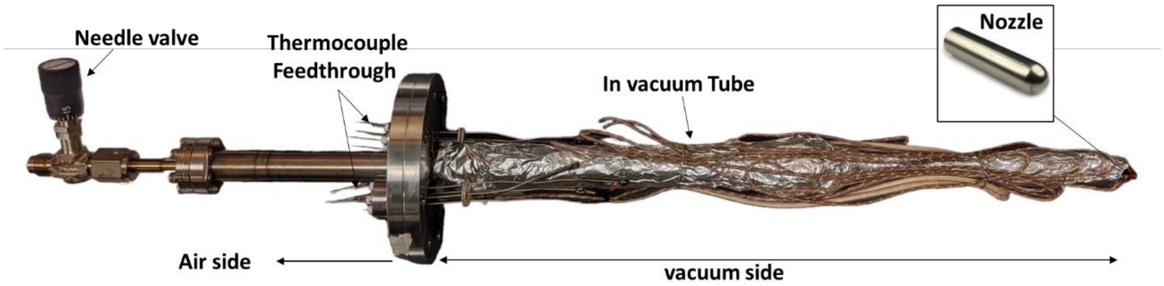

Figure 4.4: Tube-nozzle system for gas phase UED experiment. Figure indicates the vacuum side and air side separated by a 4.5-inch flange. In the vacuum side the tube and nozzle are wrapped by heating tape and aluminum foil. A tube nozzle is shown in the inset.

Figure 4.4 depicts the tube-nozzle system employed in the gas-phase UED experiment. The tube possesses a 0.75-inch diameter and a length of 12 inches. Positioned atop the tube is a nozzle with a 0.25-inch outer diameter and an orifice size of 100μm. The nozzle is connected to the 0.75-inch tube through an adapter and an additional 0.25-inch tube. The overall length of the tube-nozzle system, from the bottom of the flange to the tip of the nozzle, measures 18 inches. On the flange, two pairs of power feedthrough and thermocouple feedthrough are affixed for the purpose of supplying power to heat the tube-nozzle system, which is essential for conducting gas-phase experiments with low vapor pressure samples, and for temperature measurement. Additionally, two copper connectors are positioned near the nozzle's tip and on the 0.75-inch tube to facilitate the connection of the thermocouple probe.

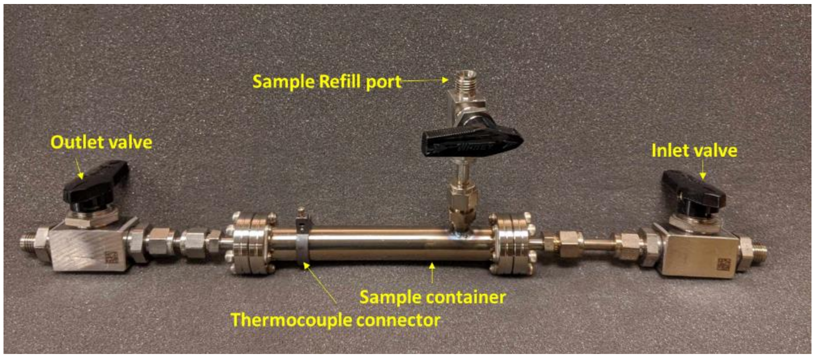

Figure 4.5: Sample reservoir and its various component. Together with the valves, sample container makes a closed system.

Figure 4.5 shows the sample reservoir (SR) where the experimental sample is kept. The SR can contain both liquid and solid samples. The SR is made of stainless steel 1.33-inch flange nipple. It has a cylindrical shape, 6 inches length and 0.645-inch inner diameter, so it has a volume of 32ml. Two valves are located before and after the sample reservoir (SR), enabling the safe detachment of the SR from the SDS by closing the valves and maintaining laboratory safety protocols. The sample can be refilled through a sample refill port, which can be closed using another valve. To measure the temperature on the surface of the SR, a copper connector is placed that can connect a thermocouple wire.

The inlet of the SR is connected to a mass flow controller (MFC) device. The purpose of the MFC is to allow controlled gas flow from its inlet to outlet. There is also a parallel gas line connected from the MFC outlet to the SR outlet. This line is intended to allow the flow of gases like CF_3I or N_2 to the target chamber without passing through the SR. A valve is connected in this line to close it when using only the SR to prevent gas flow through this line. The outlet of SR and the parallel gas line merge using a 0.25-inch Tee connector (Swagelok) and connect with the tube-nozzle assembly using a needle valve. The needle valve is used to reduce the risk of excessive gas entering the target chamber through the gas nozzle. The gas delivery section from MFC to the needle valve is referred to as the backing section. The section before the MFC is called the Mixing section.

The Mixing section consists of three gas tanks: Helium (He), trifluoroiodomethane (CF_3I), and nitrogen (N_2). He is used as a carrier gas to transport low vapor sample molecules from SR to the target chamber through the tube nozzle assembly. CF_3I is used to spatially overlap the gas nozzle, pump laser, electron, and to temporally overlap the pump laser and probe electron beam. Temporal resolution is characterized using the relaxation dynamics of CF_3I. Occasionally, N_2 is used instead of CF_3I for temporal resolution characterization, employing the laser-induced rotational dynamics of N_2 [28], [31], [155]. Both mixing section and backing section can be evacuated using a single stage rotary vane pump (Edwards RV5). All the roughing pumps are connected to a common outlet line to expel the exhaust gas.

4.5 Cold Trap

In this section, I will describe the structure and purpose of the cold trap used inside the target chamber. I will also show temperature vs time plot to characterize the cold trap.

The purpose of the cold trap is to catch and trap the hot exhausted sample molecule and ensure pressure below 1×10^{-4} Torr during experiment. By catching the exhausted molecule, the cold trap also helps to mitigate the electron scattering from molecules other than in the interaction region, hence reduce the background scattering. The cold trap is particularly useful for the sample which has a vapor pressure is low as discussed in section 4.2. When applying heat to the SR and gas line, the warm vapor is ejected from the nozzle, it can be condensed on the target chamber wall which can contaminate the detection chamber as well as the RF cavity. This contamination can in turn result in charge deposition which can cause instability in the electron beam. The cold trap alleviates the problem by actively confining the hot molecule in it.

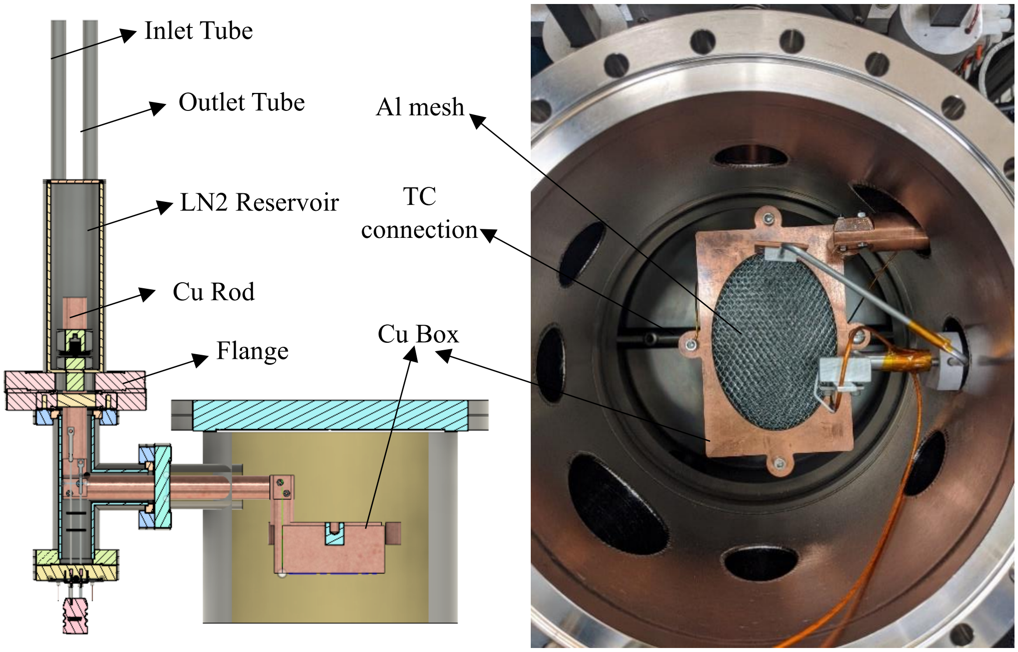

Figure 4.6: sectional View of the Cold trap and its arrangement in the target chamber. A copper rod is submerged into a liquid nitrogen reservoir, which cools the copper box inside the target chamber allowing it to trap the ejected molecule from the gas nozzle. TC: Thermocouple, LN2: Liquid nitrogen.

Figure 4.6 shows the structure of the cold trap as a sectional view to illustrate its position in the target chamber. A stainless-steel cylindrical tube containing 500ml liquid nitrogen (LN2) is mounted on a 4.5-inch stainless steel flange. A 0.75-inch diameter oxygen-free high-conductivity (OFHC) copper rod is introduced into the LN2 reservoir through a Swagelok fitting. This configuration enables direct cooling of a section of the copper rod by immersing it in the LN2, with the cooling effect propagating down the line. By properly machining the end of Cu rods, tight connections are made to maximize the thermal conductivity. Inside the target chamber, a hollow copper box measuring $5'' \times 3'' \times 1.5''$ is attached to the free end of the copper rod and located about 1 inch below the gas nozzle. Multiple layers of honeycomb-structured aluminum mesh are stacked within this copper box, effectively increasing the likelihood that molecules striking the inner walls of the copper box will be retained, preventing their escape from the trap.

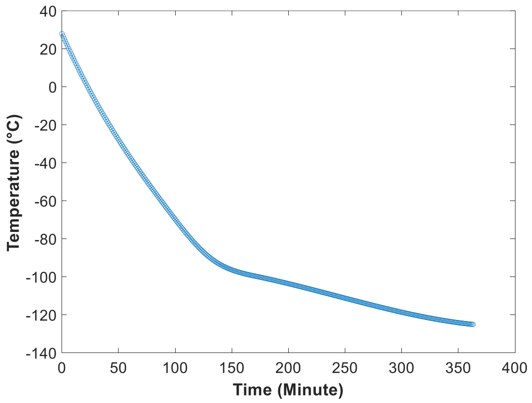

Figure 4.7: Temperature calibration curve for the cold trap. For gas phase UED -70 to -130°C is found appropriate temperature. However, the cold trap can reach -160°C.

The temperature vs. time curve is shown in Figure 4.7 for a typical day's measurement. The temperature of the cold trap is measured by using a K-type thermocouple (TC) probe. One end of the TC probe is connected on the top part of the copper box (shown in Figure 4.6) while the other end of TC leads are connected to a thermocouple feedthrough. Within about one and a half hours of flowing liquid nitrogen, the cold trap temperature reaches -70°C. From our other experimental evidence, at this temperature the cold trap is ready to function properly. The cooling rate of the cold trap depends on how consistently we fill LN2 in the LN2 reservoir. We can monitor the temperature of the LN2 reservoir using another thermocouple probe. If LN2 reservoir is running low or empty, the temp of LN2 reservoir quickly increases, which in turn raises the temperature of the cold trap. We adjust the flow of LN2 to keep the reservoir temperature below -150°C, so that cold trap can reach even lower than -70°C. The minimum temperature of the cold trap was recorded about -156°C.

4.6 Necessary sequence for gas phase UED experiments

This section will describe the general sequence that can be followed while doing gas phase UED experiments using low vapor pressure molecules. The sequence includes preparing the optical setup, wrapping the gas line with heating tape, refilling the sample reservoir, evacuating gas line, pumping out air from sample reservoir, heating the gas line, cooling the cold trap, handling the data acquisition software, allowing the electron beam to the sample chamber, allowing gas to the backing section from mixing section, spatial overlapping of gas nozzle with pump and probe beam, temporal overlapping of pump and probe, introducing the sample in the target chamber, background image acquisition, and appropriately shut down the experiment. Unless otherwise specified, the sequence can be followed immediately after one another.

Figure 4.8 provides a detailed view of the sample delivery system, as presented in the block diagram in Figure 4.3. In Figure 4.8, all components, valves, and connections are depicted through their physical diagrams to enhance clarity. We will refer this figure when describing the sequence of the gas phase experiment.

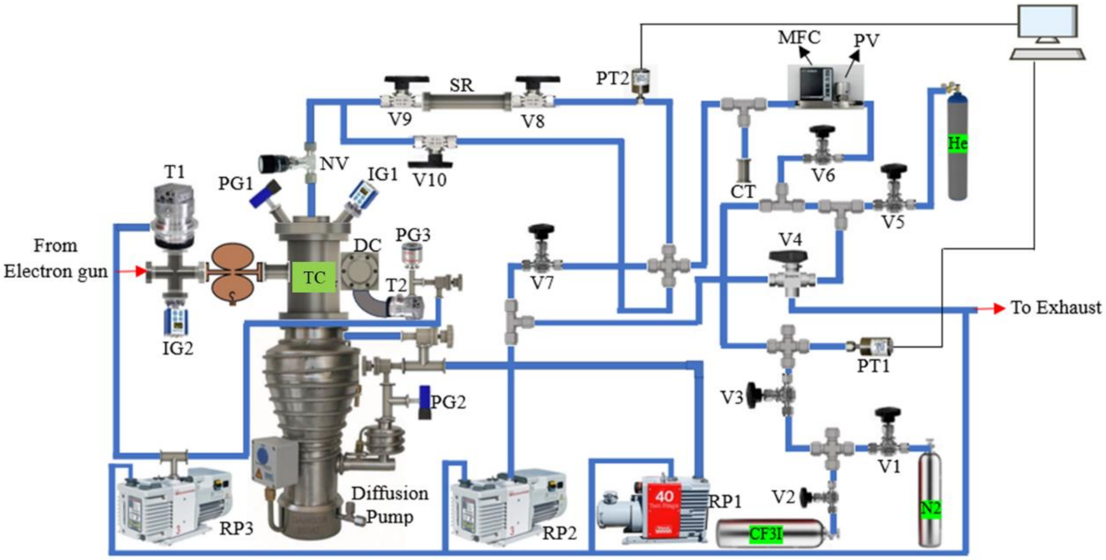

Figure 4.8: Schematic of the sample delivery system for gas phase UED experiment. The complete gas delivery system consists of two sections: the mixing section and the backing section. A mass flow controller separates these sections. The gas phase experiment is conducted by flowing gas from the mixing section to the target chamber via the backing section using several valves and proper sequence. T: Turbo Pump IG: Ion Gauge, PG: Pirani Gauge, TC: Target Chamber, NV: Needle Valve, DC: Detector Chamber, V: Valve, PT: Pressure Transducer, MFC: Mass Flow Controller, PV: Pneumatic Valve, RP: Rotary vane pump.

4.6.1 Preparing optical setup and RF electronics

The experimental procedure starts with turning on the laser, RF system, RF amplifier, and beam-pointing optimization, all power supplies for magnetic lens and deflectors. We need to allow about 30 minutes to warm up the laser oscillator. We then turn on the frequency stabilization program which stabilizes the laser oscillator frequency to the resonant frequency (74.93885MHz) of the RF cavity. Once the resonant frequency is achieved, we send the oscillator output to the photodiode, which sends the signal to the synchronizer. The synchronizer also takes about 30 minutes to stabilize. As a part of optical beam preparation, we turn on beam-pointing optimization program. The program corrects the laser beam pointing using two motorized mirrors and feedback from two CCD cameras[161]. The precise pointing is characterized by the difference in the horizontal and vertical position (DX1, DX2, DY1, DY2) between the center of the beam and center of the crosshair. The difference of the beam center and crosshair should be of the order of 1×10^{-3}.

4.6.2 Filling sample reservoir

We need to fill the sample reservoir with the target sample inside the fume hood. For each process molecule, an appropriate safely handling procedure (SOP) needs to be prepared which needs to be followed. Maintaining the SOP, the sample reservoir is then connected to the gas line.

4.6.3 Wrapping the gas line using heating tape

The sample reservoir (SR) and the gas line from SR down to the tip of nozzle is wrapped by a heating tape (Omega, OMEGALUX STH series). We cover the heating tape wrapping with aluminum foil to prevent loss of heating by convection. For UED experiment using PMCP, we heated the sample at 65°C. We ensured a positive temperature gradient towards the nozzle inside the vacuum target chamber. We probed the temperature at four locations from sample reservoir to tip of the nozzle using K-type thermocouple probe. The nozzle was kept at a temperature of 80°C.

4.6.4 Evacuating the gas line

Before flowing any sample, we need to evacuate the gas line so that there is no air or previously used gas in the line. In Figure 4.8, since mass flow controller (MFC) and a pneumatic valve (PV) isolate the mixing and backing sections, we need to use V4 in ‘Pump’ position to evacuate the mixing section. Similarly, we open V7 to evacuate the backing section.

4.6.5 Evacuating the sample reservoir

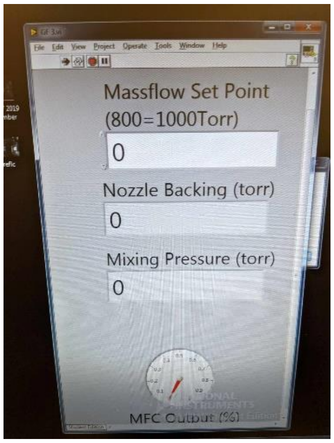

Massflow Set Point (800=1000Torr): 0

Nozzle Backing (torr): 0

Mixing Pressure (torr): 0

Figure 4.9: Gas flow software interface. The pressure of the gas in the mixing section and backing section can be monitored using this interface. The mass flow set point controls the rate of flow of gas from the mixing to the backing section.

Because heating increases the vapor pressure of the sample, we first evacuate the sample reservoir before applying heat to remove any residual air within it. Opening valve V8 allows the sample vapor or air to flow into the evacuated gas line. The pressure increase is monitored by a pressure transducer (PT2), which is connected to a home-built LabVIEW program (GF3) displaying pressure readings in both the mixing and backing sections. Valve V8 remains open until the pressure in the backing section stabilizes. Then, we close V8 and open V7 to evacuate any remaining vapor, reducing the backing pressure to zero. This process is repeated several times until we observe that there is no air left in the reservoir.

This is confirmed when opening V8 no longer results in an increase in pressure in the backing section, indicating that the reservoir is free of air.

4.6.6 Heating the gas line

We apply heat in the gas line using several AC voltage transformers (TDGC2-1KM, TDGC2-2KM). When heating the whole gas line, we ensure that there is a positive gradient of temperature from the sample reservoir up to the nozzle tip so that the hot vapor does not find any cold spot during its travel to the tip. We put a K-type thermocouple probes in various positions on the gas line. We use a Picolog thermocouple data logger (model: TC-08) to simultaneously read the temperature at six different points in the sample delivery system. Increasing the temperature in the nozzle and nozzle tube causes the pressure of the target chamber to rise by a few orders of magnitude, from $\sim 5 \times 10^{-8}$ Torr to $\sim 1 \times 10^{-6}$ Torr. The pressure than stabilizes to $\sim 5 \times 10^{-7}$ after several minutes. To not abruptly increase the system pressure, we slowly increase the temperature to the target temperature, typically at a rate of 1 per minute.

4.6.7 Cooling the cold trap

Simultaneously with the application of heat, we initiate the cooling process of the cold trap. The primary function of the cold trap is to capture the ejected hot molecules from the nozzle, thereby maintaining a stable pressure throughout the experiment. To achieve this, a 230-liter liquid nitrogen tank is connected to the inlet tube of the cold trap via a transport line. By carefully regulating the flow of liquid nitrogen and preventing any overflow, the temperature of the cold trap is significantly reduced. A Kapton insulated vacuum compatible K-type thermocouple (Accu glass product, 30 AWG) is connected to the top of the cold trap box. A bolt presses the hot junction of TC wire firmly against the top surface of the plate in the cold trap, as seen in Figure 4.6b. The other side of the TC wire is connected to the Picolog using a thermocouple feedthrough. Cooling requires a time of about 1.5 hours to go down to -70°C. During UED experiment using PMCP, at this cold trap temperature, we found flowing a total of 100 Torr of PMCP mixed with He in the target chamber did not increase the chamber pressure more than 8×10^{-5} Torr.

4.6.8 Data acquisition software (DAS)

We use a homemade user interface for remotely controlling the equipment's and to monitor the data acquisition conditions[154]. This interface facilitates users to control different parameters remotely as well as safely run the experiment.

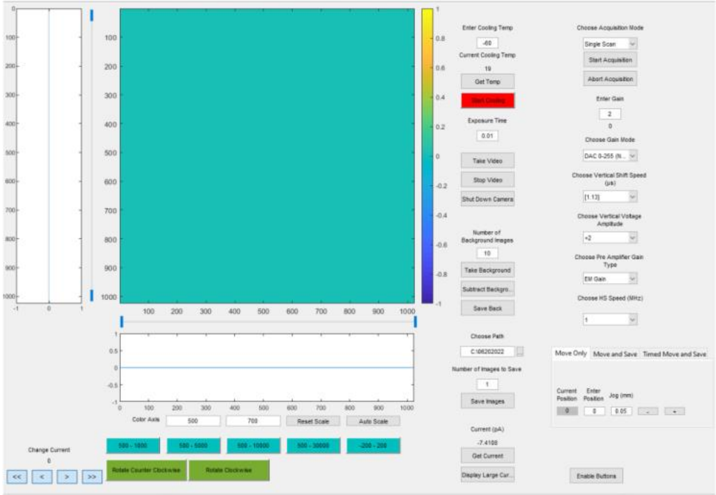

Enter Cooling Temp: -60
Current Cooling Temp: 19
Exposure Time: 0.01
Number of Background Images: 10
Choose Path: C:106202022
Number of Images to Save: 1
Current (pA): -7.4108
Choose Acquisition Mode: Single Scan
Enter Gain: 2
0
Choose Gain Mode: DAC 0-255 (N...
Choose Vertical Shift Speed (µs): [1.13]
Choose Vertical Voltage Amplitude: +2
Choose Pre Amplifier Gain Type: EM Gain
Choose HS Speed (MHz): 1
Current Position: 0
Enter Position: 0
Jog (mm): 0.05
Color Axis: 500 700
Change Current: 0

Figure 4.10: User's interface of the data acquisition software. This software facilitates carrying out the experiment by monitoring and controlling the experimental conditions remotely without being inside the lab. The details of the software are given in ref[154]. The plot is adapted from ref[154].

Figure 4.10 shows the DAS interface. The software is written on the graphical user interface (GUI) in MATLAB. Details about the DAS can be found in Ref([154]). For usual data acquisition, we need to press the 'Start Cooling' button after opening the DAS. This enables the cooling of the EMCCD camera sensor to a stable running temperature of -60°C. The cooling happens in the EMCCD camera sensor using the thermoelectric effect. The temperature of the sensor can be read by pressing the ‘Get Temp’ Button. Once the temperature reaches -60°C, we can use the linear EM gain option from the drop-down menu using the 'Choose Gain Mode' button. The gain for the unblocked electron beam should be 2, and the exposure time should be 0.01s. When changing the exposure time, we always need to stop video acquisition. We use a gain of 300 during the experiment and an exposure time of 10-30 for each scattering image, depending on the total scattering count. The interface is also able to control the delay stage and move it to the desired position to control the pump-probe delay.

4.6.9 Allowing electron beam to the chamber

If the target chamber pressure below 1×10^{-6} Torr and the DAS is ready to use, the valve between the RF cavity and the high voltage chamber can be opened to let the electron beam pass towards the target chamber. This valve is always kept closed to protect the high-voltage chamber from an accidental pressure increase in the target chamber. The electron beam is collimated by a platinum aperture arranged on a copper rack made on a copper plate. The copper plate is mounted on a 2D actuator along with the streak camera and has a pair of notches on each horizontal side. To find the aperture easily, we first find the shadow of the notch on the electron beam seen in the detector. Then the collimator is translated to get the appropriate aperture. The arrangement of the aperture is mapped in the lab-book during the time of mounting those. We can refer to the map to know aperture size. After getting the appropriate aperture, the beam block is put to block the electron beam completely. The beam block is a Faraday cup which is described in Ref [40]. By adjusting the vertical and horizontal position of the collimator, the aperture can be positioned optimally to maximize the number of electrons passing through it, thereby maximizing the current read by the Faraday Cup. The current can be monitored using the DAS. For the PMCP experiment, we employed a 300μm aperture, resulting in an electron beam size of 19.5x18 pixels full width at half maximum (FWHM). Through static analysis of PMCP, we determined that this electron beam size had improved momentum resolution. The electron beam's current without the aperture was measured at -21pA. We found this current is optimum to get good temporal resolution. After implementing the aperture, the current was reduced to -4 pA.

4.6.10 Flowing the gas to the target chamber

After attaining the target temperature of the gas nozzle and cold trap, we can flow gas to the target chamber through the backing section. Before taking data, we need to do the spatial and temporal overlap. We do the overlap using CF_3I, which shows strong scattering signal. To flow CF_3I, we first need to make sure that all the evacuating valves, V4 and V7, are closed. Also, the valve that connects the He cylinder to the Mixing section, V5, needs to be closed. By opening the valve for the CF_3I tank, and opening V2, V3 and V6 we can flow CF_3I in the mixing section. To allow a controlled flow of CF_3I in the backing section and hence to the target chamber, we first open the needle valve, NV, and valve V10. By setting a pressure in the mass flow set point on the GF3 software, a stable flow of CF3I can be introduced into the target chamber. Usually, the mass flow set point can be 0-5000, where the value 800 indicates a pressure 1000Torr is set to flow through the MFC to the backing section. The pressure in the main chamber is read using a hot filament Ion Gauge (Kurt J. Lesker, 354 series). A typical pressure of CF_3I in the backing section 30-50 Torr can result in a good scattering signal for a 100um nozzle. However, for any backing pressure, we should not allow the chamber pressure to go above 1×10^{-4} Torr.

4.6.11 Spatial overlapping the gas, electron and laser beam

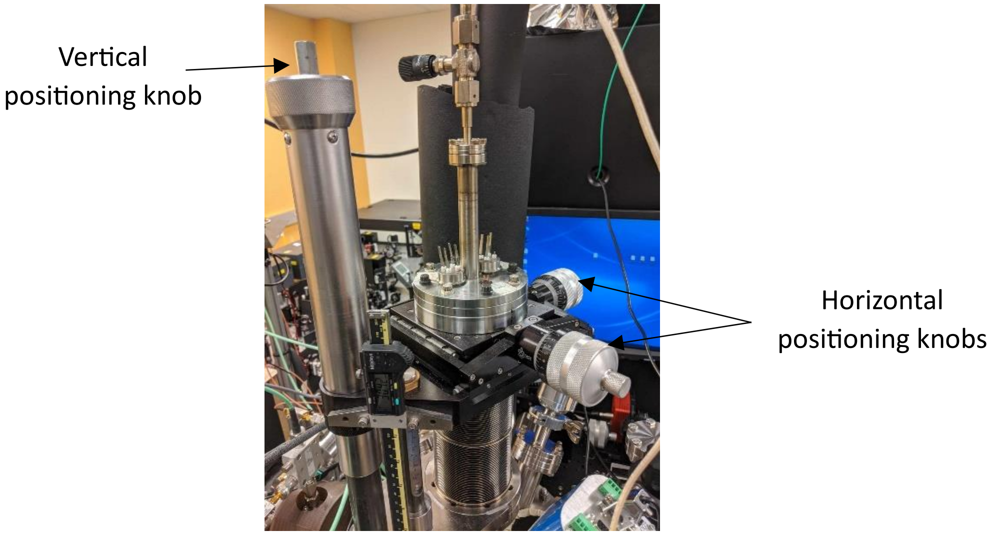

Figure 4.11: 3D actuating stage. The vertical column is used to position the nozzle vertically in the path of the electron beam. The horizontal positioning knobs are used to achieve spatial overlap among the electron beam, pump laser beam, and gas jet.

The spatial overlapping among the gas, electron beam and pump laser beam is done by first optimizing the position of the gas nozzle on electron beam by maximizing the scattering, and then by horizontally moving the pump beam on the gas jet. Figure 4.11 shows a 3D actuator stage, located on the target chamber. The purpose of the stage is to align the nozzle with respect to the electron beam and laser position. The vertical adjustment of the nozzle requires that the electron beam is not blocked by the nozzle, while at the same time the scattering is maximized. If the nozzle is far away from the electron beam, the total scattering count and scattering intensity is decreased. On the other hand, if the nozzle is lowered more and the nozzle blocks the electron beam, we can see a decrease in current displayed in the DAS. Also, a scattering is seen at the bottom of the phosphor screen because of scattering of electron beam from the nozzle tip. The optimum vertical position of the nozzle can be found by ensuring a circularly symmetric scattering pattern with maximum brightness.

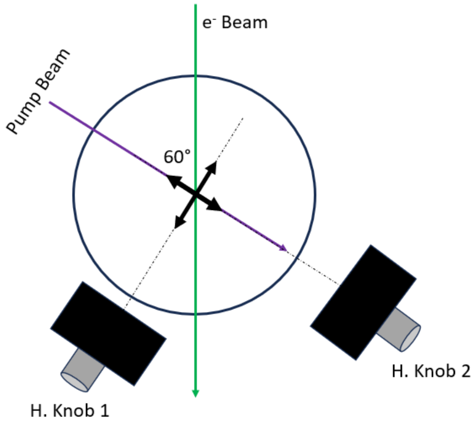

Figure 4.12: Schematic of the horizontal knob position with respect to electron beam and laser beam propagation direction. Horizontal knob 1 (H. Knob 1) moves the nozzle perpendicular to the laser path, whereas Horizontal knob 2 (H. Knob 2) moves the nozzle along the laser path.

After adjusting the vertical position, we need to optimize the horizontal position of the nozzle. To minimize the velocity mismatch, we use the laser front tilting technique, which requires the pump beam to intersect the gas at an angle of about 60° with respect to the electron propagation direction. The stage is placed so that the nozzle can be moved perpendicular to the pump beam path by moving horizontal adjustment knob 1 (H. knob 1 in Figure 4.12). On the other hand, turning the horizontal adjustment knob 2 (H. knob 2) moves the nozzle along the laser path. For a displacement of dx along the laser path, by turning H. knob 2, the displacement perpendicular to the electron beam path is

$dx \times sin60° = \frac{\sqrt{3}}{2}dx$. We first spatially overlap the gas nozzle on the electron beam by maximizing the scattering by turning H. Knob 2. This fixes the nozzle position on the electron beam. An overlap between the pump beam and gas nozzle can be ensured using laser induced fluorescence technique. In laser induced fluorescence, by absorbing laser light molecule is excited to higher energy level and then return to the ground state by spontaneous emission. The emission is viewed as white light on a CMOS camera. In the spatial overlapping between pump laser and gas nozzle, fluorescence is maximized by steering the pump laser using the mirrors just before the target chamber. This in turn does the overlap of gas nozzle and pump beam with the electron beam.

4.6.12 Temporal overlapping

The method we use for the temporal overlap is called the plasma-lensing method, which is described in Ref [40], [155]. The vertical position of the laser pump on the gas is also adjusted by seeing the plasma. The plasma lensing method can give us a coarse time zero with an accuracy of about one picosecond [160]. The fine time zero is obtained by using time dependent data of CF_3I which we will discuss in section 4.8.

4.6.13 Introducing the sample

After doing the spatial and temporal overlap and getting time zero, the system is ready to take data with the actual sample. Below are the steps to follow to introduce the sample:

- Before switching the sample, the mass flow set point is set to zero, and PV is turned off.
- The valve on the tank of CF_3I is also closed to stop the supply of CF_3I.

- Using valves V7 and V4, both the backing and mixing sections are pumped out again.
- V5 is opened to allow He to flow in the mixing section.
- Using the MFC and PV, about 100 Torr of He is flown to the target chamber for about 15-20 minutes, which flashes the residual CF_3I from the chamber and leaves it ready for the actual experiment.
- After this, V10 is closed, and V8 and V9 are opened. The He is then directed through the sample reservoir, which drives the PMCP vapor to the sample chamber.
- At this point, we should closely monitor the target chamber pressure. The backing pressure of the diffusion pump is measured by a Pirani gauge, and the pressure is labelled as ‘Diffstak’ on a vacuum gauge controller (Granville-Phillip 316). We need to check both the chamber pressure and Diffstak to see if they increase abruptly.
- In addition, we also need to monitor the high-voltage chamber pressure continuously. For a high-voltage chamber pressure of above 1×10^{-6} Torr, we should close the valve between the high-voltage chamber and RF cavity.

4.6.14 Taking scattering data with sample

The scattering data for the target molecule is captured using the DAS. We employ an EM gain of 300 for the diffraction image and configure the color axis scale for the detector on the DAS as '500-30000'. This configuration allows us to effectively monitor the diffraction image. To ensure optimal image quality, we set the exposure time in a manner that ensures a bright ring is visible around the beam block on the detector without causing saturation. For PMCP experiments, the exposure time was set to 30 seconds. Depending on the type of diffraction data, whether static or time-resolved, we can select the desired stage position on the DAS. The DAS also enables us to perform scans, either by moving the stage continuously in one direction or by employing a back-and-forth scanning method.

4.6.15 Background image acquisition

Before or after taking the scattering image with the sample, a few scattering images are taken by turning off gas delivery. This is done by setting the MFC setpoint to zero and turning off the PV. Then, the target chamber and gas lines are evacuated by opening V7 and V10 while keeping the valves V8 and V9 closed. Then the scattering images are taken using the same gain and exposure. The background image carries a great significance for our lab. The scattering image with sample contains laser reflection from various interior parts in the target chamber, ambient light, and saturated pixels. This causes the images to no longer be circularly symmetric. By subtracting the background image, these issues can be resolved.

4.6.16 After the experiment

The gas phase UED experiment with samples of low vapor pressure requires special attention when the data acquisition is over. This is necessary to protect valuable apparatus components like the RF cavity, phosphor screen, turbo pumps, and diffusion pumps from being contaminated. It is seen that when the cold trap temperature starts to rise after stopping the supply of LN2, the pressure at the target chamber starts to increase after a certain temperature, typically above -100°C. To handle this increase of pressure, we need to stop the experiment tactically following the steps:

- First, we need to close the valve between the high voltage chamber and RF cavity, NV, and press stop cooling on the DAS. Since we no longer need the electron beam and pump beam, we can turn off the laser system, RF synchronization, and electronics following standard operating procedures.
- All the heating supplies need to be stopped, as well as stopping the flow of liquid nitrogen. It takes several minutes for the cold trap to react once the liquid nitrogen supply is stopped. After that, the temperature starts to rise slowly.
- As the cold trap gets warmer, the trapped molecules evaporate from the cold trap, which increases the target chamber pressure that both ion gauge and diffstak can reflect.
- If the diffstak pressure is reaching 50mTorr, we need to close the pneumatic isolation valve of the diffusion pump so as not to stall the diffusion pump from the excess entrance of the gas molecules.
- After closing the isolation valve, the target chamber pressure increases even more rapidly. If the target chamber pressure increases to 1mTorr, we turn off both the turbo pumps. The turbo pump is not designed as baking pump, and it usually works below 1mTorr.
- By the time the rotating blades in the turbo pump comes to a complete stop, the target chamber pressure increases to the order of 10^{-2} Torr. If the gas molecules are not quickly expelled from the chamber, it is highly likely that the gas molecules will stick on the chamber wall and contaminate other apparatuses.
- We close all the backing valves for the turbo pumps and flow about 1 Torr of He in the chamber. Since the backing pumps have lower pumping speed (about 3 litre/s),

we installed another roughing pump (RP) (Agilent ds 602 dual-phase pump), which has 7 litre/s speed. This pump is connected under the detection chamber using a 4.5inch Tee connector (not shown in Figure 4.3), with T2 in another branch.

- We ensure that the valve of the backing pump for the turbo pumps is closed before opening the valve to release excess pressure caused by the mixture of helium and gas using RP.
- The RP cannot lower the pressure too much and after a while pressure starts to increase again. Therefore, we need to repeat this flushing process using He many times.
- Once the pressure is below 2.5×10^{-2} Torr and it does not increase anymore, we can close the valve for the RP and open the valves for the backing pumps of the turbo pumps followed by turning on the Turbo pumps.
- Once the pressure of the chamber is below 1×10^{-3} Torr, we can open the isolation valve. Initially, the backing pressure in the diffstak looks elevated, around 50mTorr. If it begins decreasing after a few minutes, we can leave the isolation valve open.

4.7 Sudden pressure rise

We experienced that the pressure in the main chamber increases more than 1×10^{-4} Torr during the time of data acquision due to dipping of liquid sample in the chamber or burning the heating tape in vacuum. If this happens following steps should be followed immediately after noticing the pressure rise:

- Close the valve between high voltage chamber and RF cavity.
- Close the isolation valve between the target chamber and diffusion pump.
- Close the needle valve.

- ❖ Block the laser output from the laser amplifier.
- ❖ If the target pressure is above 1×10^{-3} Torr, turn off the Turbo pumps connected with the detector chamber and RF cavity.

Subsequently, the laser, RF amplifier, RF electronics, magnetic coil, and deflector power supplies should be switched off. Once the cause of the sudden pressure rise has been thoroughly addressed through troubleshooting, the experiment can be resumed.

4.8 Time zero and instrumental time resolution measurements

In our KeV-UED setup, we measured the instrument response function (temporal resolution of the system) using CF_3I [155]. Prior to collecting time-resolved data for the current thesis, where the process sample is PMCP, we conducted several data scans using CF_3I to evaluate the system's temporal resolution and to ensure spatial and temporal overlap. Figure 4.13 presents the 2D $\frac{dI}{I}$ data for CF_3I, along with the time-dependent lineout averaged in the range of $s = 1.6 - 2.1 Å^{-1}$. We combined all the CF_3I data and measured the temporal resolution following a methodology similar to that employed by Xiong et al. during their experiment[155].

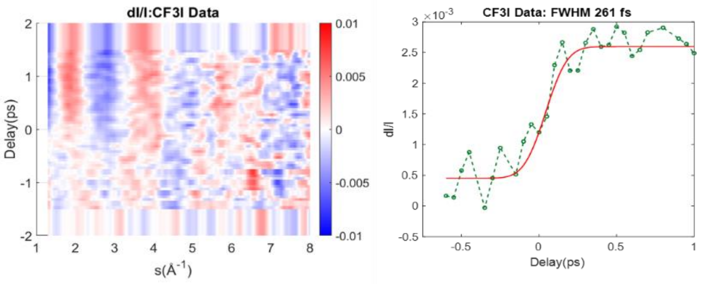

Figure 4.13: Time dependent difference-diffraction signal for CF3I. The average of the signal in $s = 1.6 - 2.1 Å^{-1}$ is averaged and fitted by an error function, which gives both the time-zero position and instrument response time of our diffraction set up.

Figure 4.13 shows the 2D $\frac{dI}{I}$ for CF_3I, where the horizontal axis shows the momentum transform vector, s, and the vertical axis shows the delay between the UV pump and electron probe. We fit an error function of model $y = a \times \mathrm{erf}\left(-\frac{\frac{(x-b)}{c}}{\sqrt{2log2}} \times \sqrt{2}\right) + d,$ as given by equation (2.10), to the feature averaged in $s = 1.6 - 2.1\text{Å}^{-1}$, and found a temporal resolution is about 260fs. The parameter, b, in this model, gives the time zero for the experiment, and c gives the rise time in FWHM. This rise time is attributed as the instrument response time or temporal resolution of the setup.

4.9 Summary

The chapter discussed the instrumentation of our KeV-UED lab, and detailed procedure for conducting gas phase UED experiments using low vapor-pressure sample. The above-mentioned procedure was followed during the gas phase UED experiment using PMCP. Proper attention needs to be given during experiments to prolong the instrument's lifetime, at the same time, to obtain good quality of data.

Chapter 5

Photodynamics of Methylated Cyclopentadiene Studied by Ultrafast Electron Diffraction

5.1 Preface

In this chapter, I will discuss the UV-induced dynamics of 1, 2, 3, 4, 5 pentamethylcyclopentadiene (PMCP) probed using our KeV-UED setup. The necessary experimental details are discussed in the previous chapter. Here, I will first introduce PMCP and deduce the scientific importance of studying the photodynamics of PMCP. Later, I will state the research goals. I will outline the data analysis routine for KeV-UED experiment since the analysis differs from the analysis of MeV-UED data. In the Result and Discussions section, I will present my analysis of static and time-resolved data. Since we do not have the simulation to interpret the data in-depth, I will just describe the primary interpretation of the data.

5.2 Introduction

Photo dynamics of cyclic organic molecules are of immense interest as they are directly involved in many natural biological systems, solar energy resources, drug molecular design, and synthetic chemistry. Organic ring molecules like polyenes participate in numerous numbers of light-induced reactions. The contribution of the polyenes can be found in the vision mechanism of human eyes due to photoisomerization[73], [162], [163], energy harvesting due to their rich photo physics[164], [165], etc. Understanding the photodynamics of these ring systems and the interconversion between various numbered-membered ring systems is important for their implication in photophysics, photochemistry, and photobiology. Investigating photodynamics in smaller molecules is convenient because they have fewer degrees of freedom, which makes the interpretation easier. Additionally, if theoretical study is required, studying smaller polyenes greatly reduces the simulation cost. The interpretation of the dynamics found experimentally and theoretically can then be projected toward investigating the dynamics of larger polyenes, which have higher relevant degrees of freedom.

Cyclopentadiene (CP) is a prototype molecule that is known to display electrocyclic ring closure reaction to generate highly strained ring molecules bicyclo [2.1.0] pent-2-ene (BP) and tricyclo [2.1.0.02,5] pentane (TP) in addition to the product due to sigmatropic transfer of H atom[166][167]. The photo excitation leads the CP to go to $1B_2$ state from where it moves to $2A_1$ state. At the CI the wave packet bifurcates. One photochemical pathway leads to the formation of both BP and TP through one conical intersection (CI), while another pathway moves to another CI and results in the creation of the CP molecule by repositioning the double bond. The end-products from photoreaction have significant importance in synthetic applications and other experimental procedures. In an experimental study on liquid phase CP, the product yield ratio was 14:7:1 for CP:BP:TP[166].

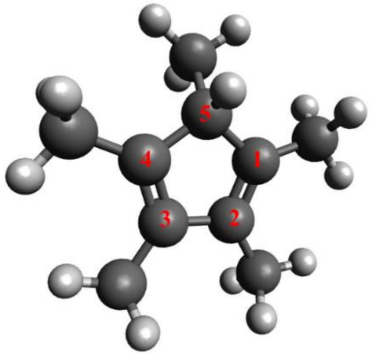

Figure 5.1: Ground state structure of PMCP. The carbon atoms in the ring is labelled for identification in the text. The labelling is done based on the description in Ref[69].

1, 2, 3, 4, 5-pentamethyl cyclopentadiene (PMCP) is a methylated sister molecule of Cyclopentadiene (CP). The structure of PMCP is shown in Figure 5.1. It is well established that the dynamics of polyenes with an added substituent of larger mass is slowed down than the unsubstituted polyene's dynamics [69][168][169][170]. Similarly, slower dynamics happened in PMCP compared to the dynamics of CP[69]. The dynamics are slowed down due to added mass and inertia in the 5th position in the ring of CP. Schalk et al.[69] demonstrated that the dynamics at CI is governed by specific vibrational mode. They showed that adding substituent in the 5th carbon position changes the symmetry of the molecule. An out-of-plane motion of the 5th carbon in the CP controls the time to arrive at the CI located at the excited state/ground state intersection. With added substituent in this position, the out-of-plane motion is slowed down, consequently slowing the overall dynamics[69]. This study aims to capture the structural dynamics during the transition to the ground state from the excited state.

For gas phase PMCP, the end product nature and ratio is still ambiguous[69], [171]. Utilizing the structure sensitive UED technique, our objective is to investigate whether highly strained products, similar to BP or TP, are formed as a result of the photoreaction of PMCP. Furthermore, we will examine the evolution of the ring structure of PMCP over time. Our aim is to determine the timescale of the relevant dynamics and the formation of products.

5.3 Research goal

In this section, we establish our goal to conduct this experiment. In a previous study, Rudakov et al. analyzed the photo-induced chemistry of PMCP after excitation with 267nm photon and probed it using photoionization spectroscopy[172]. PMCP was excited to $1B_2$

state and then it underwent subsequent relaxation to the $2A_1$ state, and then $2A_1$ state to $1A_1$ ground state. Although the excitation energy was higher than the energy required for ring opening of PMCP, they found that PMCP reverts to its original structure after relaxing back to the ground state. There was no sign of ring opening and isomerization at the picosecond time scale after photoexcitation. They concluded that because of the added methyl group in PMCP, the laser excitation energy is distributed to all of these vibrational coordinates and hence it does not cause any structural change. Based on their observation, we aim to employ UED to structurally resolve the dynamics at different stages of photoreaction. We aim to probe the motion along different degrees of freedom in the molecule and subsequent evolution in the structure of PMCP.

In another study, Rudakov et al. studied the UV dynamics of PMCP by exciting with 267nm photon and probed the dynamics implementing time-resolved photoelectron spectroscopy (TRPES) and mass spectroscopy[171]. They did not find any evidence from their observation that PMCP isomerizes due to photochemistry. By analyzing the time dependent mass spectrum, they found that the initial population in $1B_2$ state decayed to $2A_1$ state in $\tau_1 = 183fs$ subsequently decayed to $1A_1$ state in $\tau_2 = 60fs$.

Schalk et al.[69]. conducted a TRPES study on various cyclopentadiene-derivative molecules, including PMCP. They excited the ground state of PMCP using four different photon wavelengths: 240nm, 250nm, 258nm, 278nm. They found that the time required to relax from the $1B_2$ state to $2A_1$ (τ_1), and from the $2A_1$ state to $1A_1$(τ_2) is independent of excitation wavelength. They reported $\tau_1 = 71, 79, 72, 50$fs and $\tau_2 = 127, 123, 133, 195$fs for the four excitation wavelengths, respectively. Additionally, they introduced another time constant, τ_3 , which improved the fitting of their experimental data and falls in the range of 700-710fs. These time constants somewhat align with those calculated by Fuss et al.[173] for CP: τ_1=37fs and τ_2 =71fs, along with τ_3=333fs, corresponding to CP isomerization to BP and TP. Schalk et al. explained the increase in τ_2 by studying the effect of adding a methyl group to CP. The same reason can be applied for the elevation of τ_3 for the case of PMCP. However, the time constants revealed by Rudakov et al.[171] significantly contrast with those found by Schalk et al[69].

With this time resolution. In this work, our goal is to investigate the structural changes in PMCP as it relaxes to its ground state, as well as its structural evolution in the ground state. We will also study if any backreaction happens in a picosecond time regime. Employing structure sensitive UED, we aim to find if any isomerization happens after photoexcitation of PMCP. If this occurs, we focus on determining the timescale of this. We aim to determine if any dynamics occur that might take around 700fs, as suggested by Schalk et al[69]. The temporal resolution of KeV-UED in our lab is about 240fs[31], [155]. While our system's time resolution may not be sufficient to resolve the ongoing debate about various time constants in the dynamics mentioned earlier, we believe that using UED will provide a unique perspective on understanding the photodynamics of PMCP due to UED's sensitivity to charge distribution and spatiotemporal resolution. In addition, we are studying UV-induced dynamics of cyclopentadiene (CP) and tetramethyl cyclopentadiene using a gas-phase MeV-UED setup. The combination of these MeV-UED and KeV-UED experiments will contribute to a comprehensive understanding of the photodynamics of CP and its derivatives. We aim to study how the dynamics varies because of the addition of methyl group with CP. Employing UED our objective is to determine the end product and their relative ratio at the end pf dynamics.

5.4 Experimental Details

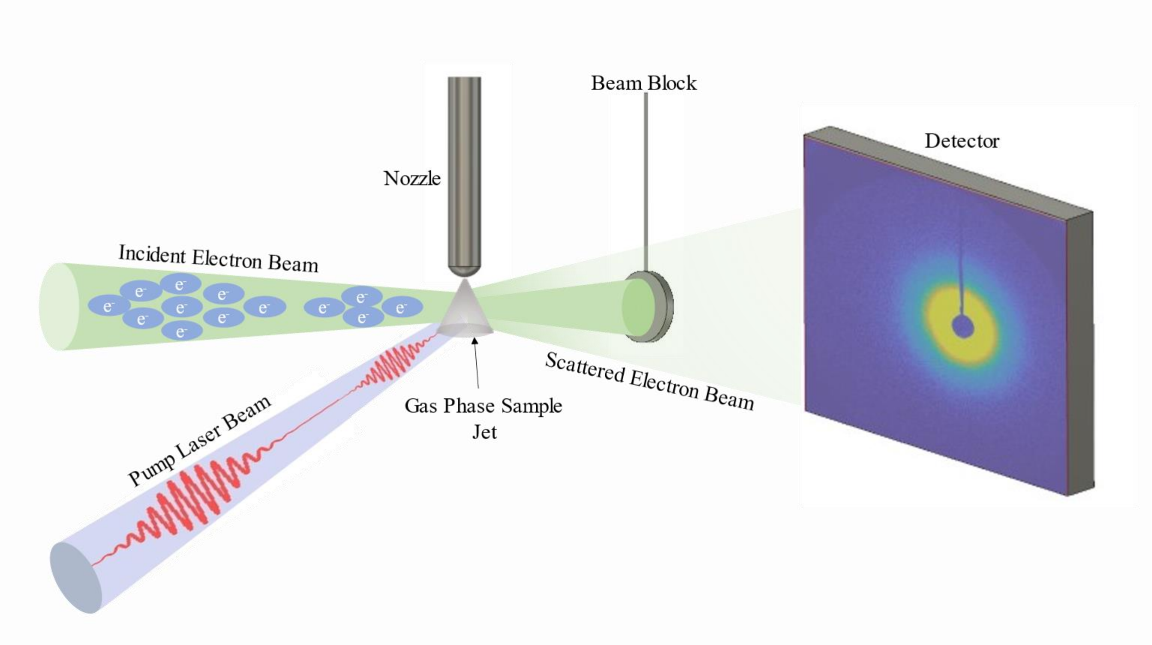

Figure 5.2: Schematic diagram of the interaction of the gas phase sample with KeV electron pulse and femtosecond UV pulse. The un-scattered electron beam is blocked by the beam block. The scattering electrons are recorded by a phosphor screen-EMCCD detector system.

The details of this experiment and experimental setup was discussed in chapter 4 and in previous reports[34], [40], [155]. Briefly, a Ti:Sapphire laser system generates laser pulses with a central wavelength of 800nm and a 30 fs pulse duration. The laser system output produces IR pulses at a repetition rate of 1KHz, each pulse carrying 7mJ of energy. A portion of the IR output is directed to a third harmonic generator, producing a 267nm pulse used to initiate photoemission from a photocathode. The emitted electrons are accelerated to a kinetic energy of 90KeV and guided to the sample chamber by magnetic deflectors, and transversely compressed by magnetic lenses. For longitudinal compression, negative velocity chirp is applied using an RF field in a cavity, resulting in pulse compression at the target position.

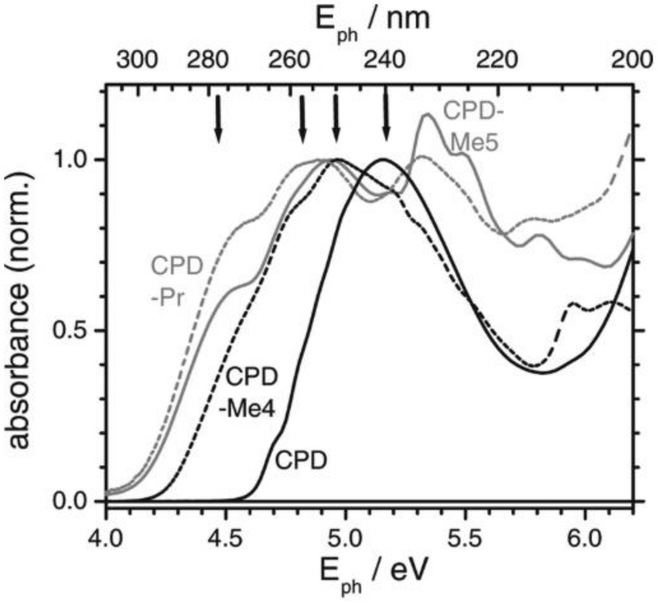

Figure 5.3: Normalized absorbance of Cyclopentadiene (CPD), 1,2,3,4 Tetramethyl Cyclopentadiene (CPD-Me4), 1,2,3,4,5 Pentamethyl Cyclopentadiene(CPD-Me5) and 1,2,3,4-tetramethyl-5-propylcyclopentadiene (CPD-Pr). Figure is adapted from Ref[69] with permission from ACS[6]. For our experiment, we only focus on 1,2,3,4,5 Pentamethyl Cyclopentadiene (CPD-Me5), which we abbreviated as PMCP. The absorbance of PMCP is indicated by the gray solid line, and the wavelength is found from the horizontal axis on top of the plot. For the case of PMCP, the maximum absorbance happens around 255nm pump wavelength.

Figure 5.3 shows the normalized absorbance of cyclopentadiene and its three-derivative including PMCP. Although PMCP shows a sharp peak at ~235nm, there is another peak that arises at 255nm. We decided to pump PMCP at 267nm since the absorbance at this wavelength is appreciable, and we can generate UV of 267nm from another portion of the laser output which is sent to a second third harmonic generator that generates a 267nm pump pulse. To minimize the velocity mismatch between the electron and laser pulses, we

---

[6] The figure is adapted from Ref [69] and can be found, https://pubs.acs.org/doi/10.1021/jp911286s. Further permissions related to the material excerpted should be directed to the ACS.

employed the pulse front tilting technique. The pump laser and probe electron traverse the sample molecule at a 60° angle. PMCP, purchased from Fisher Scientific with a 93% purity, was used without further purification. We maintained the sample reservoir at 65°C-70°C and the entire gas line at 75-80°C to prevent clogging. We took 7ml of PMCP in the sample container during the experiment. Using 7 ml of PMCP we were able to take 12 hours of data. When taking data on another day, we refilled the container by dumping out the left-over sample and refilling with new sample. An IR spectroscopy of PMCP ensured thermal stability up to 90°C (Jackson Lederer helped in performing IR spectroscopy). The PMCP vapor was introduced into the interaction region using a tube nozzle with a conical orifice with a minimum diameter of 100μm. The PMCP vapor was carried by He with a total backing pressure of 100Torr. For pump-probe data, we utilized pump energies ranging from 35-110μJ per pulse to take the pump power dependent data and used 75mW pump power to take scans from -5ps to 10ps. The electron pulse contained 25,000 electrons per pulse. The interaction between PMCP, electron, and laser pulses was recorded on a phosphor screen which is imaged by an EMCCD camera. A homemade synchronizer enhanced temporal resolution by precisely timing the arrival of the electron pulse and RF field in the cavity, amplifying the RF signal. The system's temporal resolution was measured 260fs using the relaxation dynamics of CF_3I. We took about 50 images at each delay stage, with 30 second exposure time for each image. During each scan we allow the delay stage to move in a back-and-forth motion 2-5 times.

5.5 Data analysis routine

In this section I outline the data analysis procedure, which is different for the case of KeV-UED diffraction data in some cases. The image obtained from the detector had some artifacts due to saturated pixels, ambient light, or the reflection of the laser to the phosphor screen. These artifacts were removed by following specific steps.

- During the experiment, five backgrounds diffraction images were captured using the same exposure time and gain of the as of the gas diffraction image but without flowing any sample or carrier gas. The background images were averaged and subtracted from each gas diffraction image to remove any effect from ambient light or laser reflection.

  For the case of MeV-UED, the background is taken with electron beam and gas jet off. For our case, we acquire background image by stopping the gas flow.
- A threshold was applied, usually double the mean intensity at the lowest *s* signal, above which all the pixels were set as not a number (nan) to remove all the hot and saturated pixels.
- The beam stop, and its holding wire, as shown in Figure 5.2, can alter the azimuthal average of the diffraction signal, so we put a mask on these to set their value as nan. In the MeV-UED setup, the un-scattered beam passes through a hole at the center of the phosphor screen. We need to mask the hole and its shadow during the data analysis.
- The corner of the detector, where the phosphor screen is not imaged, was also masked to set a nan value.
- We averaged all the diffraction images, and we determined a common center of the average image.

- We take the azimuthal average over all the pixels located at the same radial distance from the diffraction center and ignore any pixel 3 standard deviations more or less than the average.
- We averaged all the diffraction images for each delay point and applied a median filter of window size of 5x5. The median filter removed any grainy noise. Before applying median filter, we replace all pixels with NAN value by their corresponding azimuthal average.
- We calculated the diffraction center for each delay point from the filtered image. We calculate the average diffraction center by taking the mean center over all delay stages.
- We remove time-zero drifting in diffraction data using the following steps. We took data for several days. Each day we took data in several (typically 2-3) scans. We first split the total data of each scan into two or three groups in lab time, so that each group has four diffraction images at each delay stage. We then averaged the images and calculated $\frac{dI}{I}$. We took a time dependent lineout by averaging $\frac{dI}{I}$ at $2.3 < s < 3.3\text{Å}^{-1}$. We fit the lineout using the equation (2.10), where b gives the center of the error function for the data group.
- We follow the same procedure for all the data sets. Then we averaged the data groups based on time zero.

5.6 Results and discussions

In this section, we delve into the core findings of our research. We will first present the static data analysis to extract ground state information of PMCP. Following that, we will discuss the pump-power dependence of the scattering signal. From the power analysis, we chose the correct power to take the long scan with smaller time steps. After that, we will be discussing the time resolved long scan in term of $\frac{dI}{I}, \Delta sM, \Delta PDF$.

5.6.1 Static data analysis

We will focus on the static data in this section. As discussed before, static data gives us the information about the internuclear distance of the molecule at the ground state, facilitates determining the $pixel - s$ calibration value, finding the spatial resolution. Here, we will show how using the sM analysis we optimized the electron beam size on the detector to improve the spatial resolution.

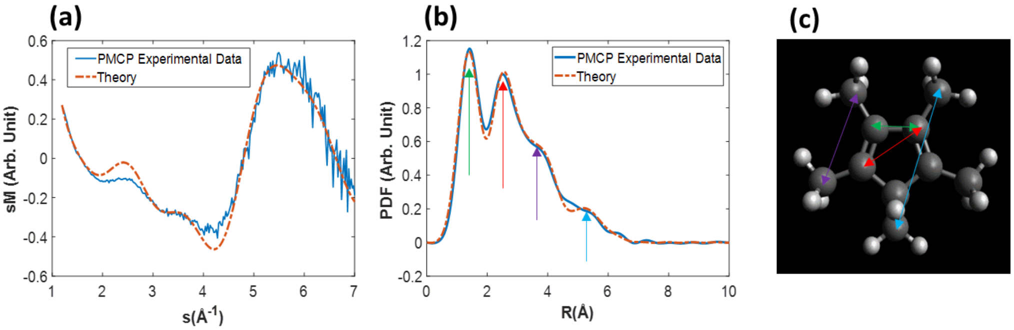

Figure 5.4: Static data analysis of PMCP. (a) Modified scattering intensity obtained from experimental data (blue curve) and theory (red curve). The theoretical scattering intensity is calculated from the optimized PMCP structure. The experimental data agrees nicely with the theory in terms of the position of the peaks and valleys. (b) The pair distribution function (PDF) for both experimental data and simulation agrees very well for all major peaks. (c) 3D structure of PMCP. Various interatomic distances appeared in the PDF. Colored arrows are used to match the relevant interatomic distances in PDF and structure.

Figure 5.4 shows the experimental and theoretical modified scattering intensity and pair distribution function for the ground state PMCP shown in Figure 5.4c. The ground state PMCP was optimized in ORCA using B3LYP/def2-SV(P) basis set. The experimental sM

was calculated using the zero-fitting method discussed in section 3.2.3. In the sM, we can see a very good match between the theory and experiment; all the peaks and troughs are located at the same s. The experimental sM can produce an oscillation at around $s = 3Å^{-1}$ like the theoretical sM, even though there is no zero crossing at a proximity.

We transversely focused the electron beam on the detector using magnetic lens. The beam size was $0.47Å^{-1} \times 0.43Å^{-1}$ FWHM. Initially, the beam size was bigger, $0.69Å^{-1} \times 0.78Å^{-1}$ FWHM on the detector. The focused electron beam has reduced transverse momentum spread. The transverse coherence length is expressed as $L_x \approx \hbar/\sigma_{p_x}$ [21][174], where, $\sigma_{p_x}$is the transverse momentum spread. Focusing the beam suppress the σ_{p_x}, enhances the transverse coherence length, consequently, improve the spatial resolution[21]. The sM, which we calculated for the bigger electron beam, did not show this oscillation for the poor momentum resolution.

Figure 5.4b shows the pair distribution function (PDF) for the ground state PMCP. All the prominent peaks demonstrate a good agreement with the theory, as shown by the red line. The peaks at 1.42Å and 2.51Å indicate the nearest C-C and second nearest C-C distance in the ring, as indicated by the colored arrows and shown in Figure 5.4c. Also, a shoulder appeared at 3.84Å, which indicates the C-C distance of the two neighboring methyl groups. A minor peak can also be seen at 5.36 Å, the furthest C-C distance in PMCP.

5.6.2 Power scan analysis

We took data upon interaction with pump lasers of different powers to determine which power has very good signal-to-noise ratio, and if any multiphoton excitation happens for that pump power. In case of single photon excitation, $\frac{dI}{I}$ depends linearly on the pump laser power. However, multiphoton process is a non-linear process, so the $\frac{dI}{I}$ does not show a linear behavior with pump power. We took pump-probe data for four different UV pump powers, namely 35mW, 60mW, 85mW and 110mW. This corresponds to fluence of 75, 130, 185, and 242mJ/cm^2, and peak intensity 0.6, 1, 1.40, and 1.9 TW/cm^2. We took a 2-point scan, where we took data at one point, which is way before time zero, and another point, which is 5ps later than the time zero, so that we can calculate $\frac{dI}{I}$.

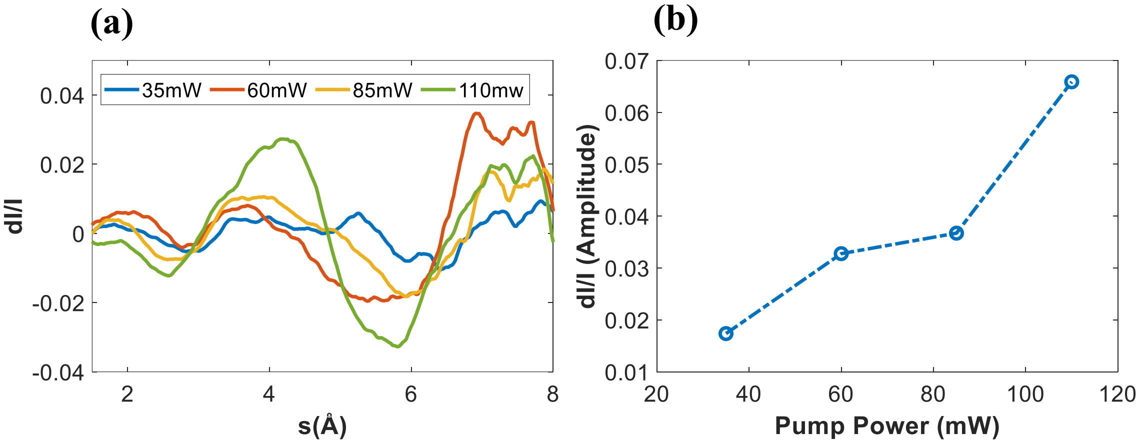

Figure 5.5: Power scan analysis for PMCP. (a) UED data was taken by using four different pump energy. The dI/I signal at different energies are overlayed to see the relative signal growth. (b) Growth of amplitude as a function of pump power. The trend is almost linear.

We calculated the $\frac{dI}{I}$ from these two pints scans, which is shown in Figure 5.5a. The amplitude grows with increasing power, although the amplitude of the 60mW pump is higher than others at $s = \sim 7\text{Å}^{-1}$, which is most probably due to an artifact. To see the relation of the amplitudes with different pump powers we calculated sum of $\frac{dI}{I}$ using the following formula,

$$\frac{dI}{I}(Amplitude) = \sum \frac{dI}{I}(Peaks) - \sum \frac{dI}{I}(Valleys). \tag{5.1}$$

For the $\frac{dI}{I}$ of each pump power, we summed $\frac{dI}{I}$ at the peaks at $s = \sim 2\text{Å}^{-1}$ and $s = \sim 3.75\text{Å}^{-1}$, and valleys at $= \sim 2.75\text{Å}^{-1}$ and $s = \sim 5.5\text{Å}^{-1}$. Subsequently, we subtracted the sum of $\frac{dI}{I}$ found in the valleys from the sum of the $\frac{dI}{I}$ found in the peaks. The relation of $\frac{dI}{I}$ (Amplitude) vs. pump power is shown in Figure 5.5b. For one-photon excitation, the amplitude would increase linearly. For multiphoton excitation the amplitude would increase rather rapidly with the increase of pump power. From Figure 5.5b, the first three data points, $\frac{dI}{I}$ at 35mW, 60mW and 85mW, shows a linear behavior with pump power to some extent; however, if we compare the $\frac{dI}{I}$ at 110mW with the other data points, it looks the $\frac{dI}{I}$ increases rapidly compared to the other data points. In a different perspective, $\frac{dI}{I}$ at 35mW, 60mW, and 110mW constitute a good linear relation with pump power. We chose to use 75mW for further time-resolved data acquisition, because it falls in the linear regime in the $\frac{dI}{I}$ vs pump power for any perspective.

5.6.3 Long scan analysis

This section describes the time-dependent data of PMCP in smaller time steps. Time dependent data shows how the scattering signal changes with progression of photoreaction. We selected 75mW based on the pump power to do the long scan from -5ps to 10ps, with a smallest time step of 50fs. In this section we will discuss the long scan based on difference diffraction data (dI/I), ΔsM, and ΔPDF.

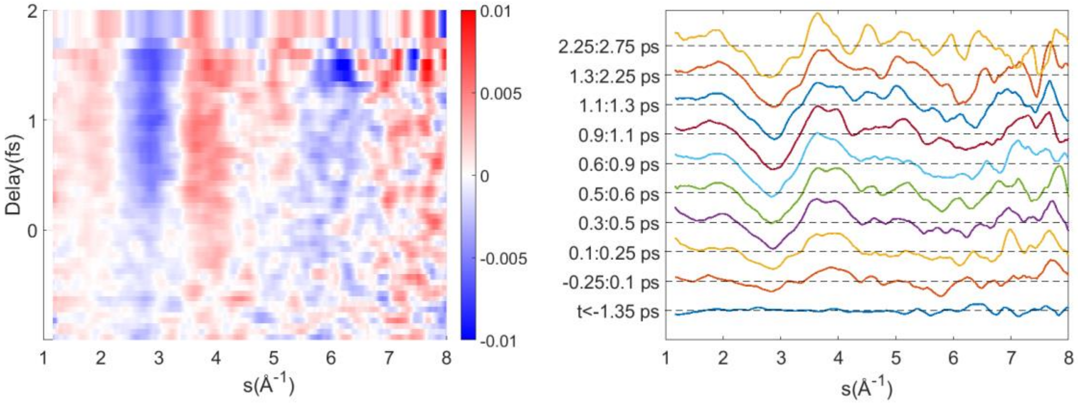

Figure 5.6: Time-dependent pump-probe signal for PMCP. (a) Experimental two dimensional $\frac{dI}{I}$ data for PMCP. Here, data from different runs are all averaged based on time-zero, discussed in section 5.5. A clear pump probe signal is seen in the 2D plot. (b) time-averaged lineout of the $\frac{dI}{I}$. The growth of signal is more obvious in this plot.

Figure 5.6a shows the 2D $\frac{dI}{I}$ as a pump-probe signal for PMCP. $\frac{dI}{I}$ was calculated using equation (2.6). We averaged all the diffraction images for the delay stages before -1ps to calculate $I(s, t < 0)$ in equation (2.6). In the figure, the horizontal axis represents the momentum transfer vector, s, and the vertical axis shows the delay between the arrival of pump and probe pulses. In Figure 5.6a, a clear pump probe signal can be seen, and features appear for the entire s range, although SNR is poor at higher s due to lower count. The features indicate the relative change in the structure of PMCP due to photo excitation with respect to the ground state molecule. We measured the rise time for the dynamics of PMCP based on the feature between $s = 2.0 - 3.2\text{Å}^{-1}$, which gives 560fs. We fit the signal at this s-range using equation (2.10) in the time range -1ps to 1ps. The rise time of the feature between $s = 3.4 - 4.2\text{Å}^{-1}$ obtained 620fs. We could not fit the other feature because of the noise due to the lower count.

We took the time-averaged signal of $\frac{dI}{I}$ in Figure 5.6(b). The time window is shown in the vertical axis. We set the time zero at the start of the rise of the low-s signal. The change in the signal can be seen more obviously in this plot. Clearly, the signal before -1.6ps has no feature appearing. For all other time windows, signals appeared prominently at other s range as well. The features at $s = 3\text{Å}^{-1}, 4\text{Å}^{-1}$, and 6Å^{-1} are changing most prominently.

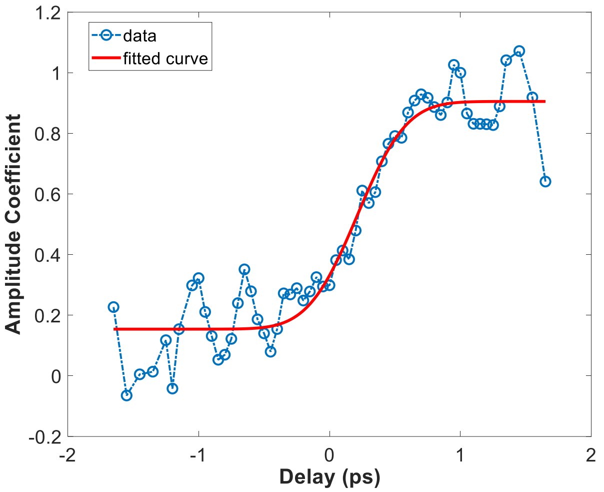

Figure 5.7: Time dependent signal analysis. dI/I of each delay point was compared to dI/I^{model} calculated using equation (5.2). The relative scaling coefficient is plotted against time.

To map the time taken for completion of the overall structural change along different degrees of freedom, and account all the features together, we made a reference model of $\frac{dI}{I}$, $\frac{dI^{model}}{I}$, by summing the $\frac{dI}{I}$ at a time window of 2ps to 5ps as following:

$$\frac{dI^{model}}{I}(s) = \frac{1}{N}\sum_{t=2ps}^{t=5ps}\frac{dI}{I}(t,s); \tag{5.2}$$

Here, N is the number of time steps from $2ps$ to $5ps$. We then fit the $\frac{dI}{I}$ of each time step with $\frac{dI^{model}}{I}$ and calculate the coefficient for the best fitting. We fitted the coefficient vs time delay plot using equation (2.10) and got a rise time of 630fs. The fitting is shown in Figure 5.7. This implies that major structural changes happen up to 630 fs and then the molecule reaches a steady state.

Since, we got the fastest dynamics happens up to 560fs, we believe there is structural change happens during the passage of nuclear wave packet from Frank Condon point to ground state based on the time constant outlined in Ref[69][171]. Fuss et al. experimentally determined that CP requires about 330fs for reaching to the CI for isomerization[173]. Since PMCP has added mass and its dynamics is expected to be slower, we predict the dynamics perhaps moves along isomerization which completes much slower than the other pathway that induces sigmatropic shifts. Compared to the time constants given in various other reports[80], [171], [172], we also think that structural change continues to happen even after the hot PMCP returns to the ground state.

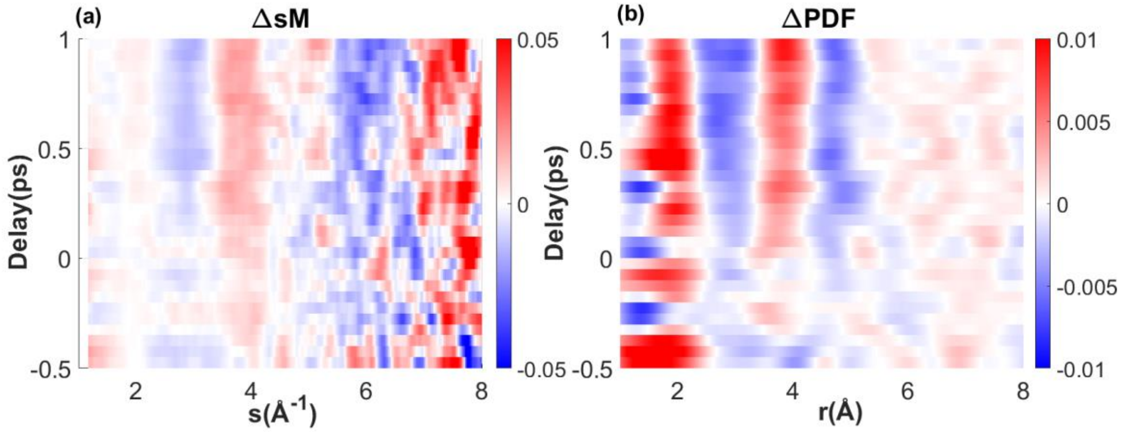

Figure 5.8: 2D ΔsM and ΔPDF. (a) Experimental 2D ΔsM, which shows a clear pump-probe signal. (b) Fourier sine transform of 2D ΔsM gives 2D ΔPDF. In the ΔPDF, clear structural changes are observed.

Figure 5.8 shows the 2D ΔsM and its sine transform, $\Delta PDF,$ using the theory described in section 2.6. The 2D ΔsM also shows a clear pump-probe signal. Because of the beam block to stop the un-diffracted electron beam, we cannot have data at $s < 1.2\text{Å}^{-1}$. Before Fourier sine transforming the $\Delta sM,$ we filled the missing part of the s range in ΔsM by smoothly interpolating the data to $s = 0$. In the 2D ΔPDF we can see that there is a gain in distance at $r = 2\text{Å}$ and 4Å, while loss of distance happens at $r = 3\text{Å}$ and 5Å. We interpret that there is a displacement of atoms that contributed to an interatomic distance of 3Å and 5Å before photo excitation. After photoexcitation, atoms distribute themselves so that their interatomic distance appears at $r = 2\text{Å}$ and 4Å. Also, the feature at $r = 4\text{Å}$ moves to higher r with time. There is no significant change in ΔPDF found for a distance higher than 5Å. The feature in ΔPDF at $r = {\sim}2\text{Å}$ has some signals appeared way before time zero. This is possibly due to the fitting used in the ΔsM to remove offset in the data. A more careful analysis of this can mitigate the artifacts.

5.7 Summary

We are able to get a good pump-probe signal in KeV-UED experiment using PMCP, which has only 2 Torr vapor pressure at room temperature. By building a new sample delivery system appropriate to conduct UED experiment using low vapor pressure sample, and heating PMCP to 60-70°C, we took diffraction data that gives a good SNR up to $s = 7\text{Å}^{-1}$. We improved the momentum resolution by focusing the electron beam on the detector. The static data agrees quite well with the simulation. The time resolved data gives a good pump-probe signal for the dynamics of PMCP. We chose pump energy which did not show any sign of multiphoton effect. We determined that the fastest dynamic has a rise-time of 560fs and overall dynamics has rise-time of 630fs. Real-space analysis of ΔPDF shows some structural change due to photoreaction. Comparing the experimental data with simulation will be useful to reveal the underlying dynamics that happen in PMCP. This work is still in progress.

Conclusions

In this chapter, I will summarize my work done to investigate the UV dynamics of different cyclic molecules. In **Chapter 1**, I described my motivation for studying light-induced processes using UED based on their scientific and commercial importance. I also pointed out a few reasons why gas phase UED is superior to other phases. I also reviewed the quantum theory of scattering for a potential. I found that the atomic scattering intensity is the Fourier transform of the potential. Later, I derived the atomic form factor for electronic scattering due to atom and charge distribution. We found the relation between the scattering amplitude of electron scattering and X-ray scattering. I also reviewed the scattering amplitude for neutral atoms and ions. The scattering intensity of ions has a model like the expected Rutherford scattering. Then, I derived the elastic scattering intensity for an ensemble of randomly oriented molecules. We employed the independent atom model to derive the scattering intensity and assumed that the scattering is isotropic. Following this, I discussed the conical intersection, which plays a decisive role in photodynamics and its outcome after the photoreaction. I wrapped up this chapter by showing the difference between electron and X-ray diffraction.

In **Chapter 2**, I discussed the experiment to study the ring conversion reaction of quadricyclane initiated by 200nm UV photon and probed by MeV-UED. I described the beamline used in the SLAC National Accelerator Laboratory and the raw diffraction image clean-up procedure. When QD moves to an excited state, because of the energy barrier it cannot go large structural change. Hence, the wave packet moves in the excited state for a few hundreds of femtoseconds. After the wave packet fall to lower lying excited state due to internal conversion, which can be seen by the decay of electronic contribution of scattering signal, the excess energy dissipates along different degree of freedom which initiates the structural change. The wave packet relaxes to the ground state through a conical intersection by the continuing structural change. From our study, we found dissociation channel is involved in addition to the isomerization to NB.

In **Chapter 3**, I discussed the photochemistry of cis-stilbene initiated by a 267nm pump beam. This experiment was also done in the MeV-UED facility at SLAC. We used two different pump intensities and observed a multiphoton effect leading to ionization for both. We compared our data using simulations for one-photon and two-photon excitation. This study on the ionization dynamics of cis-stilbene gives us experimental evidence about the topology of the ionic state. After exciting to higher lying ionized state, cis stilbene cation decay to ionic ground state in about 300fs. in the ionic ground state, cis stilbene cation traps in potential well, where is vibrates through periodic structuration change. The periodic nature of potential in the well is revealed by the vibrational mode.

The diffraction experiment using low vapor-pressure molecules needs some special attention while carrying out the experiment. We often need to apply heat to the sample to get a reasonable scattering signal and arrange the whole setup accordingly. We designed and built a sample delivery system for this purpose. In **chapter 4**, I gave a detailed description of the sample delivery system and work procedure. I also designed and built a cryo-cooled trap to catch the hot molecular vapor ejected from the gas nozzle. This trap helps keep the pressure in the sample chamber steady and facilitates us to continue taking data for a long time. I also described the detailed procedure of taking time-dependent UED data using a low-vapor pressure sample and the shut-down procedure of the experiment.

Finally, in **Chapter 5**, I presented the analysis of the experimental data taken to study the UV-induced dynamics of 1, 2, 3, 4, 5 pentamethyl-cyclopentadiene. The molecule was excited using a 267nm pump photon and probed by 90KeV electron pulse. The added methyl group in PMCP slows down the dynamics because of the different topology of conical intersection and added inertia in the molecules. The added methyl groups act as energy sinks, which absorbs excess vibrational energy and impedes the molecule from undergoing large structural change. Hence, we cannot see any isomerization by our preliminary analysis. This analysis is still in progress .

References

[1] W. J. Schreier *et al.*, “Thymine dimerization in DNA is an ultrafast photoreaction,” *Science (80-.).*, vol. 315, no. 5812, pp. 625–629, 2007, doi: 10.1126/science.1135428.

[2] E. Havinga and J. L. M. A. Schlatmann, “Remarks on the specificities of the photochemical and thermal transformations in the vitamin D field,” *Tetrahedron*, vol. 16, no. 1, pp. 146–152, 1961, doi: https://doi.org/10.1016/0040-4020(61)80065-3.

[3] M. J. Molina and F. S. Rowland, “Stratospheric sink for chlorofluoromethanes: chlorine atom-catalysed destruction of ozone,” *Nature*, vol. 249, no. 5460, pp. 810–812, 1974, doi: 10.1038/249810a0.

[4] T. G. Shepherd *et al.*, “Reconciliation of halogen-induced ozone loss with the total-column ozone record,” *Nat. Geosci.*, vol. 7, no. 6, pp. 443–449, 2014, doi: 10.1038/ngeo2155.

[5] T. Young, “PHILOSOPHICAL,” 1803.

[6] L. De Broglie, “Recherches sur la théorie des quanta (Research on the Theory of the Quanta).” Ph. D. thesis, Migration-université en cours d’affectation, 1924.

[7] G. P. THOMSON and A. REID, “Diffraction of Cathode Rays by a Thin Film,” *Nature*, vol. 119, no. 3007, p. 890, 1927, doi: 10.1038/119890a0.

[8] J. NAVARRO, “Electron diffraction chez Thomson: early responses to quantum physics in Britain,” *Br. J. Hist. Sci.*, vol. 43, no. 2, pp. 245–275, 2010, doi: DOI:

10.1017/S0007087410000026.

[9] C. J. Davisson and L. H. Germer, “Reflection of Electrons by a Crystal of Nickel,” *Proc. Natl. Acad. Sci.*, vol. 14, no. 4, pp. 317–322, Apr. 1928, doi: 10.1073/pnas.14.4.317.

[10] C. Davisson and L. H. Germer, “The Scattering of Electrons by a Single Crystal of Nickel,” *Nature*, vol. 119, no. 2998, pp. 558–560, 1927, doi: 10.1038/119558a0.

[11] H. Mark and R. Wierl, “Über Elektronenbeugung am einzelnen Molekül,” *Naturwissenschaften*, vol. 18, no. 9, p. 205, 1930, doi: 10.1007/BF01494849.

[12] L. Pauling and L. O. Brockway, “The Radial Distribution Method of Interpretation of Electron Diffraction Photographs of Gas Molecules,” *J. Am. Chem. Soc.*, vol. 57, no. 12, pp. 2684–2692, Dec. 1935, doi: 10.1021/ja01315a103.

[13] G. Mourou and S. Williamson, “Picosecond electron diffraction,” *Appl. Phys. Lett.*, vol. 41, no. 1, pp. 44–45, 1982.

[14] J. C. Williamson and A. H. Zewail, “Structural femtochemistry: experimental methodology.,” *Proc. Natl. Acad. Sci.*, vol. 88, no. 11, pp. 5021–5025, Jun. 1991, doi: 10.1073/pnas.88.11.5021.

[15] J. C. Williamson, M. Dantus, S. B. Kim, and A. H. Zewail, “Ultrafast diffraction and molecular structure,” *Chem. Phys. Lett.*, vol. 196, no. 6, pp. 529–534, 1992, doi: https://doi.org/10.1016/0009-2614(92)85988-M.

[16] J. Charles Williamson and A. H. Zewail, “Ultrafast electron diffraction. Velocity mismatch and temporal resolution in crossed-beam experiments,” *Chem. Phys.*

Lett., vol. 209, no. 1, pp. 10–16, 1993, doi: https://doi.org/10.1016/0009-2614(93)87193-7.

[17] J. C. Williamson and A. H. Zewail, “Ultrafast electron diffraction. 4. Molecular structures and coherent dynamics,” *J. Phys. Chem.*, vol. 98, no. 11, pp. 2766–2781, 1994, doi: 10.1021/j100062a010.

[18] M. Dantus, S. B. Kim, J. C. Williamson, and A. H. Zewail, “Ultrafast electron diffraction. 5. Experimental time resolution and applications,” *J. Phys. Chem.*, vol. 98, no. 11, pp. 2782–2796, 1994, doi: 10.1021/j100062a011.

[19] H. Ihee, J. Cao, and A. H. Zewail, “Ultrafast electron diffraction: Structures in dissociation dynamics of Fe(CO)5,” *Chem. Phys. Lett.*, vol. 281, no. 1–3, pp. 10–19, 1997, doi: 10.1016/S0009-2614(97)01167-6.

[20] J. Cao, H. Ihee, and A. H. Zewail, “Ultrafast electron diffraction: Determination of radical structure with picosecond time resolution,” *Chem. Phys. Lett.*, vol. 290, no. 1–3, pp. 1–8, 1998, doi: 10.1016/S0009-2614(98)00520-X.

[21] G. Sciaini and R. J. D. Miller, “Femtosecond electron diffraction: Heralding the era of atomically resolved dynamics,” *Reports Prog. Phys.*, vol. 74, no. 9, 2011, doi: 10.1088/0034-4885/74/9/096101.

[22] T. van Oudheusden, E. F. de Jong, S. B. van der Geer, W. P. E. M. O. ’t Root, O. J. Luiten, and B. J. Siwick, “Electron source concept for single-shot sub-100 fs electron diffraction in the 100 keV range,” *J. Appl. Phys.*, vol. 102, no. 9, p. 93501, Nov. 2007, doi: 10.1063/1.2801027.

[23] T. van Oudheusden, P. L. E. M. Pasmans, S. B. van der Geer, M. J. de Loos, M. J. van der Wiel, and O. J. Luiten, “Compression of Subrelativistic Space-Charge-Dominated Electron Bunches for Single-Shot Femtosecond Electron Diffraction,” *Phys. Rev. Lett.*, vol. 105, no. 26, p. 264801, Dec. 2010, doi: 10.1103/PhysRevLett.105.264801.

[24] R. P. Chatelain, V. R. Morrison, C. Godbout, and B. J. Siwick, “Ultrafast electron diffraction with radio-frequency compressed electron pulses,” *Appl. Phys. Lett.*, vol. 101, no. 8, p. 81901, Aug. 2012, doi: 10.1063/1.4747155.

[25] S. P. Weathersby *et al.*, “Mega-electron-volt ultrafast electron diffraction at SLAC National Accelerator Laboratory,” *Rev. Sci. Instrum.*, vol. 86, no. 7, 2015, doi: 10.1063/1.4926994.

[26] X. Shen *et al.*, “Femtosecond gas-phase mega-electron-volt ultrafast electron diffraction,” *Struct. Dyn.*, vol. 6, no. 5, 2019, doi: 10.1063/1.5120864.

[27] J. Yang *et al.*, “Diffractive Imaging of Coherent Nuclear Motion in Isolated Molecules,” *Phys. Rev. Lett.*, vol. 117, no. 15, pp. 1–6, 2016, doi: 10.1103/PhysRevLett.117.153002.

[28] J. Yang *et al.*, “Diffractive imaging of a rotational wavepacket in nitrogen molecules with femtosecond megaelectronvolt electron pulses,” *Nat. Commun.*, vol. 7, pp. 1–9, 2016, doi: 10.1038/ncomms11232.

[29] P. Baum and A. H. Zewail, “Breaking resolution limits in ultrafast electron diffraction and microscopy,” *Proc. Natl. Acad. Sci. U. S. A.*, vol. 103, no. 44, pp. 16105–16110, 2006, doi: 10.1073/pnas.0607451103.

[30] P. Zhang, J. Yang, and M. Centurion, “Tilted femtosecond pulses for velocity matching in gas-phase ultrafast electron diffraction,” *New J. Phys.*, vol. 16, no. 8, p. 83008, 2014.

[31] Y. Xiong, K. J. Wilkin, and M. Centurion, “High-resolution movies of molecular rotational dynamics captured with ultrafast electron diffraction,” *Phys. Rev. Res.*, vol. 2, no. 4, p. 43064, 2020, doi: 10.1103/PhysRevResearch.2.043064.

[32] M. R. Otto, L. P. Renée de Cotret, M. J. Stern, and B. J. Siwick, “Solving the jitter problem in microwave compressed ultrafast electron diffraction instruments: Robust sub-50 fs cavity-laser phase stabilization,” *Struct. Dyn.*, vol. 4, no. 5, 2017, doi: 10.1063/1.4989960.

[33] K. J. Wilkin, Y. Xiong, H. Zhao, S. B. Muvva, S. K. Saha, and M. Centurion, “Ultrafast electron diffraction from transiently aligned asymmetric top molecules: Rotational dynamics and structure retrieval,” *Struct. Dyn.*, vol. 9, no. 5, p. 54303, Oct. 2022, doi: 10.1063/4.0000163.

[34] Y. Xiong, K. J. Wilkin, S. K. Saha, S. B. Muvva, H. Zhao, and M. Centurion, “Retrieval of the molecular orientation distribution from atom-pair angular distributions,” *Phys. Rev. A*, vol. 106, no. 3, p. 33109, Sep. 2022, doi: 10.1103/PhysRevA.106.033109.

[35] Y. Xiong, H. Zhao, S. K. Saha, S. B. Muvva, K. J. Wilkin, and M. Centurion, “Isotope detection in molecules with ultrafast electron diffraction and rotational spectrometry,” *J. Phys. Commun.*, vol. 6, no. 5, p. 55006, 2022, doi: 10.1088/2399-6528/ac6aaf.

[36] D. W. H. Rankin, C. A. Morrison, and N. W. T. A.-T. T.- Mitzel, “Structural methods in molecular inorganic chemistry.” Wiley Chichester, West Sussex, United Kingdom, Chichester, West Sussex, United Kingdom, 2013, doi: LK - https://worldcat.org/title/810442747.

[37] D. J. Griffiths and D. F. Schroeter, *Introduction to quantum mechanics*. Cambridge university press, 2018.

[38] L. O. Brockway, “Electron diffraction by gas molecules,” *Rev. Mod. Phys.*, vol. 8, no. 3, pp. 231–266, 1936, doi: 10.1103/RevModPhys.8.231.

[39] R. Shankar, “Shankar - Principles of quantum mechanics.pdf,” *kKuwer Academic/Plenum Publishers*, vol. 53, no. 9. pp. 1689–1699, 1982.

[40] O. Zandi, “Design and Construction of a High-Current Femtosecond Gas-Phase Electron Diffraction Setup,” 2017.

[41] M. Centurion, T. J. A. Wolf, and J. Yang, “Ultrafast Imaging of Molecules with Electron Diffraction,” *Annu. Rev. Phys. Chem.*, vol. 73, pp. 21–42, 2022, doi: 10.1146/annurev-physchem-082720-010539.

[42] L. O. Brockway, “Electron diffraction by gas molecules,” *Rev. Mod. Phys.*, vol. 8, no. 3, p. 231, 1936.

[43] V. Schomaker and R. O. Y. Glauber, “The Born approximation in electron diffraction,” *Nature*, vol. 170, no. 4320, pp. 290–291, 1952.

[44] M. Hargittai, *Stereochemical Applications of Gas-Phase Electron Diffraction, Part A*, vol. 4. John Wiley & Sons, 1988.

[45] F. Salvat, A. Jablonski, and C. J. Powell, “elsepa—Dirac partial-wave calculation of elastic scattering of electrons and positrons by atoms, positive ions and molecules (New Version Announcement),” *Comput. Phys. Commun.*, vol. 261, p. 107704, 2021, doi: https://doi.org/10.1016/j.cpc.2020.107704.

[46] P. Debye, “Zerstreuung von röntgenstrahlen,” *Ann. Phys.*, vol. 351, no. 6, pp. 809–823, 1915.

[47] S. Shibata, H. Sekiyama, K. Tachikawa, and M. Moribe, “Chemical bonding effect in electron scattering by gaseous molecules,” *J. Mol. Struct.*, vol. 641, no. 1, pp. 1–6, 2002, doi: 10.1016/S0022-2860(01)00962-0.

[48] R. A. Bonham and T. Iijima, “Preliminary Electron-Diffraction Study of H2 at Small Scattering Angles,” *J. Chem. Phys.*, vol. 42, no. 7, pp. 2612–2614, Jul. 2004, doi: 10.1063/1.1696344.

[49] T. Iijima, R. A. Bonham, C. Tavard, M. Roux, and M. Cornille, “Small-angle Scattering from Methane, Ammonia and Water by Fast Electrons,” *Bull. Chem. Soc. Jpn.*, vol. 38, no. 10, pp. 1757–1760, Oct. 1965, doi: 10.1246/bcsj.38.1757.

[50] J. Wang, A. N. Tripathi, and V. H. Smith, “Chemical binding and electron correlation effects in x-ray and high energy electron scattering,” *J. Chem. Phys.*, vol. 101, no. 6, pp. 4842–4854, 1994, doi: 10.1063/1.467407.

[51] A. Duguet, A. Lahmam-Bennani, and M. Rouault, “High energy elastic and inelastic electron scattering by the NH3 molecule-binding effect,” *J. Chem. Phys.*, vol. 78, no. 11, pp. 6595–6597, 1983, doi: 10.1063/1.444655.

[52] Y. Xiong *et al.*, “Strong-field induced fragmentation and isomerization of toluene probed by ultrafast femtosecond electron diffraction and mass spectrometry,” *Faraday Discuss.*, vol. 228, pp. 39–59, 2021, doi: 10.1039/d0fd00125b.

[53] J. Yang *et al.*, “Simultaneous observation of nuclear and electronic dynamics by ultrafast electron diffraction,” *Science (80-.).*, vol. 368, no. 6493, pp. 885–889, 2020, doi: 10.1126/science.abb2235.

[54] T. Northey, A. Moreno Carrascosa, S. Schäfer, and A. Kirrander, “Elastic X-ray scattering from state-selected molecules,” *J. Chem. Phys.*, vol. 145, no. 15, 2016, doi: 10.1063/1.4962256.

[55] T. Northey, N. Zotev, and A. Kirrander, “Ab initio calculation of molecular diffraction,” *J. Chem. Theory Comput.*, vol. 10, no. 11, pp. 4911–4920, 2014, doi: 10.1021/ct500096r.

[56] J. Yang *et al.*, “Simultaneous observation of nuclear and electronic dynamics by ultrafast electron diffraction,” vol. 889, no. May, pp. 885–889, 2020.

[57] A. Moreno Carrascosa, H. Yong, D. L. Crittenden, P. M. Weber, and A. Kirrander, “Ab Initio Calculation of Total X-ray Scattering from Molecules,” *J. Chem. Theory Comput.*, vol. 15, no. 5, pp. 2836–2846, 2019, doi: 10.1021/acs.jctc.9b00056.

[58] G. Sansone *et al.*, “Electron localization following attosecond molecular photoionization,” *Nature*, vol. 465, no. 7299, pp. 763–766, 2010, doi: 10.1038/nature09084.

[59] M. Nisoli, P. Decleva, F. Calegari, A. Palacios, and F. Martín, “Attosecond Electron Dynamics in Molecules,” *Chem. Rev.*, vol. 117, no. 16, pp. 10760–10825, 2017, doi: 10.1021/acs.chemrev.6b00453.

[60] E. Goulielmakis *et al.*, “Real-time observation of valence electron motion,” *Nature*, vol. 466, no. 7307, pp. 739–743, 2010, doi: 10.1038/nature09212.

[61] M. Hentschel *et al.*, “Attosecond metrology,” *Nature*, vol. 414, no. 6863, pp. 509–513, 2001, doi: 10.1038/35107000.

[62] P. B. Corkum and F. Krausz, “Attosecond science,” *Nat. Phys.*, vol. 3, no. 6, pp. 381–387, 2007, doi: 10.1038/nphys620.

[63] H. Kapteyn, O. Cohen, I. Christov, and M. Murnane, “Harnessing attosecond science in the quest for coherent X-rays,” *Science (80-.).*, vol. 317, no. 5839, pp. 775–778, 2007.

[64] P. W. Atkins and J. de Paula, *Atkins’ Physical Chemistry*. OUP Oxford, 2014.

[65] M. Boggio-pasqua, “Computational mechanistic photochemistry : The central role of conical intersections Manuscrit par Martial BOGGIO-PASQUA Computational mechanistic photochemistry : The central role of conical intersections,” p. 86, 2015.

[66] B. G. Levine and T. J. Martínez, “Isomerization Through Conical Intersections,” *Annu. Rev. Phys. Chem.*, vol. 58, no. 1, pp. 613–634, 2007, doi: 10.1146/annurev.physchem.57.032905.104612.

[67] M. Chachisvilis and A. H. Zewail, “Femtosecond Dynamics of Pyridine in the

Condensed Phase: Valence Isomerization by Conical Intersections," *J. Phys. Chem. A*, vol. 103, no. 37, pp. 7408–7418, 1999, doi: 10.1021/jp991821x.

[68] F. Bernardi, M. Olivucci, and M. A. Robb, "Potential energy surface crossings in organic photochemistry," *Chem. Soc. Rev.*, vol. 25, no. 5, pp. 321–328, 1996, doi: 10.1039/cs9962500321.

[69] O. Schalk *et al.*, "Substituent effects on dynamics at conical intersections: Cycloheptatrienes," *J. Phys. Chem. A*, vol. 117, no. 40, pp. 10239–10247, 2013, doi: 10.1021/jp309875m.

[70] W. Domcke and D. R. Yarkony, "Role of Conical Intersections in Molecular Spectroscopy and Photoinduced Chemical Dynamics," *Annu. Rev. Phys. Chem.*, vol. 63, no. 1, pp. 325–352, 2012, doi: 10.1146/annurev-physchem-032210-103522.

[71] G. A. Worth and L. S. Cederbaum, "Beyond born-oppenheimer: Molecular dynamics through a conical intersection," *Annu. Rev. Phys. Chem.*, vol. 55, pp. 127–158, 2004, doi: 10.1146/annurev.physchem.55.091602.094335.

[72] W. Domcke, D. R. Yarkony, and H. Köppel, "Conical Intersections," vol. 15. p. 838, 2004.

[73] T. J. Martinez, "Seaming is believing," *Nature*, vol. 467, no. 7314, pp. 412–413, 2010, doi: 10.1038/467412a.

[74] J. Yang *et al.*, "Imaging CF3I conical intersection and photodissociation dynamics with ultrafast electron diffraction," *Science (80-.).*, vol. 361, no. 6397, pp. 64–67,

2018, doi: 10.1126/science.aat0049.

[75] J. Michl and V. Bonačić-Koutecký, “Electronic aspects of organic photochemistry,” *(No Title)*, 1990.

[76] F. Bernardi, S. De, M. Olivucci, and M. A. Robb, “The mechanism of ground-state-forbidden photochemical pericyclic reactions: evidence for real conical intersections,” *J. Am. Chem. Soc.*, vol. 112, no. 5, pp. 1737–1744, Feb. 1990, doi: 10.1021/ja00161a013.

[77] I. J. Palmer, M. Olivucci, F. Bernardi, and M. A. Robb, “An MC-SCF study of the thermal and photochemical cycloaddition of Dewar benzene,” *J. Org. Chem.*, vol. 57, no. 19, pp. 5081–5087, 1992.

[78] A. L. Sobolewski, C. Woywod, and W. Domcke, “Ab initio investigation of potential-energy surfaces involved in the photophysics of benzene and pyrazine,” *J. Chem. Phys.*, vol. 98, no. 7, pp. 5627–5641, 1993.

[79] M. Klessinger, “Conical Intersections and the Mechanism of Singlet Photoreactions,” *Angew. Chemie Int. Ed. English*, vol. 34, no. 5, pp. 549–551, 1995, doi: 10.1002/anie.199505491.

[80] O. Schalk *et al.*, “Substituent Effects on Dynamics at Conical Intersections: Cycloheptatrienes,” *J. Phys. Chem. A*, vol. 117, no. 40, pp. 10239–10247, Oct. 2013, doi: 10.1021/jp309875m.

[81] A. Odate, A. Kirrander, P. M. Weber, and M. P. Minitti, “Brighter, faster, stronger: ultrafast scattering of free molecules,” *Adv. Phys. X*, vol. 8, no. 1, 2023, doi:

10.1080/23746149.2022.2126796.

[82] M. Stefanou, K. Saita, D. V. Shalashilin, and A. Kirrander, “Comparison of ultrafast electron and X-ray diffraction – A computational study,” *Chem. Phys. Lett.*, vol. 683, pp. 300–305, 2017, doi: 10.1016/j.cplett.2017.03.007.

[83] C. G. Shull and E. O. Wollan, “X-Ray, Electron, and Neutron Diffraction,” *Science (80-.).*, vol. 108, no. 2795, pp. 69–75, Jul. 1948, doi: 10.1126/science.108.2795.69.

[84] R. Henderson, “The potential and limitations of neutrons, electrons and X-rays for atomic resolution microscopy of unstained biological molecules,” *Q. Rev. Biophys.*, vol. 28, no. 2, pp. 171–193, 1995, doi: DOI: 10.1017/S003358350000305X.

[85] C. Bostedt *et al.*, “Ultra-fast and ultra-intense x-ray sciences: First results from the Linac Coherent Light Source free-electron laser,” *J. Phys. B At. Mol. Opt. Phys.*, vol. 46, no. 16, 2013, doi: 10.1088/0953-4075/46/16/164003.

[86] J. M. Glownia *et al.*, “Self-Referenced Coherent Diffraction X-Ray Movie of Ångstrom- and Femtosecond-Scale Atomic Motion,” *Phys. Rev. Lett.*, vol. 117, no. 15, pp. 1–5, 2016, doi: 10.1103/PhysRevLett.117.153003.

[87] J. Küpper *et al.*, “X-ray diffraction from isolated and strongly aligned gas-phase molecules with a free-electron laser,” *Phys. Rev. Lett.*, vol. 112, no. 8, pp. 1–6, 2014, doi: 10.1103/PhysRevLett.112.083002.

[88] M. P. Minitti *et al.*, “Imaging Molecular Motion: Femtosecond X-Ray Scattering

of an Electrocyclic Chemical Reaction," *Phys. Rev. Lett.*, vol. 114, no. 25, pp. 1–5, 2015, doi: 10.1103/PhysRevLett.114.255501.

[89] T. R. Cook, D. K. Dogutan, S. Y. Reece, Y. Surendranath, T. S. Teets, and D. G. Nocera, "Solar energy supply and storage for the legacy and nonlegacy worlds," *Chem. Rev.*, vol. 110, no. 11, pp. 6474–6502, 2010, doi: 10.1021/cr100246c.

[90] J. R. Bolton and D. O. Hall, "Photochemical conversion and storage of solar energy," *Annu. Rev. Energy*, vol. 4, no. 1, pp. 353–401, 1979.

[91] N. S. Lewis and D. G. Nocera, "Powering the planet: Chemical challenges in solar energy utilization," *Proc. Natl. Acad. Sci.*, vol. 103, no. 43, pp. 15729–15735, 2006.

[92] D. G. Nocera, "On the future of global energy," *Daedalus*, vol. 135, no. 4, pp. 112–115, 2006.

[93] J. Barber, "Photosynthetic energy conversion: natural and artificial," *Chem. Soc. Rev.*, vol. 38, no. 1, pp. 185–196, 2009.

[94] R. Eisenberg and D. G. Nocera, "Preface: Overview of the forum on solar and renewable energy," *Inorg. Chem.*, vol. 44, no. 20, pp. 6799–6801, 2005.

[95] I. Gur, K. Sawyer, and R. Prasher, "Searching for a better thermal battery," *Science (80-.).*, vol. 335, no. 6075, pp. 1454–1455, 2012.

[96] E. E. Barton, D. M. Rampulla, and A. B. Bocarsly, "Selective solar-driven reduction of CO2 to methanol using a catalyzed p-GaP based photoelectrochemical cell," *J. Am. Chem. Soc.*, vol. 130, no. 20, pp. 6342–6344, 2008.

[97] A. M. Kolpak and J. C. Grossman, “Azobenzene-functionalized carbon nanotubes as high-energy density solar thermal fuels,” *Nano Lett.*, vol. 11, no. 8, pp. 3156–3162, 2011.

[98] Y. Feng *et al.*, “Covalent functionalization of graphene by azobenzene with molecular hydrogen bonds for long-term solar thermal storage,” *Sci. Rep.*, vol. 3, no. 1, p. 3260, 2013.

[99] T. J. Kucharski, N. Ferralis, A. M. Kolpak, J. O. Zheng, D. G. Nocera, and J. C. Grossman, “Templated assembly of photoswitches significantly increases the energy-storage capacity of solar thermal fuels,” *Nat. Chem.*, vol. 6, no. 5, pp. 441–447, 2014.

[100] V. Caia, G. Cum, R. Gallo, V. Mancini, and E. Pitoni, “A high enthalpy value in thermal isomerization of photosynthesized cis-9-styrylacridines,” *Tetrahedron Lett.*, vol. 24, no. 36, pp. 3903–3904, 1983.

[101] C. Bastianelli, V. Caia, G. Cum, R. Gallo, and V. Mancini, “Thermal isomerization of photochemically synthesized (Z)-9-styrylacridines. An unusually high enthalpy of Z→ E conversion for stilbene-like compounds,” *J. Chem. Soc. Perkin Trans. 2*, no. 5, pp. 679–683, 1991.

[102] V. Gray, A. Lennartson, P. Ratanalert, K. Börjesson, and K. Moth-Poulsen, “Diaryl-substituted norbornadienes with red-shifted absorption for molecular solar thermal energy storage,” *Chem. Commun.*, vol. 50, no. 40, pp. 5330–5332, 2014.

[103] A. D. Dubonosov, V. A. Bren, and V. A. Chernoivanov, “Norbornadiene–quadricyclane as an abiotic system for the storage of solar energy,” *Russ. Chem.*

Rev., vol. 71, no. 11, pp. 917–927, 2002.

[104] Z. Yoshida, “New molecular energy storage systems,” *J. Photochem.*, vol. 29, no. 1–2, pp. 27–40, 1985.

[105] V. A. Bren, A. D. Dubonosov, V. I. Minkin, and V. A. Chernoivanov, “Norbornadiene-quadricyclane—an effective molecular system for the storage of solar energy,” *Russ. Chem. Rev.*, vol. 60, no. 5, pp. 451–469, 1991.

[106] M. J. Kuisma, A. M. Lundin, K. Moth-Poulsen, P. Hyldgaard, and P. Erhart, “Comparative Ab-Initio Study of Substituted Norbornadiene-Quadricyclane Compounds for Solar Thermal Storage,” *J. Phys. Chem. C*, vol. 120, no. 7, pp. 3635–3645, 2016, doi: 10.1021/acs.jpcc.5b11489.

[107] F. Coppola, M. Nucci, M. Marazzi, D. Rocca, and M. Pastore, “Norbornadiene/Quadricyclane System in the Spotlight: The Role of Rydberg States and Dynamic Electronic Correlation in a Solar-Thermal Building Block,” *ChemPhotoChem*, vol. 7, no. 4, 2023, doi: 10.1002/cptc.202200214.

[108] X. An and Y. Xie, “Enthalpy of isomerization of quadricyclane to norbornadiene,” *Thermochim. Acta*, vol. 220, pp. 17–25, 1993, doi: https://doi.org/10.1016/0040-6031(93)80451-F.

[109] F. Rudakov and P. M. Weber, “Ultrafast structural and isomerization dynamics in the Rydberg-exited Quadricyclane: Norbornadiene system,” *J. Chem. Phys.*, vol. 136, no. 13, 2012, doi: 10.1063/1.3697472.

[110] K. Borne *et al.*, “Probing (or : Revealing ?) the Ultrafast Electronic Relaxation

Pathways of UV-excited Quadricyclane.”

[111] J. Yang *et al.*, “Femtosecond gas phase electron diffraction with MeV electrons,” *Faraday Discuss.*, vol. 194, pp. 563–581, 2016, doi: 10.1039/c6fd00071a.

[112] J. Kennedy and R. Eberhart, “Particle swarm optimization,” in *Proceedings of ICNN’95 - International Conference on Neural Networks*, 1995, vol. 4, pp. 1942–1948 vol.4, doi: 10.1109/ICNN.1995.488968.

[113] M. Erik, H. Pedersen, and M. E. H. Pedersen, “Good parameters for particle swarm optimization,” *Tech. Rep. HL1001, Hvass Lab.*, vol. HL1001, pp. 1–12, 2010.

[114] W. Fuß, C. Kosmidis, W. E. Schmid, and S. A. Trushin, “The photochemical cis-trans isomerization of free stilbene molecules follows a hula-twist pathway,” *Angew. Chemie - Int. Ed.*, vol. 43, no. 32, pp. 4178–4182, 2004, doi: 10.1002/anie.200454221.

[115] J. A. Syage, P. M. Felker, and A. H. Zewail, “Picosecond dynamics and photoisomerization of stilbene in supersonic beams. I. Spectra and mode assignments,” *J. Chem. Phys.*, vol. 81, no. 11, pp. 4685–4705, 1984, doi: 10.1063/1.447519.

[116] J. Saltiel, A. S. Waller, and D. F. Sears, “Dynamics of cis-stilbene photoisomerization: the adiabatic pathway to excited trans-stilbene,” *J. Photochem. Photobiol. A Chem.*, vol. 65, no. 1, pp. 29–40, 1992, doi: https://doi.org/10.1016/1010-6030(92)85029-T.

[117] L. Nikowa, D. Schwarzer, J. Troe, and J. Schroeder, “Viscosity and solvent dependence of low-barrier processes: Photoisomerization of cis-stilbene in compressed liquid solvents,” *J. Chem. Phys.*, vol. 97, no. 7, pp. 4827–4835, 1992, doi: 10.1063/1.463837.

[118] J. S. Baskin, L. Bañares, S. Pedersen, and A. H. Zewail, “Femtosecond Real-Time Probing of Reactions. 20. Dynamics of Twisting, Alignment, and IVR in the trans-Stilbene Isomerization Reaction,” *J. Phys. Chem.*, vol. 100, no. 29, pp. 11920–11933, Jan. 1996, doi: 10.1021/jp960909x.

[119] B. I. Greene and R. C. Farrow, “Subpicosecond time resolved multiphoton ionization: Excited state dynamics of cis-stilbene under collision free conditions,” *J. Chem. Phys.*, vol. 78, no. 6, pp. 3336–3338, 1983, doi: 10.1063/1.445201.

[120] S. Abrash, S. Repinec, and R. M. Hochstrasser, “The viscosity dependence and reaction coordinate for isomerization of cis-stilbene,” *J. Chem. Phys.*, vol. 93, no. 2, pp. 1041–1053, 1990, doi: 10.1063/1.459168.

[121] S. Pedersen, L. Bañares, and A. H. Zewail, “Femtosecond vibrational transition-state dynamics in a chemical reaction [1],” *J. Chem. Phys.*, vol. 97, no. 11, pp. 8801–8804, 1992, doi: 10.1063/1.463350.

[122] D. C. Todd, J. M. Jean, S. J. Rosenthal, A. J. Ruggiero, D. Yang, and G. R. Fleming, “Fluorescence upconversion study of cis-stilbene isomerization,” *J. Chem. Phys.*, vol. 93, no. 12, pp. 8658–8668, Dec. 1990, doi: 10.1063/1.459252.

[123] J. H. Frederick, Y. Fujiwara, J. H. Penn, K. Yoshihara, and H. Petek, “Models for stilbene photoisomerization: Experimental and theoretical studies of the excited-

state dynamics of 1,2-diphenylcycloalkenes," *J. Phys. Chem.*, vol. 95, no. 7, pp. 2845–2858, 1991, doi: 10.1021/j100160a040.

[124] S. T. Repinec, R. J. Sension, A. Z. Szarka, and R. M. Hochstrasser, "Femtosecond laser studies of the cis-stilbene photoisomerization reactions. The cis-stilbene to dihydrophenanthrene reaction," *J. Phys. Chem.*, vol. 95, no. 25, pp. 10380–10385, 1991, doi: 10.1021/j100178a026.

[125] M. J. Bearpark, F. Bernardi, S. Clifford, M. Olivucci, M. A. Robb, and T. Vreven, "Cooperating rings in cis-stilbene lead to an S0/S1 conical intersection," *J. Phys. Chem. A*, vol. 101, no. 21, pp. 3841–3847, 1997, doi: 10.1021/jp961509c.

[126] T. Nakamura, S. Takeuchi, T. Taketsugu, and T. Tahara, "Femtosecond fluorescence study of the reaction pathways and nature of the reactive S 1 state of cis-stilbene," *Phys. Chem. Chem. Phys.*, vol. 14, no. 18, pp. 6225–6232, 2012, doi: 10.1039/c2cp23959k.

[127] W. Fuß, C. Kosmidis, W. E. Schmid, and S. A. Trushin, "The lifetime of the perpendicular minimum of cis-stilbene observed by dissociative intense-laser field ionization," *Chem. Phys. Lett.*, vol. 385, no. 5–6, pp. 423–430, 2004, doi: 10.1016/j.cplett.2003.12.114.

[128] J. Bao, M. P. Minitti, and P. M. Weber, "Ring-closing and dehydrogenation reactions of highly excited cis-stilbene: Ultrafast spectroscopy and structural dynamics," *J. Phys. Chem. A*, vol. 115, no. 9, pp. 1508–1515, 2011, doi: 10.1021/jp1095322.

[129] Y. Amatatsu, "Ab initio study on the electronic structures of stilbene at the conical

intersection," *Chem. Phys. Lett.*, vol. 314, no. 3, pp. 364–368, 1999, doi: https://doi.org/10.1016/S0009-2614(99)01042-8.

[130] J. Quenneville and T. J. Martínez, "Ab initio study of cis-trans photoisomerization in stilbene and ethylene," *J. Phys. Chem. A*, vol. 107, no. 6, pp. 829–837, 2003, doi: 10.1021/jp021210w.

[131] N. Minezawa and M. S. Gordon, "Photoisomerization of stilbene: A spin-flip density functional theory approach," *J. Phys. Chem. A*, vol. 115, no. 27, pp. 7901–7911, 2011, doi: 10.1021/jp203803a.

[132] G. Tomasello, M. Garavelli, and G. Orlandi, "Tracking the stilbene photoisomerization in the S1 state using RASSCF," *Phys. Chem. Chem. Phys.*, vol. 15, no. 45, pp. 19763–19773, 2013, doi: 10.1039/C3CP52310A.

[133] I. N. Ioffe and A. A. Granovsky, "Photoisomerization of stilbene: The detailed XMCQDPT2 treatment," *J. Chem. Theory Comput.*, vol. 9, no. 11, pp. 4973–4990, 2013, doi: 10.1021/ct400647w.

[134] H. Weir, M. Williams, R. M. Parrish, E. G. Hohenstein, and T. J. Martínez, "Nonadiabatic Dynamics of Photoexcited cis-Stilbene Using Ab Initio Multiple Spawning," *J. Phys. Chem. B*, vol. 124, no. 26, pp. 5476–5487, 2020, doi: 10.1021/acs.jpcb.0c03344.

[135] Y. Dou and R. E. Allen, "Another important coordinate in the photoisomerization of cis-stilbene," *Chem. Phys. Lett.*, vol. 378, no. 3–4, pp. 323–329, 2003, doi: 10.1016/S0009-2614(03)01316-2.

[136] D. H. Waldeck, “Photoisomerization Dynamics of Stilbenes,” *Chem. Rev.*, vol. 91, no. 3, pp. 415–436, 1991, doi: 10.1021/cr00003a007.

[137] S. T. Repinec, R. J. Sension, A. Z. Szarka, and R. M. Hochstrasser, “Femtosecond laser studies of the cis-stilbene photoisomerization reactions. The cis-stilbene to dihydrophenanthrene reaction,” *J. Phys. Chem.*, vol. 95, no. 25, pp. 10380–10385, 1991, doi: 10.1021/j100178a026.

[138] G. J. Fisher and H. E. Johns, “Rapid #: -17931386,” 2021.

[139] C. S. Wood, “/I(Si)s*c 11,” vol. 153, no. 2, 1963.

[140] H. Petek, K. Yoshihara, Y. Fujiwara, Z. Lin, J. H. Penn, and J. H. Frederick, “Is the nonradiative decay of S1 cis-stilbene due to the dihydrophenanthrene isomerization channel? Suggestive evidence from photophysical measurements on 1,2-diphenylcycloalkenes,” *J. Phys. Chem.*, vol. 94, no. 19, pp. 7539–7543, 1990, doi: 10.1021/j100382a043.

[141] S. Karashima *et al.*, “Ultrafast Ring Closure Reaction of Gaseous cis-Stilbene from S1(ππ*),” *J. Am. Chem. Soc.*, vol. 145, no. 6, pp. 3283–3288, 2023, doi: 10.1021/jacs.2c12266.

[142] J. Bao and P. M. Weber, “Ultrafast dynamics of highly excited trans-stilbene: A different twist,” *J. Phys. Chem. Lett.*, vol. 1, no. 1, pp. 224–227, 2010, doi: 10.1021/jz900147b.

[143] T. J. A. Wolf *et al.*, “electron diffraction,” vol. 11, no. June, 2019.

[144] Y. Liu *et al.*, “Rehybridization dynamics into the pericyclic minimum of an

electrocyclic reaction imaged in real-time," *Nat. Commun.*, vol. 14, no. 1, pp. 1–9, 2023, doi: 10.1038/s41467-023-38513-6.

[145] E. G. Champenois *et al.*, "Conformer-specific photochemistry imaged in real space and time," *Opt. InfoBase Conf. Pap.*, vol. 182, no. October, pp. 178–182, 2022, doi: 10.1364/up.2022.f2a.6.

[146] M. Taniguchi, H. Du, and J. S. Lindsey, "PhotochemCAD 3: diverse modules for photophysical calculations with multiple spectral databases," *Photochem. Photobiol.*, vol. 94, no. 2, pp. 277–289, 2018.

[147] M. Taniguchi and J. S. Lindsey, "Database of absorption and fluorescence spectra of> 300 common compounds for use in photochem CAD," *Photochem. Photobiol.*, vol. 94, no. 2, pp. 290–327, 2018.

[148] K. J. Wilkin *et al.*, "Diffractive imaging of dissociation and ground-state dynamics in a complex molecule," *Phys. Rev. A*, vol. 100, no. 2, p. 23402, 2019, doi: 10.1103/PhysRevA.100.023402.

[149] E. Mezura-Montes and C. A. Coello Coello, "Constraint-handling in nature-inspired numerical optimization: Past, present and future," *Swarm Evol. Comput.*, vol. 1, no. 4, pp. 173–194, 2011, doi: https://doi.org/10.1016/j.swevo.2011.10.001.

[150] M. Williams *et al.*, "Unmasking the cis-Stilbene Phantom State via Vacuum Ultraviolet Time-Resolved Photoelectron Spectroscopy and Ab Initio Multiple Spawning," *J. Phys. Chem. Lett.*, vol. 12, no. 27, pp. 6363–6369, 2021, doi: 10.1021/acs.jpclett.1c01227.

[151] F. Neese, F. Wennmohs, U. Becker, and C. Riplinger, “The ORCA quantum chemistry program package,” *J. Chem. Phys.*, vol. 152, no. 22, p. 224108, Jun. 2020, doi: 10.1063/5.0004608.

[152] M. D. Hanwell, D. E. Curtis, D. C. Lonie, T. Vandermeersch, E. Zurek, and G. R. Hutchison, “Avogadro: an advanced semantic chemical editor, visualization, and analysis platform,” *J. Cheminform.*, vol. 4, no. 1, p. 17, 2012, doi: 10.1186/1758-2946-4-17.

[153] O. Zandi, K. J. Wilkin, Y. Xiong, and M. Centurion, “High current table-top setup for femtosecond gas electron diffraction,” *Struct. Dyn.*, vol. 4, no. 4, p. 44022, May 2017, doi: 10.1063/1.4983225.

[154] K. J. Wilkin, “Laser Induced Molecular Dynamics Imaged with Ultrafast Electron Diffraction.” The University of Nebraska-Lincoln, 2022.

[155] Y. Xiong, “DIFFRACTIVE IMAGING OF LASER INDUCED MOLECULAR,” 2023.

[156] O. F. Hagena, “Nucleation and growth of clusters in expanding nozzle flows,” *Surf. Sci.*, vol. 106, no. 1–3, pp. 101–116, 1981, doi: 10.1016/0039-6028(81)90187-4.

[157] O. Zandi, K. J. Wilkin, and M. Centurion, “Implementation and modeling of a femtosecond laser-activated streak camera,” *Rev. Sci. Instrum.*, vol. 88, no. 6, 2017, doi: 10.1063/1.4985008.

[158] P. Baum and A. H. Zewail, “Breaking resolution limits in ultrafast electron

diffraction and microscopy," *Proc. Natl. Acad. Sci.*, vol. 103, no. 44, pp. 16105–16110, Oct. 2006, doi: 10.1073/pnas.0607451103.

[159] P. Zhang, J. Yang, and M. Centurion, "Tilted femtosecond pulses for velocity matching in gas-phase ultrafast electron diffraction," *New J. Phys.*, vol. 16, 2014, doi: 10.1088/1367-2630/16/8/083008.

[160] J. Yang *et al.*, "Femtosecond gas phase electron diffraction with MeV electrons," *Faraday Discuss.*, vol. 194, no. 0, pp. 563–581, 2016, doi: 10.1039/C6FD00071A.

[161] Y. Wang *et al.*, "Ultrafast electron diffraction instrument for gas and condensed matter samples," *Rev. Sci. Instrum.*, vol. 94, no. 5, 2023, doi: 10.1063/5.0146577.

[162] H. Kandori, Y. Shichida, and T. Yoshizawa, "Kandori2001_Article_PhotoisomerizationInRhodopsin," vol. 66, no. 11, 2001.

[163] D. Polli *et al.*, "Conical intersection dynamics of the primary photoisomerization event in vision," *Nature*, vol. 467, no. 7314, pp. 440–443, 2010, doi: 10.1038/nature09346.

[164] B. P. Krueger, G. D. Scholes, R. Jimenez, and G. R. Fleming, "Electronic excitation transfer from carotenoid to bacteriochlorophyll in the purple bacterium Rhodopseudomonas acidophila," *J. Phys. Chem. B*, vol. 102, no. 12, pp. 2284–2292, 1998, doi: 10.1021/jp973062t.

[165] P. J. Walla, P. A. Linden, C. P. Hsu, G. D. Scholes, and G. R. Fleming, "Femtosecond dynamics of the forbidden carotenoid S1 state in light-harvesting complexes of purple bacteria observed after two-photon excitation," *Proc. Natl.*

Acad. Sci. U. S. A., vol. 97, no. 20, pp. 10808–10813, 2000, doi: 10.1073/pnas.190230097.

[166] G. D. Andrews and J. E. Baldwin, “Phototransposition of Carbon Atoms in Cyclopentadiene. Photoisomerization of Cyclopentadiene to Tricyclo[2.1.0.02.5]pentane,” *J. Am. Chem. Soc.*, vol. 99, no. 14, pp. 4851–4853, 1977, doi: 10.1021/ja00456a066.

[167] J. E. Baldwin and R. K. J. Pinschmidt, “Bicyclo[2.1.0]pent-2-ene. 6JHH spin-spin coupling in the cyclopentadiene Diels-Alder adduct,” *J. Am. Chem. Soc.*, vol. 92, no. 17, pp. 5247–5248, Aug. 1970, doi: 10.1021/ja00720a057.

[168] A. M. D. Lee *et al.*, “Substituent Effects on Dynamics at Conical Intersections: α,β-Enones,” *J. Phys. Chem. A*, vol. 111, no. 47, pp. 11948–11960, Nov. 2007, doi: 10.1021/jp074622j.

[169] T. J. A. Wolf *et al.*, “Hexamethylcyclopentadiene: Time-resolved photoelectron spectroscopy and ab initio multiple spawning simulations,” *Phys. Chem. Chem. Phys.*, vol. 16, no. 23, pp. 11770–11779, 2014, doi: 10.1039/c4cp00977k.

[170] S.-H. Lee *et al.*, “Substituent Effects in Molecular Electronic Relaxation Dynamics via Time-Resolved Photoelectron Spectroscopy: ππ* States in Benzenes,” *J. Phys. Chem. A*, vol. 106, no. 39, pp. 8979–8991, Oct. 2002, doi: 10.1021/jp021096h.

[171] F. Rudakov and P. M. Weber, “Ultrafast curve crossing dynamics through conical intersections in methylated cyclopentadienes,” *J. Phys. Chem. A*, vol. 114, no. 13, pp. 4501–4506, 2010, doi: 10.1021/jp910786s.

[172] F. Rudakov and P. M. Weber, “Ground state recovery and molecular structure upon ultrafast transition through conical intersections in cyclic dienes,” *Chem. Phys. Lett.*, vol. 470, no. 4–6, pp. 187–190, 2009, doi: 10.1016/j.cplett.2009.01.058.

[173] W. Fuß, W. E. Schmid, and S. A. Trushin, “Ultrafast photochemistry of cyclopentadiene: Competing hydrogen migration and electrocyclic ring closure,” *Chem. Phys.*, vol. 316, no. 1–3, pp. 225–234, 2005, doi: 10.1016/j.chemphys.2005.05.014.

[174] A. M. Michalik, E. Y. Sherman, and J. E. Sipe, “Theory of ultrafast electron diffraction: The role of the electron bunch properties,” *J. Appl. Phys.*, vol. 104, no. 5, p. 54905, Sep. 2008, doi: 10.1063/1.2973157.

Appendix

Diffraction simulation code

```
%This code was originally written by Dr. Kyle J. Wilkin. I modified this for using with our data. Using the code, the diffraction pattern can be simulated directly in one dimension. The input is just the structure of molecule.


load('Scattering 3.7MeV.mat','scat')        % This loads the form factor for a list of atoms for electron scattering with energy 3.7MeV

Path = 'E:\Research_backup_1122021\Stilbene Research\Stilbene_theory_geometris\cis_wigner_single.xyz';
% path where the structure of the molecule is saved in the computer.

fileID = fopen(Path);
C = textscan(fileID,'%s %s %s %s %*[^\n]');
fclose(fileID);

ds = 0.0250; % pixel to s calibration value
maxS = 10; % maximum s value set for s range

s = 0:ds:maxS;

NA = (str2double(C{1}{1})); % total number of atom in the molecule
N = round(length(C{1})/(NA + 2)); % total number of structure in the raw structure file
I_mol_cis_grnd = zeros(N,length(s)); % preallocating the array for molecular scattering intensity

Type = C{1}(2:27); % gets different type pf atoms
[UniqueAtoms,~,~] = unique(Type); % gets only the unique type of atoms
[s0,Scat,ScatIndex] = LoadScattering3p7MeV(Type,scat); % scat comes from the loaded file above.
```

```
NUA=length(UniqueAtoms); % Number of individual atoms
fmap = zeros(NUA,length(s));
for ii=1:NUA
   fmap(ii,:) = interp1(s0',Scat(ii,:),s,'spline');
end
for ii = 1:N
Start = (ii-1)*(NA+1)+2;
   Finish=ii*(NA+1)
   X = C{2}(Start:Finish);
   Y = C{3}(Start:Finish);
   Z = C{4}(Start:Finish);

   Coor={X Y Z Type};

   [I_mol_cis_grnd(ii,:)] = calcMolScat(Coor, fmap, s, ScatIndex, NA); % getting the molecular
scattering intensity
end
I_at=0;
for ii=1:NA
   I_at=I_at+abs(fmap(ScatIndex(ii),:)).^2; % getting the atomic scattering intensity

end

function [s0,Scat,ScatIndex] = LoadScattering3p7MeV(Atoms,scat);
%% Load scattering and phase information for atoms.
% INPUT:
%       Atoms: Nx1 cell array with each index corresponding to a character
%       with desired atoms, ex {'C'}
% OUTPUT:
%       s: Scattering vector associated with Scat and eta
%       Scat.X: Scattering amplitude for atom X.
%       ScatIndex: Index pointing Scat.X to the correct index from your
%       Atoms array.
%       Phase: Scattering phase for atom X.
```

```
[UniqueAtoms,~,ScatIndex] = unique(Atoms);

NUA=length(UniqueAtoms);
Scat = zeros(NUA,606);

% Phase = zeros(NUA,606);
for ii=1:NUA
   Scat(ii,:) =sqrt( scat.(UniqueAtoms{ii})); % added sqrt;

%     Phase(ii,:) = zeros(1,length(scat.(UniqueAtoms{ii}))); % I don't
%     think MeV needs phase.
end

U=3.7e6; %Acceleration field in V
E=U*1.6022*1e-19;m=9.1094e-31;h=6.6261e-34;c=299792458;%Physical constants
lambda=h/sqrt(2*m*E)/sqrt(1+E/(2*m*c^2));% Electron wavelength
k=2*pi/lambda;
s0=2*k*sind(scat.theta/2)/1e10;
 end

function [I_mol] = calcMolScat(Coor, fmap, s, ScatIndex, NA)

I_mol = zeros(1,size(fmap,2));

for z1=1:NA
   for z2=1:NA
      if z1~=z2
 coij = [str2double(Coor{1}{z1}) str2double(Coor{2}{z1}) str2double(Coor{3}{z1})] -
[str2double(Coor{1}{z2}) str2double(Coor{2}{z2}) str2double(Coor{3}{z2})];
         rij=sqrt(coij(1).^2+coij(2).^2+coij(3).^2);
         I_mol=I_mol+fmap(ScatIndex(z1),:).*fmap(ScatIndex(z2),:).*(sin(s*rij)./s./rij);
            end
   end
```

```
end
I_mol=real(I_mol);
 end
```

Gas phase diffraction analysis code

```
%% Getting Data Path
data_path = ('E:\Research_backup_1122021\Stilbene
Research\Data_Raw\20200314\Run\20200314_2115\scan001\images-ANDOR1\');
data_bank=data_generator_130(data_path); % This is a 4D array containing the raw data.

%% following function generates the 4D array based on the image stored in the local computer
function data_bank=data_generator_130(data_path)

%% get number of runs
data = dir(data_path); data = data(~strncmpi('.',{data.name},1));
no_runs_1 = size(data,1);

%% creating run path
run_path = cell(no_runs_1,1);
for i = 1:no_runs_1
        run_path{i,1} = strcat(data_path,'/',data(i).name);
        fprintf('run path found %d/%d \n',i,no_runs_1)
end

%% 2115 data bad frames; seeing the total count vs lab time, the following images are discarded
run_path(689)=[];run_path(686)=[];run_path(675)=[];run_path(660)=[];
run_path(549)=[];run_path(540)=[];run_path(532)=[];run_path(517)=[];
run_path(440)=[];run_path(373)=[];run_path(349)=[];run_path(342)=[];
run_path(332)=[];run_path(313)=[];run_path(245)=[];run_path(238)=[];
run_path(230)=[];run_path(220)=[];run_path(190)=[];run_path(161)=[];
run_path(158)=[];
run_path(118)=[];
```

```
%% splitting and extracting stage position
no_runs_1=size(run_path);
for i=1:no_runs_1
        split_1=split(run_path(i),'-');
        split_2=split(split_1(4),'_');
        stage_pos_1(i,1)=str2double(split_2(1));
        stgs(i,1)=stage_pos_1(i,1);
        fprintf('stages found %d/%d \n',i,no_runs_1)
end

stage_pos=unique(stage_pos_1);
no_delays=size(stage_pos,1);

%% Finding list of images corresponding to delay position
clear run_list

for i=1:no_delays

        stg_idx = stgs==stage_pos(i);
        stage_run=find(stg_idx(:,1)==1);
        run_size=size(stage_run,1);
        run_list(:,i)=run_path(stg_idx);
end

%% creating the databank
no_runs=size(run_list,1); delay_no=length(run_list);
stg_list_130=stage_pos(1:no_delays);

for j=1:no_delays
for i=1:no_runs
        data_bank(:,:,i,j)=double(imread(run_list{i,j}));

end
```

```
fprintf('Data_bank generated %d/%d \n',j,no_delays)
end

%% Background Image Processing

bkgpath1='E:\Research_backup_1122021\Stilbene Research\Data_Raw\20200314\Background\20200314_2003\scan001\images-ANDOR1\';

bkgpath2='E:\Research_backup_1122021\Stilbene Research\Data_Raw\20200314\Background\20200315_0713\scan001\images-ANDOR1\';
        bkg_data_1=BkgData(bkgpath1,bkgpath2);
%% The following function works to arrange the background image
function [bkg_data]=BkgData(bkgpath1,bkgpath2)
data_bkg1=dir(bkgpath1);
data_bkg1 = data_bkg1(~strncmpi('.',{data_bkg1.name},1));
data_bkg2=dir(bkgpath2);
data_bkg2 = data_bkg2(~strncmpi('.',{data_bkg2.name},1));

data_bkg=cat(1,data_bkg1,data_bkg2);

%% Cleaning the background image

for i=1:length(data_bkg)
            bkg_1(:,:,i)=double(imread(strcat(data_bkg(i).folder,'\',data_bkg(i).name)));
        bkg_2(:,:,i)=medfilt2(bkg_1(:,:,i),[5 5]);
end

for i=1:size(bkg_2,1)
  for j=1:size(bkg_2,2)
    A=squeeze(bkg_2(i,j,:));
    A_mean=nanmean(A);
    A_std=std(A);
    for k=1:length(A)
      if A(k)>A_mean+3*A_std || A(k)<A_mean-3*A_std
```

```
                A(k)=NaN;
            end
            bkg_3(i,j,k)=A(k);
        end

    end
end

bkg_mean=nanmean(bkg_3,3);
bkg_data=bkg_mean;


%% Applying the mask on the center hole


center_mask=[532  522]; %% this center is given based on the inspection of the artifact
    mask = createCirclesMask([1024,1024],center_mask,51);
    center_mask3=[463 503]; mask3 = createCirclesMask([1024,1024],center_mask3,17);


%% Data Clean Up: Step 1
center_trial=[531 490]; % This is a guess center found by a center finding algorithm

step=1;
tic;
             no_delays=size(data_bank,4); no_runs=size(data_bank,3);
             corrParr=[537.3678 529.8361 -0.0188 2.0599]; %elliptical correction parameters

for j=1:no_delays
       tic;
    ini_data=squeeze(data_bank(:,:,:,j));

%background subtraction
    data_BkgRmv=ini_data-repmat(bkg_data_1,1, 1, size(ini_data,3));

% elliptical correction
```

```
    for i=1:size(data_BkgRmv,3)

[imgCorner,basecount]=ring_correction(data_BkgRmv(:,:,i),center_trial); %% The ring
correction function is used to find the averag
 data_bCntRmv(:,:,i)=data_BkgRmv(:,:,i)-basecount;
 [img_EllipCorr,~]=ellipCorr(data_bCntRmv(:,:,i),corrParr);

% hot pixel removal
    Threshold = 1e4;img_EllipCorr(img_EllipCorr>Threshold)=nan;
     Img_HotRmv(:,:,i)=hotPxlRmv(img_EllipCorr,center_trial(1),center_trial(2),600, 180,400);

     %Img_Msk(:,:,i)=Img_HotRmv(:,:,i)+mask_calc_80uJ;
      a1=Img_HotRmv(:,:,i);
      a1=a1+imgCorner;
      a1(mask)=NaN;a1(531:580,520:575)=NaN;
a1(527:618,475:662)=NaN;a1(478:526,542:614)=NaN;a1(496:509,480:490)=NaN;
       a1(503:527,452:490)=NaN;
      Img_Msk(:,:,i)=a1;
       fprintf('delay position %f run number: %f \n',j,i);
    end

     img_clean(:,:,:,j)=vertical_correction(Img_Msk,4);% g is out elliptical correction.
     fprintf('Clean image found %d/%d \n',j,no_delays)
end
fprintf('Step done %d\n',step)
clear data_bank

function data_refine=vertical_correction(data_in,N);

for i=1:size(data_in,1)
    for j=1:size(data_in,2)

        XX=squeeze(data_in(i,j,:));
```

```
    XX_mean=nanmean(XX);
    XX_std=std(XX);
    for k=1:length(XX)
      if XX(k)>XX_mean+N*XX_std || XX(k)<XX_mean-N*XX_std
        XX(k)=NaN;
      end
      data_refine(i,j,k)=XX(k);
    end

  end
end
%data_refine=nanmean(YY,3);

%% Data Clean Up: Step 2: this step is required to get a refined center
tic; step=2; center_trial=[529.7699 491.0260 ];  pixel=1:550;

   for j=1:no_delays
    img=squeeze(img_clean(:,:,:,j));

   for i=1:size(img,3)



  fprintf('delay position %f run number: %f \n',j,i);
  % radial outlier removal

[~,~,~,~,img_RadRmv,stand_dev]=SubtractRadialMean(img(:,:,i),center_trial(1),center_trial(2),-
1, 3);

  %filling the nan
  Img_nanFill=diffNanFill(img_RadRmv,center_trial,0);

 % Applying MedFilt

  Img_medFilt=medfilt2(Img_nanFill,[5 5]);
```

```
    %Restoring the Nan
    x2=Img_medFilt;
   x2(isnan(img_RadRmv))=NaN;

    Img_fresh(:,:,i)=x2;
    end

     Img_avg(:,:,j)=nanmean(Img_fresh,3);
      rGuess=150:50:250;
    [ cGuess,~] = findCenter_2(Img_avg(:,:,j),rGuess,0.05,0);
      [cRansac(:,j),~] = findCenterRansac(Img_avg(:,:,j),cGuess,rGuess,2,0);
            fprintf('center found for %d/%d \n',j,no_delays)
end
 center_130uJ=mean(cRansac,2);
  clear Img_avg
  fprintf('Step Finsihed %d \n',step)


%% Data Clean Up: Step 3: this step is required to get azimuthal avg by refined center
 step=3;
 for j=1%:no_delays
       img=squeeze(img_clean(:,:,:,j));

     for i=1:size(img,3)

    fprintf('delay position %f run number: %f \n',j,i);
   % radial outlier removal

[~,~,~,~,img_RadRmv,stand_dev]=SubtractRadialMean(img(:,:,i),center_130uJ(1),center_130uJ(
2),-1, 3);
  azi_RadRmv(:,i,j)=azi(img_RadRmv,center_130uJ,pixel);
   %filling the nan
   Img_nanFill=diffNanFill(img_RadRmv,center_130uJ,0);
```

```
  % Applying MedFilt

    Img_medFilt=medfilt2(Img_nanFill,[5 5]);

    %Restoring the Nan
    x2=Img_medFilt;
   x2(isnan(img_RadRmv))=NaN;

    Img_fresh(:,:,i)=x2;

    azi_fresh(:,i,j)=azi(Img_fresh(:,:,i),center_130uJ,pixel);

    end
    fprintf('azimuthal Avg found for %d/%d \n',j,no_delays)
        Img_avg(:,:,j)=nanmean(Img_fresh,3);
end
 fprintf('Step Finsihed %d \n',step)

%% Baseline Removal
 Azi_BaseRmv=squeeze(nanmean(azi_fresh,2));
for j=1:no_delays
    baseline(:,j)=mean(Azi_BaseRmv(500:550,j));
end
baseline_mean=baseline-min(baseline);
for j=1:no_delays
    for i=1:size(azi_fresh,2)
        azi_130_corr(:,i,j)=azi_fresh(:,i,j)-baseline_mean(j);

    end

     fprintf('Baseline Correction finsihed  %d/%d \n',j,no_delays)
end

%% Normalization
```

```
ds=0.0250;
s_130=(0:549)*ds;
%   Azi_com=azi_130_corr;

   for j=1:no_delays
      for i=1:size(Azi_com,2)
         sum_h_com=nansum(Azi_com(100:300,i,j));
         arc_norm_com_130(:,i,j)=Azi_com(:,i,j)./sum_h_com;
      end
       fprintf('Normalization done  %d/%d \n',j,no_delays)
   end




s_expt=single((0:549)*ds);
clear dI_step_1 dI_step_2 dsM_80uJ  dI_I_80uJ
arc_norm_com_80=single(arc_norm_com_80);
 s_130=s_expt;
for j=1:size(arc_norm_com_130,3)
     % erasing problematic frames
   Arc=squeeze(arc_norm_com_80(1:550,:,j));
    Range=round(10/ds);
   if j==12
          Arc(:,[2 3 7 10 19 20])=[];
   end

         if j==15
          Arc(:,30:32)=[];
         end
         if j==16
         Arc(:,31:32)=[];
         end
         if j==19
```

```
        Arc(:,31:32)=[];
        end
        fprintf('Bad Frames removed. \n')
%   bootstraping
    nBoot=100;
    kk=1;
        for ii=1:nBoot
                                      idx=single(randsample(1:size(Arc,2),size(Arc,2),'true'));
        I_end(ii,:,j)=nanmean(Arc(:,idx),2);
        end
end
%%
for j=1:no_delays
    for ii=1:nBoot
      I_ref=nanmean(I_end(ii,:,25:28),3);
        dI_step_1(ii,:,j)=(I_end(ii,:,j)-I_ref);
        dI_step1_mean=mean( dI_step_1(ii,250:end,j));
        dI_step_2=dI_step_1(ii,:,j)-dI_step1_mean;


%           % calculation of dI/I
        dI_I_130uJ=dI_step_2./I_ref;

dI_I_130uJ_cut1=(dI_I_130uJ(:,1:Range,:));
dI_I_plot1=dI_I_130uJ_cut1;

        n0=findzeros(dI_I_plot1);

      if numel(n0)<1
        dI_I_plot1=nan;
        continue
      end

      s1=s_expt(n0(1):Range);
```

```
     test_2= dI_I_plot1(n0(1):Range);
    ft2 = fittype( 'a*x^b+c');
        opts = fitoptions( 'Method', 'NonlinearLeastSquares' );
        opts.Display = 'Off'; opts.Robust = 'LAR';
        opts.Lower=[-inf 0 -inf];%opts.Upper=[4.502E-6 5.528];
        [f2,gof]=fit(s1',test_2',ft2,opts);
%

      line2=f2.a.*s_expt.^f2.b+f2.c;
     dI_I_130uJ_corr(ii,:,j)=  dI_I_plot1-line2(1:Range);

     if  nanmean( dI_I_80uJ_corr(ii,20:50,j),2)>0.3 || nanmean( dI_I_130uJ_corr(ii,20:50,j),2)<-
0.3
        dI_I_130uJ_corr(ii,:,j)=nan;
     end
fprintf('dI_I calculated for bootstrap %d and delay %d \n',ii,j)
```

Application of Gaussian convolution

```
function [dsM_G,GaussFact] = GaussFit_4Sajib(dsM,t,FWHM)
%% dsM should be a matrix with time along the second dimension.
% t is the corresponding time steps.
% FWHM (Optional) is the FWHM of the Gaussian you want to convolve.
% dsM=dI_mean_smooth;
% t=time_delay_80;
% FWHM=100;
if nargin < 3 || isempty(FWHM)
  FWHM=100;
end


%FWHM=FWHM*1e-15;
```

```
sig=FWHM/(2*sqrt(2*log(2)));    % Turn FWHM to Sigma



GaussFact=zeros(size(dsM,2));
for i=1:size(dsM,2)
   GaussFact(i,:)=exp(-(t(i)-t).^2/2/sig^2);    % Set a Gaussian weighting function for each time step
end
for i=1:size(dsM,2)
   GaussFact(i,:)=GaussFact(i,:)/sum(GaussFact(i,:));    % Normalize the weights
end

dsM_G=zeros(size(dsM));

for i=1:length(t)
   dsM_G(:,i)=dsM*GaussFact(i,:)';    % Convolve the each time step with its corresponding weight vector. Notice this is not .* so there is a sum involved
end
```

Three Parameter fitting algorithm using Particle Swarm

```
function [coeffs,perc1,perc2,dI_I_end,chi]=min_ration_3_param(data,err,dI_I_end1,dI_I_end2,nSwarm,s_start,s_end)

rng('shuffle')

lb=[ 0.00001  0  -200 ];
ub=[ 100   100  200 ];




s=(1:length(data))*0.0250;
opts=optimoptions('particleswarm','Swarmsize',nSwarm,...
```

```
    'FunctionTolerance',1E-4,'MaxIterations',nSwarm*2,'MaxStallIterations',round(nSwarm/5),...
    'Useparallel',true,'Display','iter');



[coeffs]=particleswarm(@findCorrPar,numel(lb),lb,ub,opts);
    function obj=findCorrPar(c)




S=c(1)+c(2);
dI_I_end=1/S*(c(1)*dI_I_end1+c(2)*dI_I_end2);


 obj=1/(numel(s_start:s_end)-numel(lb))*nansum(((data(s_start:s_end)-
1/c(3)*dI_I_end(s_start:s_end))./err(s_start:s_end)).^2);

    end
c=coeffs;

S=c(1)+c(2);
dI_I_end=1/S*(c(1)*dI_I_end1+c(2)*dI_I_end2);
     perc1=c(1)/S;
     perc2=c(2)/S;


 chi=1/(numel(s_start:s_end)-numel(lb))*nansum(((data(s_start:s_end)-
1/c(3)*dI_I_end(s_start:s_end))./err(s_start:s_end)).^2);




 end
```

Error-function Fitting

```matlab
hold on;
ft = fittype( 'a*erf(-(x-b)/(c/ (2*sqrt(2*log(2))) *sqrt(2)))+d');
opts = fitoptions( 'Method', 'NonlinearLeastSquares' );
opts.Display = 'Off'; opts.Robust = 'LAR';
opts.StartPoint = [0 0.1 0.1 0.01]; % you have to find this point after fitting this function at cftool.


dI_I_mean=nanmean(dI_I_combined_Gaussfit(55:87,26:57)); % This is the vector which we want to fit
pos=time_delay_organized_2(26:57); % This is the independent variable in the fit
dsM= dI_I_mean;

figure;

[f1,gof]=fit(pos',dsM',ft,opts);
 plot(f1,pos,dsM,'-o');
 gof
f1.c
set(gca,'fontsize',20)
```